Sediment dynamics in tidal environments spanning a range of fluvial influence

Daniel J. Nowacki

A dissertation
submitted in partial fulfillment of the
requirements for the degree of

Doctor of Philosophy

University of Washington

2014

Reading Committee:

Andrea S. Ogston, Chair

Alexander Horner-Devine

Charles Nittrouer

Program Authorized to Offer Degree:
Oceanography

University of Washington

Abstract

Sediment dynamics in tidal environments
spanning a range of fluvial influence

Daniel J. Nowacki

Chair of the Supervisory Committee:
Professor Andrea S. Ogston
Oceanography

A full understanding of the transport of sediment from terrestrial source to marine sink requires knowledge of dynamics in a multitude of intermediate environments with both fluvial and marine influences. Two of these environments, tidal flats and tidal rivers, are dramatically different in scale and setting but are unified by common sedimentary processes. This dissertation presents observations of flow and sediment transport on the tidal flats of Willapa Bay, Washington, USA; tidal channels along the tidal floodplain of the Amazon River, Brazil; and the mainstem of the tidal Mekong River, Vietnam. These three study sites are ideal locations to improve understanding of where, when, and how the annual worldwide total of 13 billion metric tons of sediment is delivered from land to ocean.

The muddy tidal flats of southern Willapa Bay, Washington are tidally dominated and receive little direct freshwater input. Observations in channels of different size and their adjacent flats illustrate the hydrodynamics and sediment dynamics of each morphological setting under a range of seasonal and meteorological conditions, including rain and wind events. Interaction between the morphology of the channel/flat complex and tidal water-level variations produces well-defined velocity pulses during both flooding and ebbing tides. These pulses represent about 27% of the total along-channel water transport and 35% of the suspended-sediment transport of the system. Wind alters the typical flow regime in channels and on the flat, increasing the over-flat ebb flow in this study location while decreasing the

ebb-pulse intensity. Wind speed was positively correlated with background suspended-sediment concentration (SSC). Residual along-channel water transport in channels and on nearby flats was flood dominant under all seasonal conditions sampled. Sediment flux was flood dominant during winter and spring deployments.

In contrast to channels incising the Willapa flats, the channels connecting the mainstem Amazon River to its tidal floodplain have considerably more fluvial influence. Water level, flow velocity, temperature, and SSC were measured in floodplain channels along the tidal Amazon River, Brazil. Eleven deployments were made at four locations during low, rising, high, and falling seasonal river level. These observations are the first of their kind on the Amazon. In nearly all cases, tidal channels import water with high SSC from the mainstem to the tidal floodplain on flood tides and export water with low SSC back to the mainstem on ebb tides. The importance of sediment resuspension in transferring sediment to the tidal floodplain decreases with distance from the mainstem river mouth. Overbank flow in strongly tidal regions is an important characteristic of the flow regime and is controlled both by the seasonal water level and tidal conditions. A synthesis of the observations indicates that tidal-floodplain channels are important conduits of water and sediment along the tidal river, and a measurable but small percentage of the total mainstem water and sediment discharge is exchanged with the tidal floodplain.

Export of sediment from intertidal environments, such as tidal-floodplain channels, to the coastal ocean is strongly influenced by mainstem tidal-river dynamics. Flow velocity, salinity, and SSC were measured for 25 hours at three cross-sections in the tidal Song Hau distributary of the Mekong River, Vietnam. Estuarine conditions varied dramatically between high and low seasonal discharge periods. The system transitioned from a tidal river with an ephemerally present salt wedge during high flow to a partially mixed estuary during low flow. The changing freshwater input, sediment sources, and estuarine conditions resulted in sediment export during high flow and import during low flow. The Dinh An channel of the Song Hau distributary exported sediment to the coast at a rate of about 1 $\mathrm{t\,s^{-1}}$ during high flow and imported sediment in a spatially varying manner at approximately

0.3 t s^{-1} during low flow. These values scale to a yearly sediment discharge of 40×10^6 t y^{-1} for the entire Mekong River, about 65% less than a generally accepted estimate of 110×10^6 t y^{-1}. Fluvial advection of sediment was primarily responsible for the high-flow sediment export, while exchange-flow and tidal processes, including local resuspension, were principally responsible for the low-flow import. The resulting bed-sediment grain size was coarser and more variable during high flow and finer during low flow. The residual flow patterns supported the maintenance of mid-channel islands.

TABLE OF CONTENTS

LIST OF FIGURES

LIST OF TABLES

ACKNOWLEDGMENTS

I am indebted to many individuals and organizations for their support over the past six years. Firstly, I thank my adviser, Andrea Ogston, for her guidance and friendship. I am also truly thankful to my master's adviser and reading committee member Alex Horner-Devine, who, along with Andrea, helped me navigate the sometimes turbulent waters of graduate school. My deep thanks also to the rest of my committee: Chuck Nittrouer, Neil Banas, and Darrel Cowan.

I am thankful to the graduate students, past and present, of the Sediment Dynamics Group and UW-EFM. In particular, my office mate, Aaron Fricke, has been a continual source of inspiration and, at times, distraction.

I have the distinct pleasure of having been part of several large research initiatives in several locations around the globe, and I am appreciative of all the members of those projects. In Willapa Bay, I enjoyed collaboration with many local and international colleagues on the Tidal Flats DRI. In Brazil, I deeply appreciate the friendship, camaraderie, and collaboration of the faculty, staff, and students of Universidade Federal do Pará, especially Odete Silveira, whose memory will live on in future Amazon research. For the Mekong work, I am deeply grateful for the guidance, assistance, and friendship of Rich Nguyen. I'm also thankful to the students, staff, and faculty of Can Tho University, along with the boat operators and local populace of Cu Lao Dung district, Soc Trang Province, Vietnam.

I am grateful to the staff par excellence of the School of Oceanography administration office. Thanks also to the UW Ocean Engineering Services, especially Randy Fabro, Tor Bjorklund, and Dave Thoreson.

I was supported financially by a National Defense Science and Engineering Graduate Fellowship from 2010–2013. The tidal-flats work was funded by the Office of Naval Research, award numbers N00014-08-1-0759, N00014-08-1-0789, and N00014-10-1-0213. The Amazon

research was supported by the National Science Foundation and the Office of Naval Research. Work on the Mekong was funded by the Office of Naval Research, award numbers N00014-12-1-0181, N00014-13-1-0127, and N00014-13-1-0781.

Finally, and most gratefully, I give thanks and love to my family and ABB.

DEDICATION

In memory of Dianne Croft Nowacki

Chapter 1

INTRODUCTION

Understanding the transfer of sediment from terrestrial source to marine sink is essential for knowledge of global carbon budgets, prediction of landform evolution, and interpretation of the stratigraphic record. Sediment is eroded, transported, and trapped via a myriad of processes along the continuum from riverine to oceanic environments. The varying degrees of fluvial, tidal, and wave influence in each environment drive these processes. This dissertation focuses on sedimentary dynamics in two critical gateways within the source-to-sink continuum: tidal flats and tidal rivers.

Tides are one of the most recognizable properties of the oceans. They mix water masses, resuspend and transport sediment, and disperse pollutants. Produced by astronomical forces, they are influenced by the geometry of the ocean, coastline, and coastal intrusions like lagoons, estuaries, and rivers. As a result, the largest tides occur in shallow coastal environments where morphology amplifies the tidal wave (Fig. 1.1). Deformation from frictional damping, channel convergence, and tidal-wave reflection affects the characteristics of the tide and tidal currents. Flood velocity dominance is a common result of tidal deformation in shallow water, wherein flood-tide currents are faster than ebbs (Dyer, 1986). The interaction between tidal asymmetry and sedimentary processes such as settling and resuspension leads to settling and scour lag effects (e.g., van Straaten and Kuenen, 1958; Postma, 1961), which result in landward residual transport of sediment. This flood-tide-oriented pumping of sediment is an essential sedimentary process in tidal flats, estuaries, and other shallow environments, and may be ephemerally active even in river-dominated systems.

Although tides are one of the strongest sedimentary forcing mechanisms in coastal settings, other factors, including river discharge, storms and waves, and geomorphic complexity, can also be important. Rivers link the land to the sea and have a dramatic influence on

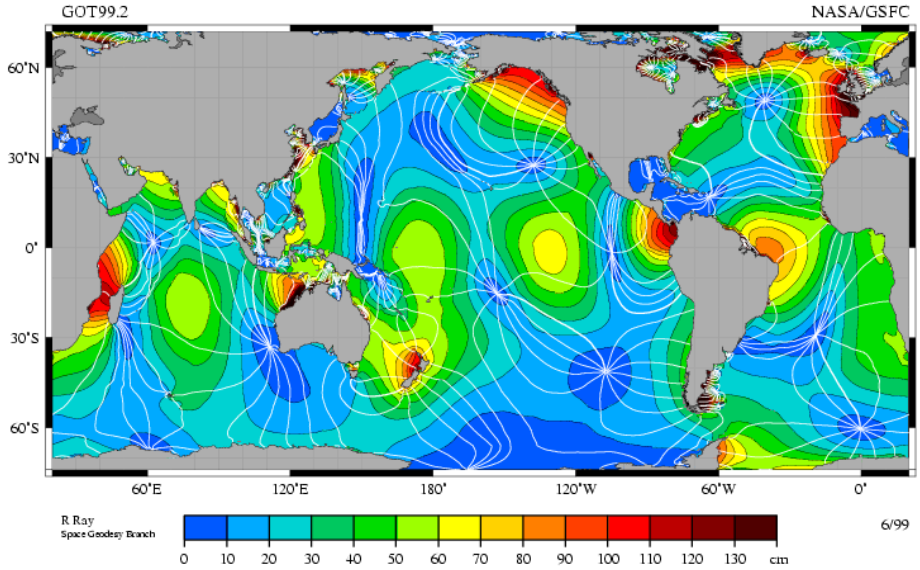

Figure 1.1: Map of worldwide distribution of the M2 tidal component. Courtesy NASA GSFC/JPL Scientific Visualization Studio.

coastal environments. They discharge about 3.6×10^4 km^3 of freshwater each year (Milliman and Farnsworth, 2011) and are the the largest suppliers of sediment to the world ocean, delivering about 13 Gt y^{-1} today (Syvitski and Kettner, 2011). Large rivers are particularly important. The ten largest rivers transport about 40% of the water and particulate matter entering the ocean (Dagg et al., 2004). The Amazon alone supplies about 20% of the total freshwater delivered to the ocean. Further, large rivers are primarily responsible for 80+% of the sedimenting organic carbon that accumulates on continental shelves (Berner and Raiswell, 1983) and 40% of the global marine carbon burial that takes place in deltaic environments (Hedges and Keil, 1995).

In all coastal regions, interaction among rivers, tides, and waves strongly influences sediment dynamics. In the two environments at the center of this dissertation, tidal flats and tidal rivers, riverine and tidal influences dominate the sediment dynamics, with limited wave influence. A brief overview of the tidal-flat and tidal-river environments is given below, followed by a more thorough description of the study sites, an enumeration of this dissertation's research goals, and a presentation of the document's organization.

1.1 Tidal flats

Tidal flats develop in areas with large tidal range, a sizable sediment source, and limited waves. Flats at or near mean high-water level often are heavily vegetated and, in temperate regions, form salt marshes. *Intertidal flats* are lower elevation and are smoother, with less vegetation; they are generally what is meant by the general term "tidal flats." Because tidal flats lie between low and high water and typically have an extremely shallow bed slope, vast swaths of tidal-flat area may be exposed and submerged over the course of a tidal cycle. The sediment grain size of tidal flats generally is coarser and often sandy in deep regions, and finer, usually muddy, at mid-to-upper elevations. One key geomorphic feature of tidal flats is the innumerable tidal channels that dissect them, but many studies overlook dynamics in the channels and instead focus on processes taking place over the flats proper (see Amos, 1995; Friedrichs, 2011, for reviews).

Complex forcing mechanisms and geomorphic settings are present in tidal flats, both of which modify transport of sediment. In addition to the daily tidal forcing, seasonal variability is also important. For example, changes in river discharge can modify dynamics in tidal-flat settings close to a riverine source (e.g., Yang et al., 2001; Webster et al., 2013). Energetic storm events increase suspended-sediment concentration (SSC) in the water column and may erode sediment through wave action (e.g., Anderson et al., 1981; Yang et al., 2003). Storms are countered during calmer periods by biological production which stabilizes the seabed, potentially leading to sediment accumulation (e.g., Anderson et al., 1981; Christie et al., 1999). The variable bathymetry of channels incising tidal flats, which can vary by several meters in depth over short distances, suggests a heterogeneity in the hydrodynamics and sediment-transport processes occurring there. Despite complex sedimentary forcings, sediment accumulation on tidal flats can keep pace with local sea-level rise (Boldt et al., 2012), even without a significant local sediment source.

1.2 Tidal rivers

Tidal rivers are those river reaches that are tidally influenced but without salinity. They lie downstream of the purely fluvial river region but upstream of the estuary, where brackish or

saltwater is present. Today, the tidal river remains a significant missing link in understanding material transfer from the land to the ocean. This situation exists largely because of historical scientific boundaries: the tidal river occupies a no-man's land between the realm of hydrologists and fluvial geomorphologists in the non-tidal river and estuarine physicists and marine sedimentologists in the estuarine, coastal, and shelf regions. This missing link is potentially the site of many important hydrodynamic, sedimentary, and geochemical transformations taking place between land and ocean.

The extent and character of the tidal river changes over a spectrum of temporal and spatial scales. Tides, varying on the order of minutes to fortnights, seasonal river discharge, and longer-term climatic change all impact processes in the tidal river. The spatial extent of the tidal river can approach 1000 km in length for the largest tidal rivers (e.g., Amazon: 800 km; Mekong: 300 km; Columbia: 200 km) and can contract or expand daily, monthly, or seasonally. The tidal river is also morphologically complex, with abrupt bathymetric changes between mainstem river channel, river banks, and floodplains.

Interaction between the river and its floodplain drives transformations as water and sediment travel downstream. In fluvial settings, the river and floodplain are generally separated by a natural levee, and communication of water and sediment between the mainstem and floodplain is restricted to times when the levees are overtopped. In contrast, the tidal river is often in contact with its floodplain twice per day, as tidal water-level variations inundate and expose the floodplain. This increased connectivity potentially enables significant sequestration of sediment on the floodplain that otherwise would have been delivered to the coastal ocean. Furthermore, floodplain-incising tidal channels form in many tidal-river environments, and they are additional conduits of sediment exchange between the mainstem and floodplain. The tidal-floodplain channels may also facilitate temporary or long-term storage of sediment on the tidal floodplain.

In addition to processes in the tidal-floodplain channels, dynamics in the mainstem tidal river may export or import sediment over a variety of timescales. Sediment may be discharged to the coastal ocean during high river-flow conditions and temporarily deposited on the continental shelf before being resuspended and imported back into the channels during low river flow. Seasonality in the form of waves and currents on the shelf interacts

with tidal-river processes to further alter the sediment dispersal system. In summary, the processes of export and import in the tidal river modulate the non-tidal sediment-transport characteristics, altering sediment delivery to the coastal ocean.

1.3 Study sites

In recognition of the importance of tidal flats and tidal rivers in the source-to-sink continuum, this dissertation investigates sedimentary mechanisms in three distinct locations: Willapa Bay, Washington, USA, the Amazon River, Brazil, and the Mekong River, Vietnam (Fig. 1.2). The Willapa Bay study area is home to extensive tidal flats and experiences little direct fluvial influence, while the Amazon and Mekong are among the top ten rivers worldwide in terms of freshwater discharge. Vegetation along the Amazon and Mekong intertidal areas provides contrast to the denuded Willapa flats. The Amazon is purely freshwater, macrotidal, and pristine, while the Mekong is ephemerally brackish, mesotidal, and heavily impacted by humans. While the environments are varied, they share fundamental similarities. For example, the flat-incising channels of Willapa Bay bear strong resemblance to the tidal-floodplain channels along the Amazon River. In addition, the complex morphology of the Mekong distributary channels is shared by the mainstem of the Amazon. This dissertation not only investigates these environments as self-contained research topics, but also seeks to compare and contrast them and find linkages among the processes that pervade each.

Over the past few decades, dozens of studies have investigated the sedimentary and hydrodynamic processes of muddy tidal-flat environments across the globe (e.g., China: Shi and Chen, 1996; Brazil: Allison et al., 1995; Korea: Wells et al., 1990; Alexander et al., 1991; northwest Europe: Dyer et al., 2000a). In addition, significant work has been undertaken in small channels of higher-elevation salt marshes (see Friedrichs and Perry, 2001 for a review) and in larger or river-influenced channels in tidal flats (e.g., Ralston and Stacey, 2007; Webster et al., 2013). To date, comparatively little work has been carried out in the innumerable small channels that incise tidal flats, and Willapa Bay provides an ideal setting for studies of this kind.

On the Amazon, large sediment-related research projects have been carried out upstream

of tides (CAMREX; e.g., Dunne et al., 1998) and seaward of the mouth (AmasSeds; Nittrouer et al., 1995) but little study has been undertaken along the 800-km length of the tidal river, with few exceptions (e.g., Vital et al., 1998; Vital and Stattegger, 2000b). On the Mekong, the situation is similar, and the only significant prior work on the sediment dynamics of the tidal river was reported in Wolanski et al. (1996, 1998). The paucity of information about processes in these two globally important systems motivates their further study.

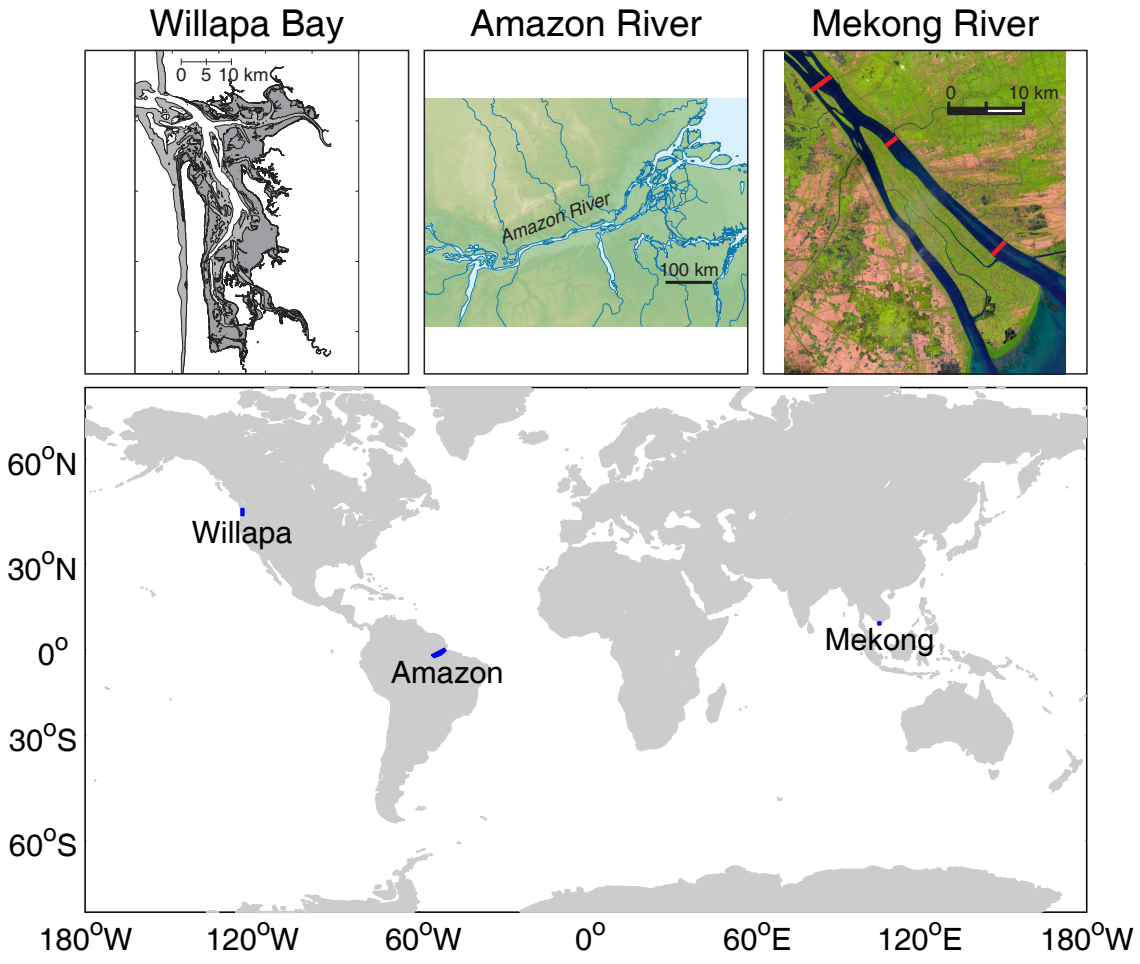

Figure 1.2: Field locations in this dissertation.

1.4 Research goals and document organization

The objective of this dissertation is to increase knowledge of sediment transport dynamics in tidal systems spanning a range of fluvial influence. This research is aimed at understanding the tidal- and seasonal-scale hydrodynamics and sediment dynamics of tidal-flat and tidal-river systems through instrumented observations.

The research goals for each environment, as expanded upon below, are (1) to describe the characteristics of sediment transport in a flat-incising channel of a tidal-flat system; (2) to identify the major processes by which small channels import or export sediment to or from the floodplain of a tidal river; and (3) to describe the sediment dynamics of the mainstem of a large tropical river.

The data and analyses in Chapters 2, 3, and 4 are the result of field campaigns carried out in three distinct environments (Fig. 1.2). Data were collected between 2008 and 2010 in the tidal flats of Willapa Bay, Washington, USA and form the basis of Chapter 2. Four cruises on the tidal Amazon River, Brazil from 2010–2014 provide the data in Chapter 3. Two field campaigns were carried out in 2012 and 2013 on the tidal Mekong River, Vietnam, and are presented in Chapter 4. These chapters were written for standalone publication in peer-reviewed journals: Chapter 2 was published in *Continental Shelf Research* as Nowacki and Ogston (2013); Chapters 3 and 4 are in preparation for publication.

Chapter 2 discusses tidal-flat sediment-transport in southern Willapa Bay. The Chapter presents water-column data collected over a period of ten months, examines processes that transfer fine-grained sediment within and between the flats and the channels that incise them, calculates the water and sediment fluxes of the system, and examines the dynamics of short-lived velocity pulses that contribute significantly to the sediment budget.

Chapter 3 presents a spatially and temporally extensive data set collected in tidal channels that incise the floodplain of the tidal Amazon River. The data, which are the first published measurements of their kind on the Amazon, include water level, flow velocity, water temperature, and SSC during a range of seasonal discharge levels. The Chapter describes the sediment dynamics of these channels through space and time, investigates the thermal dynamics of the channels and their relation to sediment transport, explores the

feedbacks among seasonal water level, tides, and geomorphology, and develops an initial estimate of sediment exchange with the Amazonian tidal floodplain.

Chapter 4 describes observations made on a distributary of the lower Mekong River during high- and low-discharge periods to characterize its hydrodynamics and sediment dynamics. The Chapter quantifies the changes in the hydrodynamics and sediment transport on multiple temporal and spatial scales, decomposes the residual sediment flux to determine the contributions of different sediment-transport processes and their variability with discharge, and discusses the geomorphic implications of the observations.

Chapter 2

TIDAL-FLAT WATER AND SEDIMENT TRANSPORT[1]

2.1 Introduction and Background

Intertidal flats are an important gateway for particles transported from terrestrial source to marine sink and are characterized by a network of channels that incise them. Tidal forcing is one of the strongest drivers of variability in tidal-flat systems. It modulates residual flows and circulation (e.g., Kjerfve, 1986), can control the relative magnitudes of peak velocity on flood and ebb (Fortunato and Oliveira, 2005), and modifies net sediment accumulation (Allen et al., 1980) in tidal flats and estuaries. Velocity in tidal channels often is flood dominated (i.e., greater peak flood velocity than ebb velocity; Postma, 1967) but the observed balance varies widely among study locations. For example, in the macrotidal Namyang Bay flats of western South Korea, which lack major river input, ebb speeds are 5–10% faster than flood speeds (Wells et al., 1990). Analytical modeling suggests that tidal flats generally enhance ebb velocity dominance when the flats are at mean sea level or above, whereas flood dominance is promoted by large tidal amplitudes and increased friction (Fortunato and Oliveira, 2005). Velocity dominance has also been related to the ratios of channel depths and widths at high and low tide (Friedrichs et al., 1992).

Landward, or upstream, transport of sediment is often observed in tidal environments (Postma, 1967; Pejrup, 1988; Christie et al., 1999; Le Hir et al., 2000) and is attributed variously to asymmetric tidal currents, settling lag, scour lag, and flocculation effects. Yet channels may also be net exporters of sediment. Studies in macrotidal flats (Wells et al., 1990) have observed channels to be conduits for offshore sediment dispersal during ebb tides. Events, including storms and increased riverine water and sediment input, are also recognized as important to the sedimentological and morphological dynamics of these sys-

[1]This chapter published as: Nowacki, D.J., & Ogston, A.S. (2012). Water and sediment transport of channel-flat systems in a mesotidal mudflat: Willapa Bay, Washington. *Continental Shelf Research*, 114. doi:10.1016/j.csr.2012.07.019.

tems (e.g., Anderson et al., 1981; O'Brien et al., 2000; Yang et al., 2005). Wind-generated waves associated with storms are effective in resuspending sediment in tidal-flat environments (Anderson et al., 1981; Sanford, 1994; Brand et al., 2010), and storms have been shown to be important remobilizers of tidal-flat sediments into channels (Wells et al., 1990; Yang et al., 2003). Waves also have been observed to temporarily change the sediment flux balance on tidal flats from flood dominance to ebb dominance (Christie et al., 1999; Dyer et al., 2000b; Lee et al., 2004). Relevant event time scales range from days to seasons, and the onset of event influence can be rapid or gradual and have short- or long-term effects. For example, sediment resuspended by waves and precipitation may be stored within channels immediately but subsequently eroded over days to months after the event has passed (Yang et al., 2003).

Short-lived occurrences of elevated velocity, which we term pulses, have been observed in tidal creeks for decades (e.g., Pestrong, 1965), and a specific study of the pulse as a phenomenon dates to as early as 1979 (Bayliss-Smith et al., 1979). The pulse is often framed using continuity arguments as water level crosses a marsh platform or tidal flat (Boon, 1975; French and Stoddart, 1992; Allen, 1994). Most published observations of the pulse have been made in salt marshes where it occurs at higher relative water depths than in lower-elevation tidal flats. Although the pulse may only occur in salt marshes on the greatest spring tides or during storm surges, it occurs with regularity in lower-elevation intertidal flats and is a more consistent feature in the flow regime.

Rain events in shallow-water environments have been shown to reduce the critical sediment erosion threshold (Green and Houk, 1980) and increase erosion rates, particularly in muddy sediments (Mwamba and Torres, 2002; Tolhurst et al., 2006; Pilditch et al., 2008). Bed shear stresses induced by direct (exposed surface) rainfall generally exceed the critical stress values for intertidal sediments and can be much larger than stress associated with waves and tidal forcing (Mwamba and Torres, 2002). Rainfall on exposed cohesive sediment has resulted in suspended-sediment concentration (SSC) values 2–100 times those observed without raindrop-induced sediment erosion (Mwamba and Torres, 2002).

In this paper we present water-column data collected over a period of ten months on the tidal flats of southern Willapa Bay, Washington. We examine processes that transfer

fine-grained sediment within and between the flats and the channels that incise them. We calculate the water and sediment fluxes of the system and examine the dynamics of short-lived velocity pulses that contribute significantly to the budget.

2.2 Study area

Willapa Bay is a bar-built estuary located in southwest Washington (Fig. 2.1), and is the first embayment north of the Columbia River mouth, covering an area of approximately 350 km^2. Extensive tidal flats are found in Willapa Bay, and 50% of the bay's surface area and volume are in the intertidal zone (Andrews, 1965). Willapa Bay has a mixed semidiurnal tidal regime with a mean daily tidal range of 2.7 m (Banas et al., 2004).

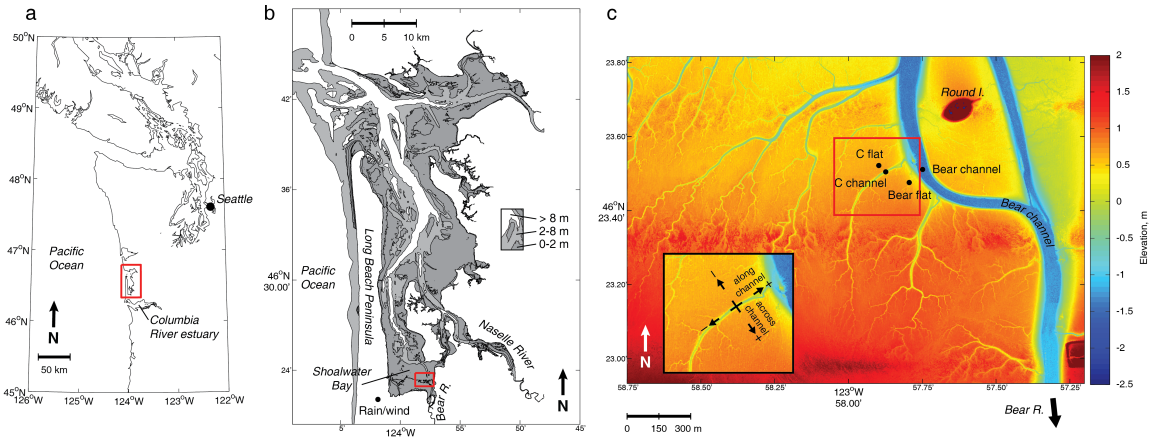

Figure 2.1: (a) Map of the Pacific Northwest coastal region, with Willapa Bay indicated by red box. (b) Willapa Bay bathymetry relative to mean sea level, with study area indicated by red box. The black circle southeast of Shoalwater Bay marks the location of the WSU AgWeatherNet station. (c) Study area map showing bathymetry relative to NAVD 88 (Buijsman et al., 2002) and instrument locations indicated by black circles. The inset, denoted by the red box, shows the rotated channel-wise coordinate system. The on-site weather station was located near the Bear flat location.

This study was undertaken on the muddy tidal flats of southern Willapa Bay, in an area known as Shoalwater Bay, which is approximately 4 km by 2.5 km in size. Most observations were made in the thalweg of a secondary—alternately inundated and exposed—channel known as "C channel" and on the adjacent flat to the north (Fig. 2.1). At the measurement

location, C channel was approximately 15 m wide at bankfull and had a maximum depth of 1 m below the flat elevation. Maximum water depth above the channel bottom was more than 4 m during spring tides. Observations were also made in the larger, primary (always inundated) Bear channel. Near the study site, median sediment grain size corresponds to fine-to-medium silt, with representative distributions of 10–20% sand, 50–60% silt, and 30–40% clay (Boldt et al., 2012). Shoalwater Bay receives little direct riverine input. The Naselle River is the primary freshwater source for the southern portion of Willapa Bay, and it drains a portion of the coastal mountain range that forms the bay's eastern border. The Naselle represents 20% of the bay's total freshwater input (Banas et al., 2004), with an 80-year mean discharge of 12 m^3 s^{-1}, and its mouth is approximately 6 km northeast of the study site. The North and Willapa Rivers contribute most of the rest of the freshwater input and enter the bay near its northern end. The small Bear River is the closest freshwater source and seaward of its mouth forms Bear channel (Fig. 2.1). While presently unmonitored, the Bear River was gauged from 1963 to 1975, and regression of concurrent Bear River and Naselle River (which is currently monitored) discharge data indicates a linear relationship ($r^2 = 0.86$), with Bear River discharge about 17% of Naselle River discharge. Using this relationship, the Bear River contributes about 3% of the total freshwater input to Willapa Bay. River input to Willapa Bay is strongly seasonal, with winter discharge approximately two orders of magnitude greater than summer discharge.

Circulation in Shoalwater Bay is tidally driven, with significant spring-neap variations in tidal amplitude. Salinity is variable and depends primarily on freshwater input, generally ranging from 15–21 PSU during winter and 21–28 PSU during summer (Boldt et al., 2012). Stratification in channels during the winter and spring is moderate, with a salinity range of approximately 4 PSU between near-surface and near-bed waters. During the summer, the water column is well-mixed and stratification is minimal. Modeling studies indicate that circulation within the central and northern parts of Willapa Bay is influenced by river discharge, although these effects are less important in Shoalwater Bay (Banas and Hickey, 2005).

The regional climate of southwest Washington is characterized by dry summers and mild, wet winters. Precipitation measures approximately 2 m annually and is highly seasonal,

with less than ten percent of the annual precipitation falling between the months of July and September. Regional wind directions also vary seasonally, with predominantly southerly winds during the winter and northerly winds during the summer. As a result of the location of the study site in Willapa Bay, winter winds generally blow over fetch- and depth-limited waters, and summer winds blow over greater fetch. Winds are active throughout the year, although extreme wind events occur primarily during the winter (Boldt et al., 2012). Swell is minimal in Shoalwater Bay. Waves are generated by local wind forcing and despite being limited in height and period they are effective in transporting sediment (Andrews, 1965).

2.3 Methods

Data are presented from three seasonal instrument deployments made between March 2009 and January 2010 to measure currents, SSC, and salinity. Small stainless-steel tripods were equipped with 5 MHz SonTek Hydra acoustic Doppler velocimeters (ADVs), D&A Instruments Optical Backscatter Sensors (OBS), and Sea-Bird CTDs. Sample volumes were located nominally 30 centimeters above bottom (cmab). During the July 2009 and December 2009 deployments, upward-looking 2 MHz Nortek Aquadopp acoustic Doppler current profilers (ADCPs) were also used to measure water-column velocities. In addition, an upward-looking 1200 kHz RD Instruments ADCP was deployed in Bear channel and an upward-looking Aquadopp was deployed on the adjacent flat (Fig. 2.1) during the December 2009 deployment. SSC measurements in Bear channel were obtained from a long-term deployment tripod located on the channel flanks. Data results and processing methods for the long-term deployment are described in Boldt et al. (2012). For all deployments, OBS voltage was calibrated to SSC in the laboratory using sediment from collocated sediment traps ($r^2 > 0.89$). OBS data were inspected manually and spurious values caused by biofouling or water-borne debris were deleted or interpolated. Despite routine sensor cleaning, biofouling of the channel OBS invalidated a portion of the SSC data from the July deployment. SSC above the maximum sensor response during the December deployment is reported as the maximum recorded by the instrument.

Six-minute bursts of 2 Hz samples were collected by the ADVs every half hour during the March and July Deployments. Two-minute bursts of 25 Hz samples were collected every

ten minutes during the December deployment. The upward-looking ADCPs collected two-minute averages of velocity data throughout the water column every ten minutes. ADV data were quality-controlled using a minimum correlation score of 70%.

Water depth was computed using the ADV pressure sensor plus the instrument height off the bed. During the December deployment, water depth was computed using the Aquadopp pressure sensor because of its proximity to the bed. The time evolution of bed elevation was determined from the distance-to-boundary measurement reported by the ADVs in C channel and its adjacent flat. Bed elevation data for Bear channel were obtained from the long-term tripod.

In the channel, data measured by the upward-looking ADCP were segmented by depth-averaging velocities in bins either below or above the surrounding flat surface. These data are presented using the designations "below-flat channel" and "above-flat channel." Velocity data are presented in a channel-wise coordinate system in which the axes have been rotated to align with the channel orientation at the instrument deployment location (Fig. 2.1). In December, when instruments were deployed in both C and Bear channels, each channel/flat instrument pair was rotated according to the alignment of its respective channel.

Unit-width water transport was computed as the depth-integrated velocity for the area of interest (below-flat channel, above-flat channel, and flat). Unit-width sediment flux was computed as the water transport multiplied by the measured SSC. In this scheme, SSC is assumed to be well mixed throughout the water column. This assumption is warranted based on the good agreement between measured flat and channel SSC (Fig. 2.2) along with profiling OBS data from channel occupations (not shown). Processes active below the minimum measurable water depth threshold (< 30–40 cm) may be important to water and sediment flux budgets, and a worst-case model was used to fill in the low-water data gaps to test the sensitivity of our results. The model assumed continuous ebbing velocities and maximum observed SSC values throughout the period of instrument emergence. While magnitudes were affected, trends were not, and results are presented from the data as measured.

The terms "flood dominant" and "ebb dominant" in relation to calculated water and sediment flux are used throughout this paper. Ebb dominance corresponds to positive time-

integrated along-channel flux. Flood dominance is obtained when this quantity is negative. This definition is an expansion of the traditional usage in relation to velocity. To minimize confusion, the usage of flood or ebb dominance in the ensuing sections always refers to water or sediment flux, not velocity.

Bottom stress was calculated using ADV data with the near-bed Reynolds stress method during periods without wave contamination. Friction velocity u_* was computed using the ADV burst data:

$$u_* = \sqrt{-\overline{u'w'}}.$$

When waves were present, a wave-current interaction model (Madsen, 1994) was employed to estimate friction velocity from the combination of both waves and currents. The wave parameters and wave-orbital velocities were determined from the ADV velocity and pressure data using a PUV scheme.

Wind was measured at the study area with a weather station mounted on a navigational piling. While the wind speed sensor was active throughout all deployments, the wind direction vane was inoperational during the December deployment. Wind direction data for this period were obtained from the WSU AgWeatherNet station on the Long Beach peninsula, 6 km WSW of the study site (Fig. 2.1); the wind direction from this station and the on-site station were compared during periods of overlapping data and found to agree well. Wind stress was computed using measured wind speed following Yelland et al. (1998). Precipitation data for all deployments were obtained from the AgWeatherNet station.

2.4 Results

2.4.1 Characteristic processes

To evaluate the effects of external forcing mechanisms on flow and sediment transport in Willapa Bay, we first describe the characteristic evolution of these parameters in C channel and its adjacent flat during a calm period with no precipitation, spanning two spring tidal cycles (24.8 hours) during December 2009 (Fig. 2.2). We then describe the variations from this characteristic tidal cycle as observed during the seasonal deployments.

Velocity and bed stress

At low water, the flats were exposed and water depth in the channel was shallow (often 15 cm or less). Valid velocity measurements began when channel water depth was approximately 25 cm (Fig. 2.2), at which time upstream flow measured 3–5 cm s^{-1}. Flow speed steadily increased to approximately 20 cm s^{-1} as channel depth approached 1 m, when water began to flood the flats. When the flats were inundated with 15–20 cm of water, currents in the channel reached a maximum of 40–60 cm s^{-1} and channel friction velocity u_* reached a maximum of more than 1 cm s^{-1}. Peak speed during this high-speed pulse

This high-speed pulse was relatively short lived, with peak speeds lasting about 30 minutes and returning to approximately 20 cm s^{-1} within an hour. As water level continued to increase, below-flat channel speed decreased and direction remained approximately channel-aligned until stagnation at high water. Flow direction on the flat was approximately aligned with channel flows throughout the flood.

During the early part of the ebb, flow along the channel axis was minimal, and was instead aligned with larger-scale tidal forcing toward the northwest. Below-flat channel speeds typically did not exceed 10 cm s^{-1} for most of the early ebb, but flows in both the above-flat channel and flat reached 20–30 cm s^{-1}. Flows in the above-flat channel and flat had significant across-channel components, with direction oriented toward the northwest. As water level continued to fall, flow was generally across-channel until water level was almost equal with the flats, at which time another velocity pulse within the channel occurred. Channel speeds increased to 40–60 cm s^{-1} with u_* values near 1 cm s^{-1} and flow direction again was aligned with the channel axis. Speeds decreased as water level continued to fall within the channel and flow remained channelized.

Averaged over all the tidal cycles within the deployments, average speeds during floods were greater than during ebbs. During periods of calm winds, ebb-pulse speeds were greater than flood-pulse speeds, but the flood pulse lasted longer than the ebb pulse.

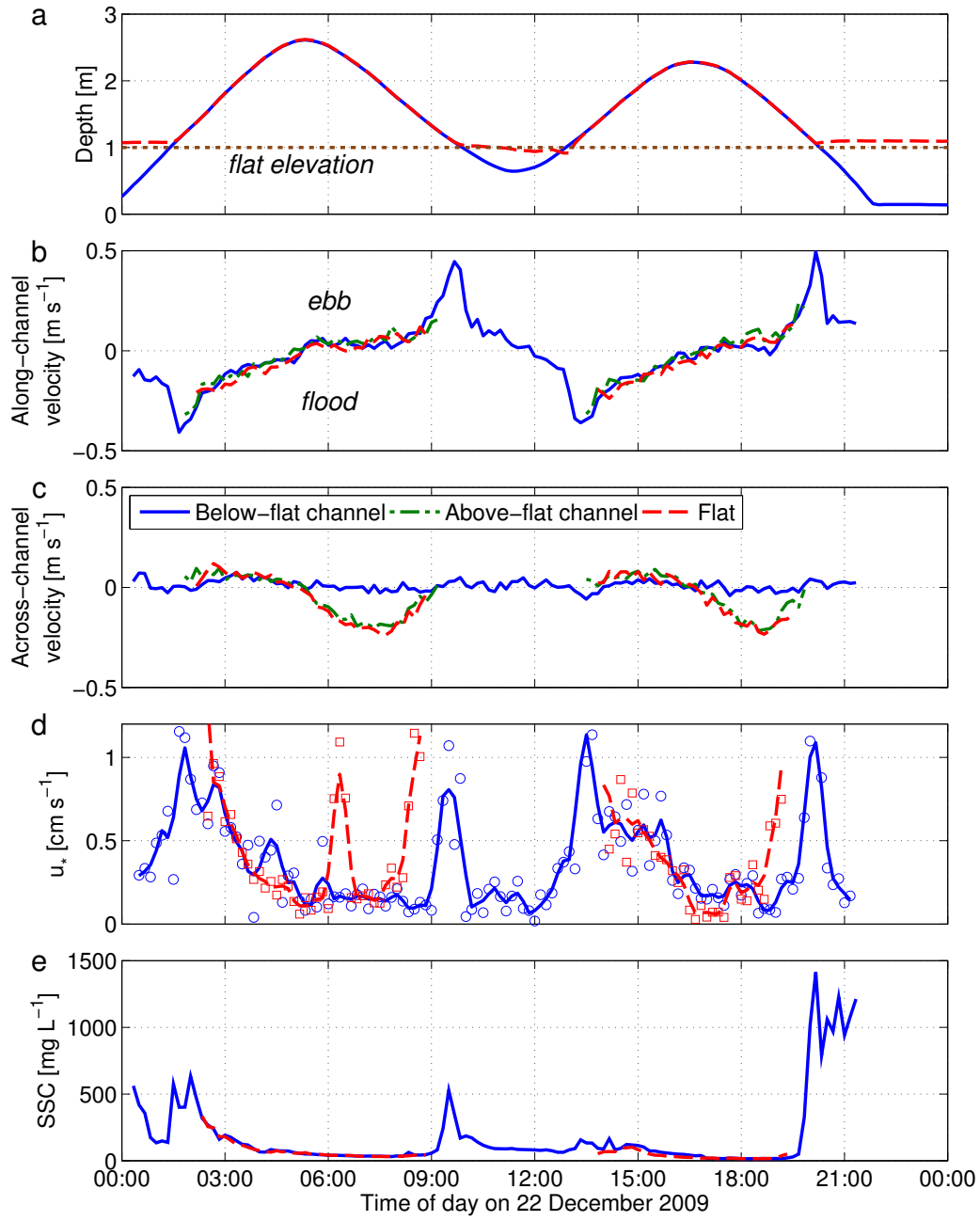

Figure 2.2: Timeseries of two typical tidal cycles in C channel and adjacent flat during the December 2009 deployment. (a) Channel (solid) and flat (dashed) water depth (horizontal dotted line indicates flat elevation). (b) Along-channel and (c) across-channel velocity in the below-flat channel (solid), above-flat channel (dash-dot), and flat (dashed). (d) Friction velocity (u_*) in the channel (circles) and flat (squares) computed using Reynolds stresses. Heavy lines indicate running averages. (e) SSC in the channel (solid) and flat (dashed).

Suspended sediment

SSC values during the early flood ranged from 10-100 mg L^{-1}. Just prior to and during the flood velocity pulse, SSC was approximately 500 mg L^{-1} and then slowly declined to about 50 mg L^{-1} at high water. SSC continued to decrease during the beginning of the ebb, attaining a minimum of 10–20 mg L^{-1} approximately halfway between high and low water. During the latter half of the ebb, SSC slowly increased until about twenty minutes prior to the ebb velocity pulse, when SSC rapidly increased to 500–1000 mg L^{-1}. On lesser ebbs with relatively small tidal ranges, SSC values were reduced to below 100 mg L^{-1} during low water; on greater ebbs, SSC remained high for the duration of sensor inundation. When water levels were sufficient to inundate both channel and flat OBSs, measured SSC was similar at both locations.

Considering all the tidal cycles within the deployments, SSC was lower during neap periods than spring periods in both the channel and flat. Minimum background SSC was greater in March and December, both periods of relatively high winds and river discharge, than during July, when winds were calm and river discharge minimal.

Water and suspended-sediment flux

Unit-width water transport trends in the channel were similar to velocity trends, being strongly pulsed on both flood and ebb (Fig. 2.3a, b). Averaged over a spring-neap tidal cycle, below-flat channel transport was greater during floods than ebbs, driven by higher flow speeds throughout the duration of the flood. Across-channel water transport was minimal in the below-flat channel, although it was sizable in the flat and above-flat channel, particularly during ebbs.

When averaged over all the tidal cycles within the deployments, the flux of water and sediment was southeastward on the flood, aligned with the channel and toward the interior of the flat complex. Ebb transport did not follow the channel and was instead north-northwestward until after water levels were near the flat elevation and water was forced to exit via the channel (Fig. 2.3).

Along-channel sediment flux associated with the pulses was the most significant signal

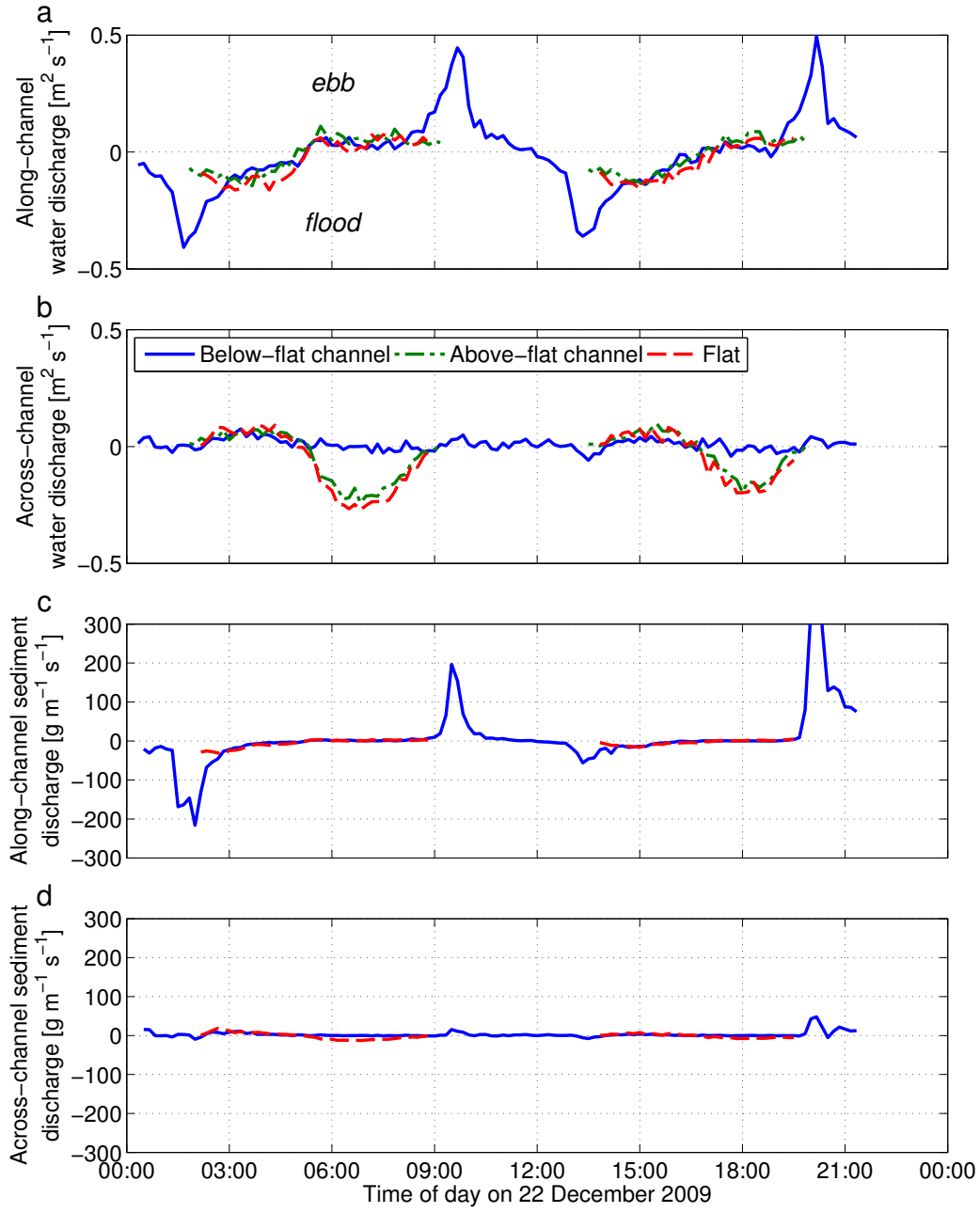

Figure 2.3: (a) Along-channel and (b) across-channel water transport in the below-flat channel (solid), above-flat channel (dash-dot), and flat (dashed). (c) Along-channel and (d) across-channel sediment flux in the below-flat channel (solid) and flat (dashed). The plot limits are the same as in Fig. 2.2.

in the sediment flux record (Fig. 2.3c, d). Consistent with the velocity and water transport observations, the sediment-flux flood pulse was more diffuse and had a longer-duration peak than the ebb pulse. Sediment flux magnitudes on the flat were significantly smaller than in the channel because of a shorter period of inundation and a lack of tidal pulses. Across-channel sediment flux in both the channel and the flat was small relative to along-channel flux.

2.4.2 Variability from characteristic processes

Here we describe variability from the characteristic tidal cycle described in the previous section, as observed during the March, July, and December deployments. In particular, we note the daily, fortnightly, and seasonal influences of tidal range, wind, precipitation, and river discharge.

March 2009

Both calm and stormy conditions were present during the 13-day March deployment. The first five days of the deployment were calm and had near-zero residual unit-width water transport within the channel, although sediment flux was flood dominated. Concurrently on the flat, water and sediment fluxes were slightly flood dominated compared to residual values in the channel. No precipitation was recorded during this period, river discharge was constant, and wind speeds generally were less than 8 m s^{-1}.

Following the initial calm period, a three-day storm that included rainfall, winds, and increased river discharge was observed. The first day of the storm consisted primarily of precipitation and intermittent winds and did not significantly alter sediment flux. An increase in flood dominance of water transport, coincident with the transition from spring to neap tidal regime, also began at this time. The second day of the storm was characterized by rain and high winds. Water transport on the flood was enhanced and ebb transport was diminished. Sediment flux was also strongly flood dominated, and minimum SSC values rose from pre-storm levels of 20 mg L^{-1} to over 200 mg L^{-1} during the storm. On the flat, across-channel transport was enhanced in the direction of the wind stress, which was toward the

NNW. In the days following the storm, residual sediment flux returned to values comparable to those before the storm. During the last four days of the deployment, which were calm and occurred during neap tides, enhanced flood dominance of water transport, reduced diurnal variability of sediment flux, and near-zero residual sediment flux were present.

Minimum SSC during spring tides was approximately 50 mg L^{-1}, while on neaps the minimum was approximately 10 mg L^{-1}, and SSC was elevated during the storm. Integrated over the entire deployment, velocity and unit-width water and sediment fluxes were flood dominated.

July 2009

The July 2009 deployment took place over 11 days during a period characterized by calm winds and minimal precipitation. Minimum SSC was lower than was observed in March and ranged from 5–10 mg L^{-1}. Overall, water transport and velocity were slightly flood dominated. Similar to the observations during the March 2009 deployment, water transport became more strongly flood dominant during neap-tide periods. Residual sediment flux in the channel during periods of valid OBS data was slightly ebb dominated, while on the flat the sediment flux was slightly flood dominated.

December 2009

The December 2009 deployment took place over 40 days in December 2009 and January 2010 (Fig. 2.4), which encompassed both calm and wet, stormy conditions. A total of 40 cm of rainfall led to increased riverine sediment delivery and frequent high winds led to wave-induced sediment resuspension.

C channel The minimum SSC in C channel during December ranged from 10–200 mg L^{-1} and was correlated with wind speed and tidal range. The first five days (days 345–349) of the deployment consisted of calm winds and no precipitation, and residual water and sediment fluxes were approximately zero. Three windy periods (wind speeds 12–15 m s^{-1}), each lasting several hours, were accompanied by 5 cm of total rainfall during days 349 and 350. Water and sediment fluxes were flood dominant for the duration of the storm, which took

place during spring tide conditions. After the storm, residual flux was less flood dominant compared to the storm period. Another wind and rain storm on days 355–357, during neap tides, corresponded to a slight increase in the flood dominance of water transport but no similar trend in the sediment flux. Several additional storms were observed for the duration of the deployment, each generally corresponding to an increase in the flood dominance of water and sediment fluxes in the channel.

As observed during the March and July deployments, tidal variation in sediment flux was smaller during neap tides and larger during spring tides. Flood dominance of water transport was increased during neap tides, although the strong and frequent storms during the deployment make the separation of fortnightly signals challenging.

Bear channel As in C channel, flow was aligned with the channel axis on the early flood, when water level was below the flat elevation. As water level rose in Bear channel, flow velocity increased steadily and reached a maximum about one hour before high water. Velocity trends during the early ebb were similar to those in C channel, in which flows in the below-flat channel were minimal, and appreciable flow did not occur until late in the ebb.

Velocity pulses similar to those in C channel were observed within Bear channel. They were longer in duration (60–90 minutes) than in C channel and only occurred during greater ebbs, when water level fell below the lower-elevation flats near Bear channel. Obvious flood velocity pulses were not observed in Bear channel.

Within Bear channel, unit-width water transport was flood dominated (Fig. 2.4c), and flood dominance increased during wind events, a trend consistent with C-channel observations. While mean speeds in Bear channel were 50% faster than in C channel (24 cm s^{-1} and 16 cm s^{-1}, respectively), the greater unit-width transport was primarily driven by the depth of Bear channel. The temporal unit-width transport trends in Bear channel were similar to those in C channel (Fig. 2.4a, c).

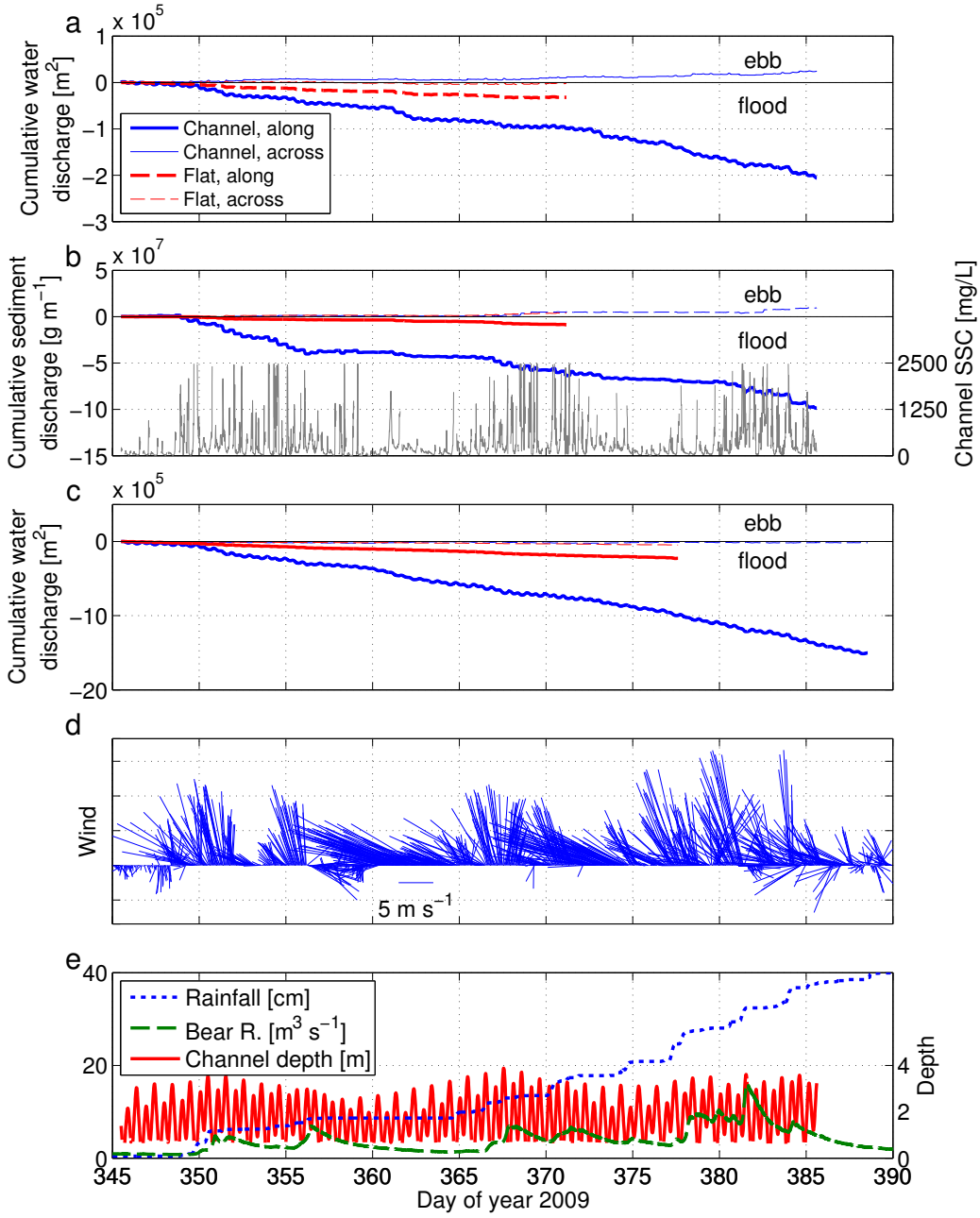

Figure 2.4: Data from the December 2009 deployment. (a) Along-channel and across-channel cumulative water transport at C channel and C flat stations. (b) Along-channel and across-channel cumulative sediment flux at C channel and C flat stations, and channel SSC. (c) Along-channel and across-channel cumulative water transport at Bear channel and Bear flat stations. (d) Wind vectors. (e) Cumulative precipitation, river discharge, and channel water depth.

2.5 Discussion

As in most intertidal environments, tides are a primary control on Willapa system dynamics, although this forcing and its interaction with bathymetry and external stresses are complex. In general, the hydrodynamics of the system are under either local or large-scale control depending on water level relative to flat elevation. Wind and precipitation alter system dynamics, sometimes to the extent that their effects dominate tidal and bathymetric controls. We discuss the interrelated roles of these external stresses in the following sections.

2.5.1 Tidal pulses

Pulse mechanics

For a given location on a tidal flat, one-dimensional depth-averaged tidal currents can be estimated by applying conservation of mass (e.g., Friedrichs and Aubrey, 1996):

$$\frac{\partial h}{\partial t} + \frac{\partial (hu)}{\partial x} = 0, \tag{2.1}$$

where h is water depth and u is tidal velocity, with the assumption that the tidal excursion is much shorter than the tidal wavelength and the water surface rises and falls uniformly across the region. Spatial integration of Eq. 2.1 landward of the location of interest yields

$$u = \frac{x_f - x_0}{h} \frac{\partial h}{\partial t}, \tag{2.2}$$

where x_f is the boundary between wetted and exposed portions (i.e., where depth is equal to zero), and x_0 is the location of interest. By assuming no across-channel flow and neglecting flow concentration within the channel, the average velocity through a channel/flat cross section can be estimated by multiplying by the cross-sectional width b:

$$u = \frac{S}{A} \frac{\partial h}{\partial t}, \tag{2.3}$$

where $S = b(x_f - x_0)$ is the wetted surface area landward of the cross-sectional area and $A = bh$ is the cross-sectional area. As water depth increases in the channel, A and S gradually get larger until water level is equal to flat level. The shallow bed gradient of the flats and the small channel size relative to the flat area drive a more rapid increase of S than

A when the flats flood, producing a velocity pulse. The duration of the pulse is controlled by the relationship between S and A with respect to h, as velocity in Eq. 2.3 is maximized when water depth over the flats is shallow.

Despite the complex flow patterns and bathymetry of Willapa Bay, our observations are generally consistent with Eq. 2.3. The velocity pulse occurs in C channel at a well-defined water-surface elevation dictated by the flat level (Fig. 2.5). Every tidal cycle exhibits velocity pulses, except those during neap tides when the water surface stays above the flat elevation. On floods, the velocity pulse occurs when the flats are inundated with approximately 20 cm of water (Fig. 2.5a). On ebbs, it occurs when the water surface is within 10 cm of flat level. The pulse is also associated with elevated SSC (Fig. 2.5b).

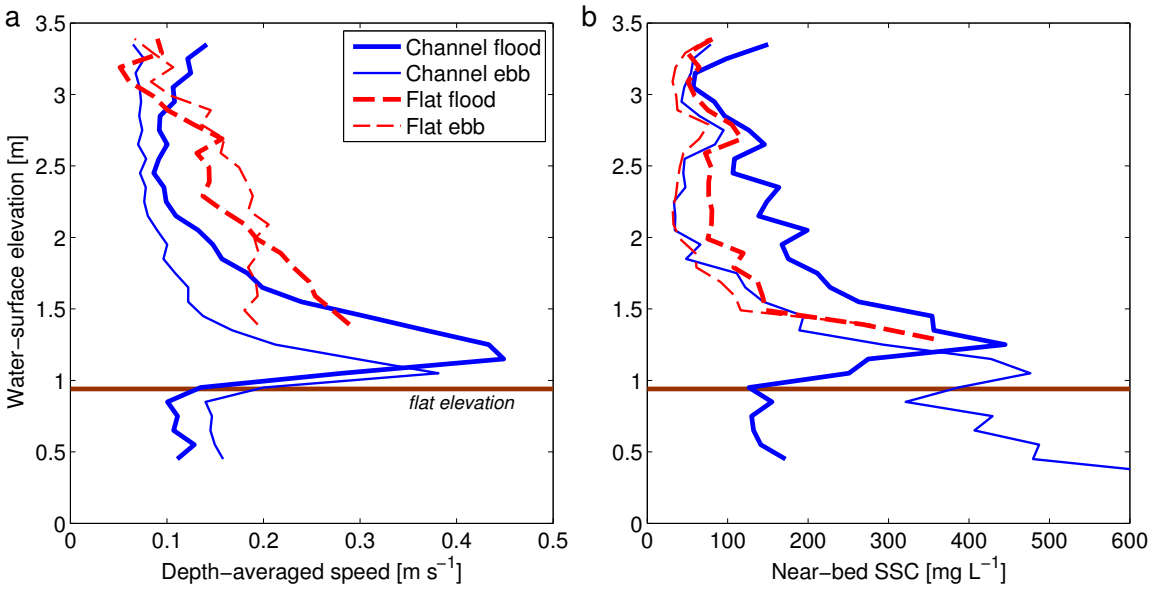

Figure 2.5: (a) Median depth-averaged speed and (b) median near-bed SSC versus water-surface elevation in the below-flat channel (solid) and flat (dashed). Flood data are indicated with thick lines; ebb data are indicated with thin lines. The horizontal line indicates the flat elevation.

When ignoring the pulse, C channel velocity is approximately in quadrature with water-surface elevation, which suggests a standing tidal wave. As such, non-pulse tidal flow speed is a function of $\partial h/\partial t$ (Fig. 2.6; red and blue points) and by extension tidal range. Pulse h

(or S/A) is limited to a small range of values, and here Eq. 2.3 predicts that the magnitude of u should be a function of $\partial h/\partial t$, as observed (Fig. 2.6; black-circled points). Furthermore, pulse $\partial h/\partial t$ is not markedly different from non-pulse values (Fig. 2.6) but pulse flow velocity is considerably higher. This again suggests that (a) large S/A produces the pulse instead of maximum or peak in the $\partial h/\partial t$ time series, and (b) $\partial h/\partial t$ sets the pulse magnitude as predicted by Eq. 2.3.

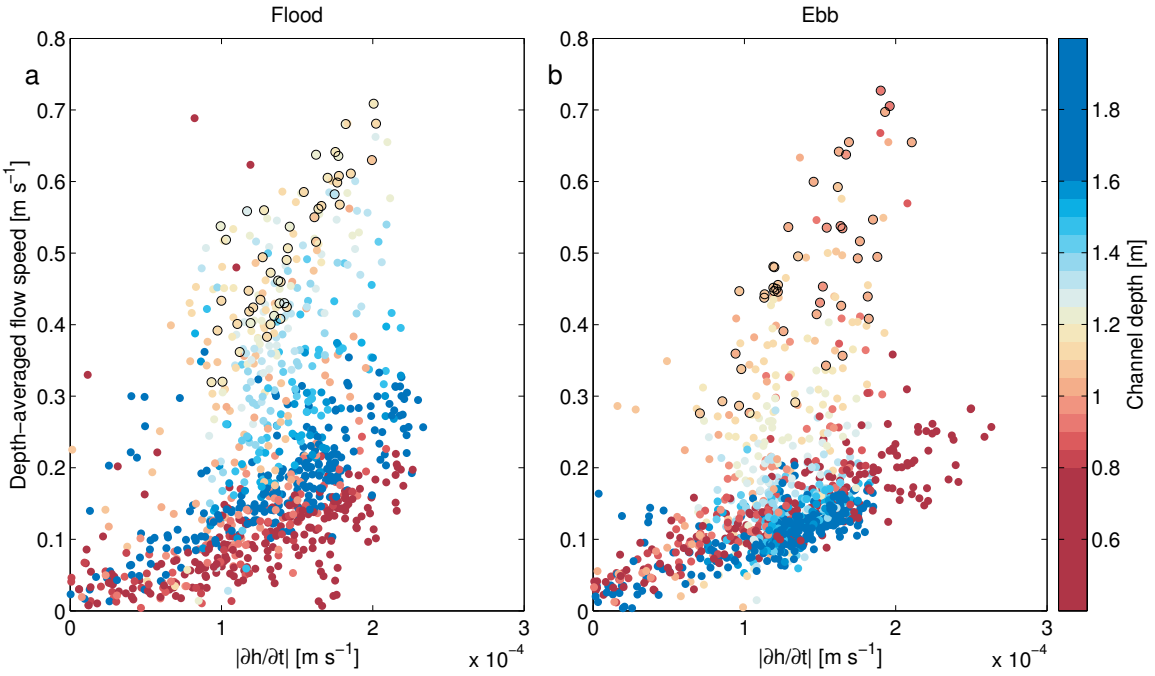

Figure 2.6: Absolute value of temporal water-surface gradient ($|\partial h/\partial t|$) vs. flow speed in C channel during the December 2009 deployment for (a) flood and (b) ebb. Colors indicate water depth. Black-circled points denote peak velocity during pulses. Only channel water depths between 0.5 and 2 m are plotted and a nonlinear colormap is used to emphasize differences in flood and ebb pulse elevations.

As described earlier, the flood pulse occurs when water depths are greater than flat elevation instead of when water level crosses the flat as Eq. 2.3 would predict. We can still use Eq. 2.3 to investigate these offsets by relaxing the assumption that changes in water-surface elevation occur everywhere uniformly and immediately. Because the pulse is not produced by a spike in $\partial h/\partial t$, a different functional relationship of S/A and h on floods and

ebbs is a potential factor in setting the pulse elevation. Bottom friction is a likely mechanism to alter this relationship because it slows the spread of flooding water over the flats and a corresponding S/A increase until a higher stage than without friction. Similar flood-pulse delays in salt marshes have been attributed to vegetative friction (French and Stoddart, 1992) or to travel-time delays (Fagherazzi et al., 2008). Here we see that the combination of unvegetated tidal flat bottom friction and travel time are sufficient to similarly delay the flood pulse until water level is above the flat elevation. On ebbs, bottom friction within the shallowing NNW flow may allow nearby channels to serve a more prominent role in draining the flats earlier than they would without friction and produce the pulse at a higher stage. In contrast, pulses in salt marshes do not occur until stage is below the marsh elevation (e.g., French and Stoddart, 1992), and vegetative friction (French and Stoddart, 1992) and travel-time effects (Fagherazzi et al., 2008) have been used to explain the delay of ebb pulses in salt marshes.

Temporal dynamics

Flow speeds quickly increase prior to both the flood and ebb pulses, but the increase starts later and is more rapid for the flood pulse (Fig. 2.7a). While speeds decrease after both pulses, the decay is less significant after the flood pulse, and flow velocity after the flood pulse (depth > 1.4 m; Fig. 2.6a) is greater than before the flood pulse (depth < 1.0 m; Fig. 2.6a) for a similar range of $\partial h/\partial t$ values. This could suggest that reduced impact of bottom friction in deeper flows allows for faster flow speeds for a given $\partial h/\partial t$. After the ebb pulse, the converse is true. Even though $\partial h/\partial t$ can be large during the shallow-water period after the ebb pulse (Fig. 2.6b; red colors), flow velocity is generally less than about 0.24 m s^{-1}. This could be due to increased effects of bottom friction in these shallow-water flows. As a result, channel speeds after the flood pulse are higher than they are after the ebb pulse.

Increased mean flow speeds associated with the pulses are accompanied by elevated shear velocity (Fig. 2.7b). Maximum shear velocity is maintained for 10–20 minutes after the flood pulse and gradually decays, although it remains significantly higher than after the ebb pulse. Differences in the patterns of SSC relative to shear velocity allow us to infer

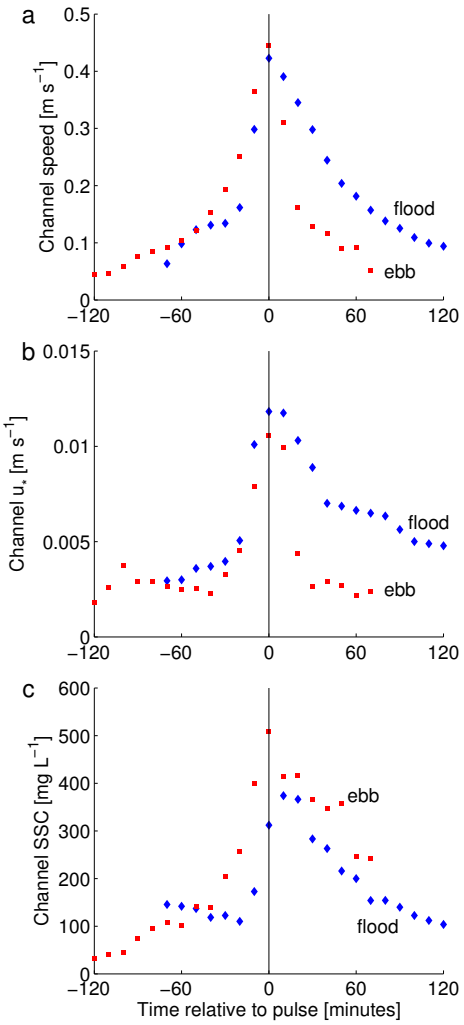

Figure 2.7: Temporal evolution of (a) speed, (b) friction velocity (u_*), and (c) SSC in C channel with respect to time of the velocity pulse (at zero minutes). Median values are plotted relative to the flood (diamonds) and ebb (squares) velocity pulses during the December 2009 deployment. Only data measured during calm winds (< 7 m s^{-1}) are included in the analysis.

relationships between SSC and local resuspension. Prior to the flood pulse, SSC is relatively low but increases rapidly, reaching its maximum just after peak velocity (Fig. 2.7c). After the pulse, channel SSC decreases but remains elevated compared to pre-pulse conditions. Sediment resuspension in the channel from high bed stress (Fig. 2.7b) could be a contributor to the sustained SSC after the flood pulse. Channel SSC after the flood pulse is also higher than concurrent flat observations (Fig. 2.5b). Because bed stresses in the channel and on the flat are similar after the flood pulse (Fig. 2.2d), the SSC difference could be explained by resuspension of more easily erodible (Wiberg et al., 2012) channel bed sediment compared to more resistant flat sediment. Once remobilized, the channel sediment is a source for landward fluxes on floods. On the ebb, SSC slowly builds and reaches its maximum during the pulse. After the ebb pulse, SSC remains high despite the rapid decay of u_* (Fig. 2.7b, c), suggesting delivery of sediment-laden water from draining flats and upstream channel flanks as water's edge processes resuspend (Hsu et al., 2012) and advect sediment to and through the channel.

Bear channel Compared to C channel, the ebb pulse in Bear channel is longer lived, occurs at a lower stage, and is not as strong relative to mean flow velocity. The first two characteristics are consistent with Bear channel's larger drainage area and the lower elevation of the flats that surround it. The third could suggest that the difference in A between Bear and C channel is greater than the difference in S Eq. 2.3, resulting in a weaker pulse in Bear channel (Eq. 2.3). Alternatively, it could imply that because of larger S, frictional and travel-time effects are more important to Bear channel pulse dynamics, and that the assumptions of Eq. 2.3 are less suitable than they are for C channel.

Pulse significance

Because the pulse occurs at moderate depth ($\sim$1 m), it is an important component of the water transport budget of C channel (Fig. 2.3a). We conservatively associate pulse transport with the 15 minutes before and after the peak of each pulse. For the December deployment, the ebb pulse accounts for 33% of total along-channel ebb water transport, while temporally accounting for just 8% of ebb data. On floods, the pulse represents 21% of the total flood

transport, again representing 8% of the time.

In Bear channel, the ebb pulse is less important but still a significant component of the along-channel water budget, representing about 17% of total ebb transport. This may be an underestimate because of the longer duration of the ebb pulse in Bear channel.

The greatest SSC values were measured during or just after the velocity pulse (Fig. 2.5b, 2.7). Because maximum velocity and SSC occur at similar times, sediment transport associated with velocity pulses is an important component of the total suspended-sediment budget of C channel. Using the same pulse definition as above, ebb pulses represent 46% of total ebb along-channel sediment flux, and on floods, pulses account for about 23% of the total flood sediment flux. Also, the pulse could serve an important role in maintaining tidal-flat channel geometry because the greatest bottom stresses in the channel are generated then.

2.5.2 Meteorological effects on tidal-flat dynamics

Wind

Wind influences the flow regime, generates waves, and modifies SSC in both channels and flats. Strong winter winds blow from the S or SE, which is approximately orthogonal to the axis of C channel (Fig. 2.8a), and is the direction of minimum fetch in Shoalwater Bay (Fig. 2.1).

Average flat and above-flat-channel speeds increased during windy periods (Fig. 2.8b, d). At the flat, average flow speed during moderate to strong winds (above 7 m s^{-1}) was 38% faster than during calm winds. At the above-flat channel, flow speed during winds was about 27% faster than during calm conditions. Winds were less effective at altering flow at the below-flat channel, where flow speed increased by 17% during windy periods (Fig. 2.8c).

Wind also altered flow direction at the flat and above-flat channel and steered it in the direction of the wind forcing (Fig. 2.8). On ebbs, flow direction (NNW during calm conditions) was aligned with the direction of the wind forcing (approximately NW). On floods, flow was deflected clockwise at the flat and above-flat channel. Flow direction in the below-flat channel was not altered significantly on floods, although on ebbs it went from

being channel-aligned during calm winds to approximately parallel with wind forcing during windy periods.

Wind also modified the intensity I of the pulse, defined as

$$I = \frac{u_{pulse}}{\left(\frac{\partial h}{\partial t}\right)_{pulse}}, \tag{2.4}$$

where u_{pulse} is pulse speed and $(\partial h/\partial t)_{pulse}$ is the temporal water-surface gradient during the pulse. When neglecting external forcing, I should not vary between pulses because u_{pulse} is balanced by $(\partial h/\partial t)_{pulse}$ (Eq. 2.3). During windy conditions, however, I was inversely related to wind speed on ebb pulses ($r^2 = 0.61$) and weakly but positively related to wind speed on flood pulses ($r^2 = 0.44$), suggesting that meteorological forcing alters the effective relationship between S/A and h. Ebb-pulse intensity decreased by 28% during windy periods compared to calm periods, corresponding to a flow-velocity decrease of 0.14 m s^{-1} for a typical $(\partial h/\partial t)_{pulse}$ value of 1.4×10^{-4} m s^{-1}. Flood-pulse intensity increased by 18%, corresponding to a flow-velocity increase of 0.09 m s^{-1} for the same typical $(\partial h/\partial t)_{pulse}$ value. The reduction of the ebb-pulse intensity with wind may result from prolonged and enhanced wind-driven drainage of water northward across the flats (Fig. 2.8) prior to flow concentration into channels. We speculate that the augmented flood pulse could result from wind resistance on water flooding the flats from the north, forcing increased tidal exchange via secondary channels along the eastern flank of the flats (Fig. 2.1).

Wave heights were related to wind speed (Fig. 2.9a), suggesting that waves are locally generated by wind and swell does not reach the study area. Wind-generated currents (Fig. 2.8) or greater apparent roughness from the wave-current boundary layer increased u_{*c} (Fig. 2.9b) to values greater than those during calmer periods. The combination of wind-driven flow and wave-orbital motion increased combined wave-current shear velocity (Fig. 2.9c), supplying additional bottom stress to erode and resuspend bed sediment.

As a result of wind-driven waves and currents, minimum SSC was higher during windy periods than calm periods, and SSC was functionally related to u_{*wc} (Fig. 2.10a, b). In the channel, u_{*wc} sets a minimum bound on observed SSC (Fig. 2.10a), and variability above the minimum is driven by advection from elsewhere in the channel network and local resuspension. While local resuspension is important in the channel when the flats

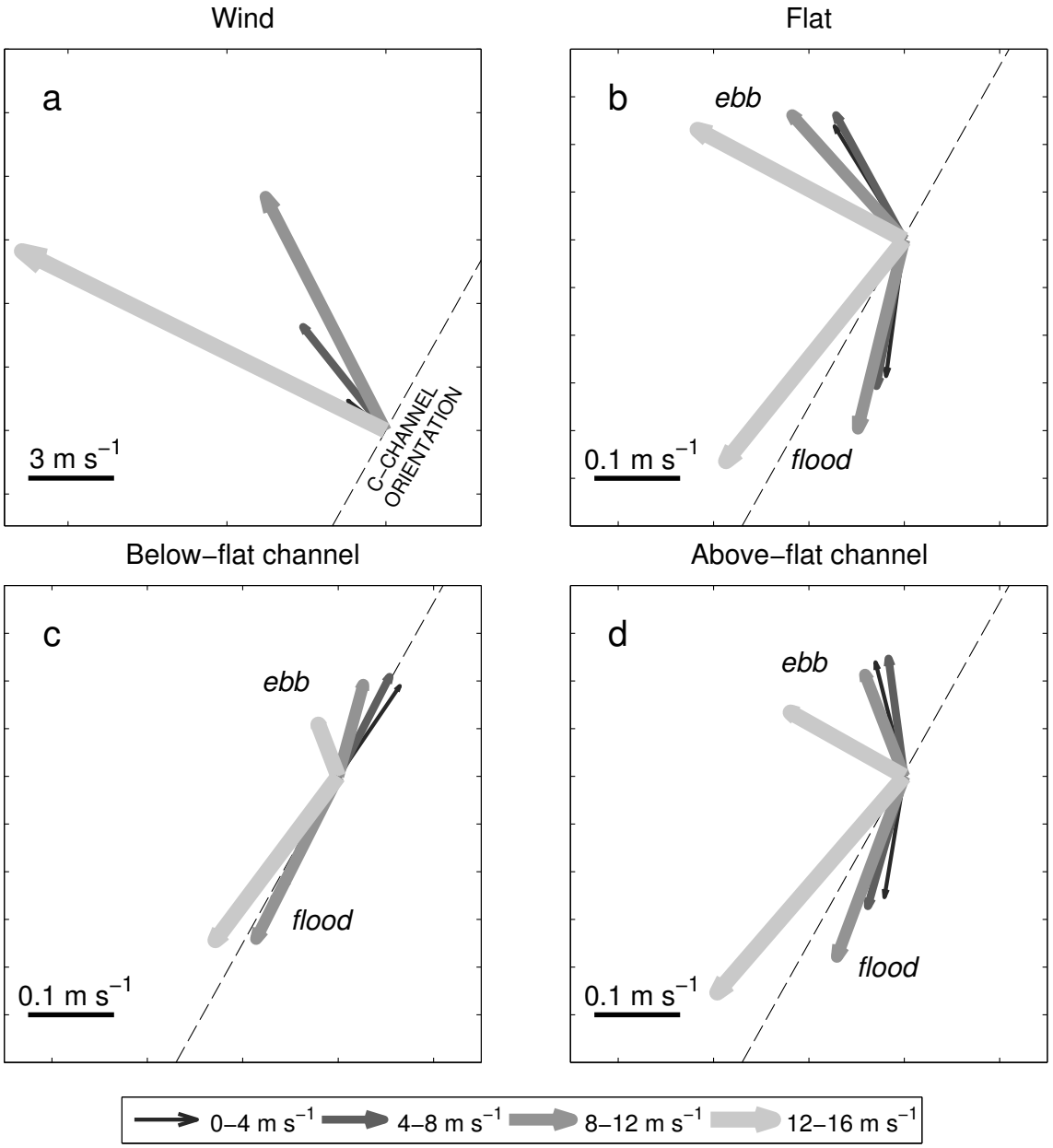

Figure 2.8: (a) Average wind vectors binned by speed. Average flow-velocity vectors for ebb and flood binned by wind speed at (b) flat, (c) below-flat channel, and (d) above-flat channel. Vector thickness corresponds to wind speed segmented into 4 m s^{-1} bins as measured during the December deployment. Dashed lines show alignment of C channel.

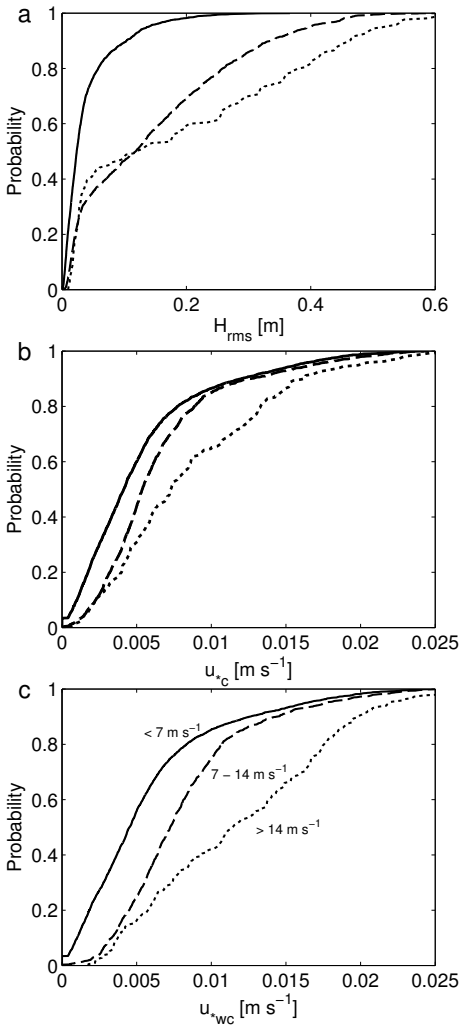

Figure 2.9: Cumulative distribution functions of wave heights and channel bed shear velocities under different wind regimes during the December 2009 deployment. (a) RMS wave height (H_{RMS}). (b) Current shear velocity (u_{*c}). (c) Wave-current shear velocity (u_{*wc}). Solid lines indicate winds less than 7 m s^{-1}, dashed lines from 7 to 14 m s^{-1}, and dotted lines above 14 m s^{-1}. Data presented in (b) and (c) were computed following Madsen (1994).

are flooded and during tidal pulses, advection also provides sediment to locations within the channel, particularly at lower water levels. On the flat, SSC is more directly related to u_{*wc} (Fig. 2.10b), suggesting that local resuspension and advection of sediment resuspended elsewhere on the flats (which should experience similar u_{*wc}) are the important processes in determining SSC. These results highlight the different sedimentary processes active in the channel and flat at different water levels and phases of the tidal cycle.

Wind stress is an effective means of predicting minimum SSC (Fig. 2.10c). Minimum SSC increased linearly with wind stress in both the channel and flat for wind stress above 0.075 Pa (corresponding to a wind speed of 7 m s^{-1}). This threshold suggests that minimum SSC during calm winds is dependent on advection, resuspension from tidal forcing, and sediment characteristics, while during windy periods minimum SSC is controlled by resuspension by waves and wind-driven currents. Despite these complicated relationships, significant information about the minimum turbidity of this shallow-water system can be gained simply by measuring the wind speed. For example, at wind stresses greater than 0.4 Pa ($\sim$15 m s^{-1}) at least 150 mg L^{-1} of sediment will be in suspension regardless of the tidal phase or water level. These results confirm those found in other muddy tidal-flat environments (Dyer et al., 2000b; Lee et al., 2004) and suggest a dynamic system in which SSC varies based on immediate, localized forcing in addition to riverine sediment delivery.

Precipitation

In Willapa Bay, wind events can occur without precipitation, but heavy winter precipitation events are almost always accompanied by strong wind. Here we focus specifically on the influence of precipitation. Rainfall increases freshwater and sediment inputs to Willapa Bay by way of river flooding, and the seasonal relationship between SSC and riverine sediment delivery is described in Boldt et al. (2012). This discussion focuses on a rain storm from 14–16 December that was accompanied by winds reaching nearly 15 m s^{-1}, making this storm typical in the data record. Unique to this storm was the delivery of 2 cm of rainfall onto exposed flats at low tide over approximately seven hours (Fig. 2.11), making it the most intense and longest-lived rain-on-flat event of the data set. Rain-on-flat events occur

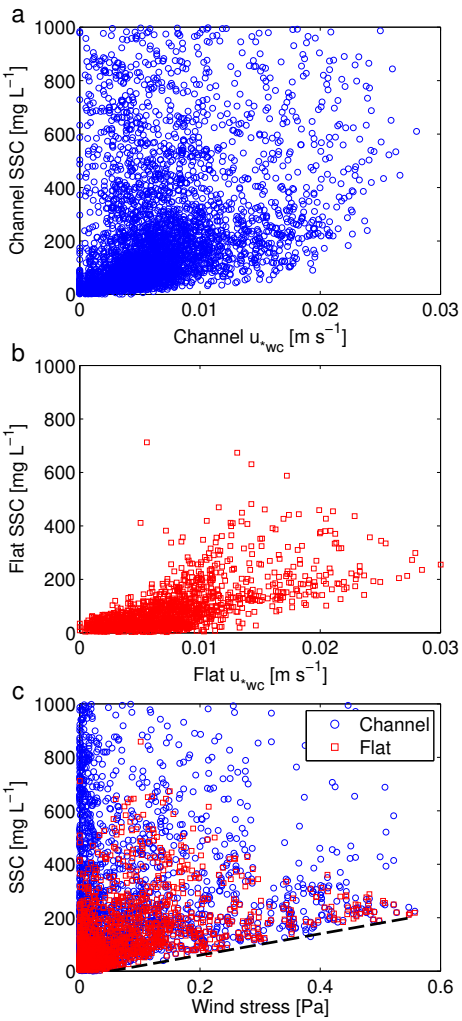

Figure 2.10: Relationship of SSC to total bed stress and applied wind stress during the December deployment. (a) Combined wave-current shear velocity vs. C channel SSC. (b) Combined wave-current shear velocity versus flat SSC. (c) Wind stress versus SSC in C channel (circles) and adjacent flat (squares). Dashed line indicates relationship between background concentration and wind stress.

with some frequency over partial flat exposure periods as storms are not correlated with daily tidal fluctuations.

Minimum SSC after the rain-on-flat event was 80 mg L^{-1} compared to 10–20 mg L^{-1} during the tidal cycle preceding the storm, consistent with the observed high winds (Fig. 2.10, 2.11). Additionally, C channel bed elevation increased by approximately 5 mm over the two tidal cycles following the rain-on-flat event (Fig. 2.11b). Bear channel bed elevation also increased modestly, gaining about 3 mm (Fig. 2.11b). In contrast, C flat bed elevation decreased by about 2 mm (Fig. 2.11c). After the storm passed, a reduction in bed elevation of approximately 4 mm in C channel and 5 mm in Bear channel was observed. SSC in both channels and the flat gradually decayed toward pre-storm conditions, although they remained somewhat elevated, likely because of increased supply from river flood input. Flat bed elevation slowly increased during the same period and approached the pre-rain condition during the days after the storm.

These observations suggest that a rain-on-flat event of sufficient magnitude can be an important eroder and mobilizer of flat sediment. In addition, they show that rain-detached sediment is delivered and stored within channels. Other rainfall events at higher water levels that did not fall directly on flats did not alter bed elevation, suggesting that the changes were not due to increased riverine sediment supply. Likewise, while waves and wind-driven currents are important in maintaining sediment in suspension, wind-only events were not observed to produce bed elevation changes of magnitude similar to those of the large rain-on-flat event. Less intense rain-on-flat events likely erode amounts of sediment smaller than the altimeter can reliably detect. That the bed elevations returned to their pre-storm values within several days suggests that while direct rain impact can be important to short-term system dynamics, the system may be able to return to its previous state relatively quickly. Nevertheless, enhanced sediment cycling from direct rain impact increases readily transportable sediment, augments existing landward sediment transport processes, and can modify the sea bed.

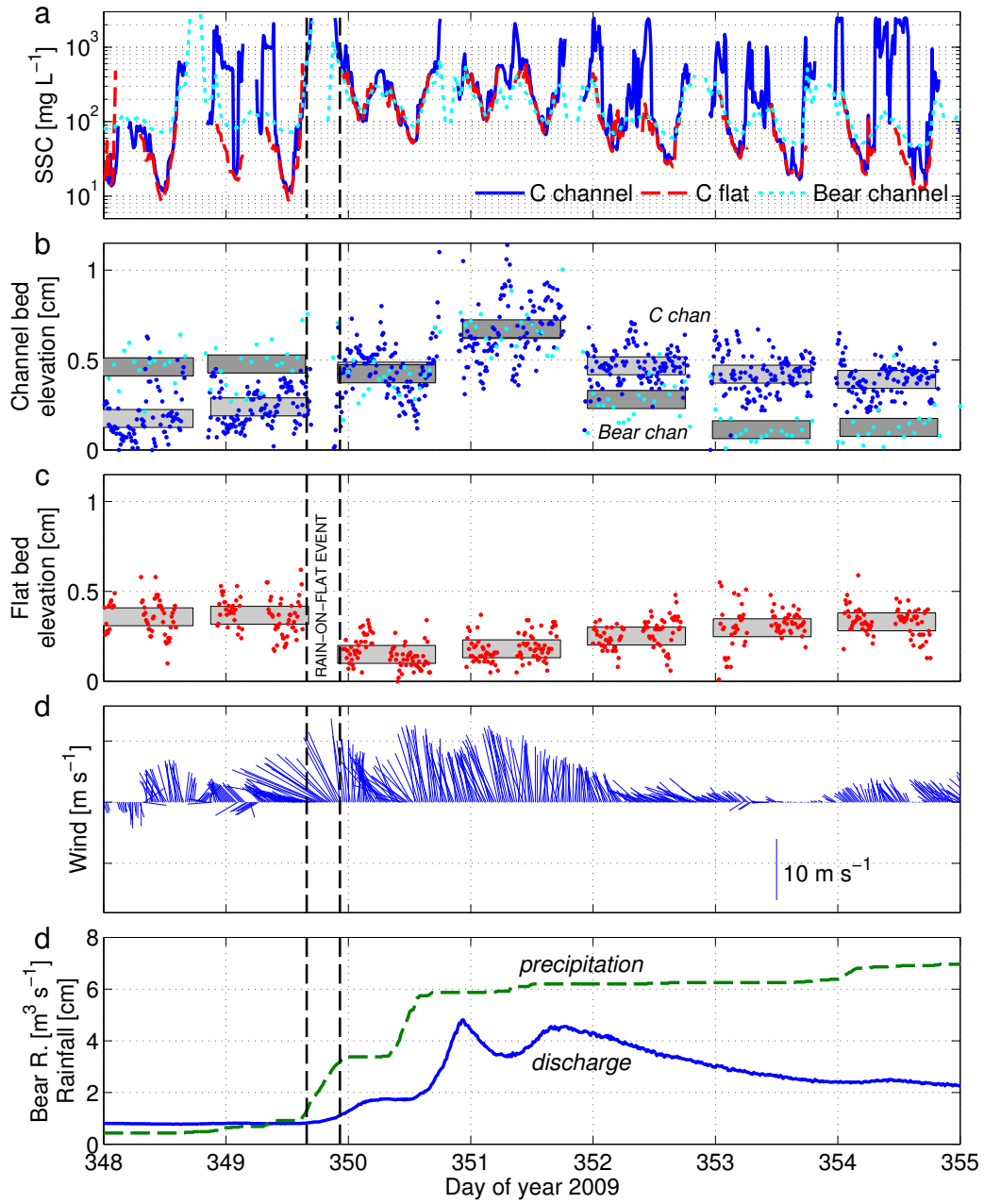

Figure 2.11: December rain-on-flat event with period of rainfall onto exposed flats indicated by dashed lines. (a) SSC in C channel (solid), C flat (dashed), and Bear channel (dotted). (b) Bed elevation in C channel (blue points and light boxes) and Bear channel (cyan points and dark boxes). (c) C flat bed elevation. (d) Wind vectors. (e) Bear River discharge (solid) and cumulative precipitation (dashed). To help identify trends, averages of the individual data points are indicated by shaded boxes.

2.5.3 Water and suspended-sediment budget

Along-channel flood dominance is the overarching theme of the residual water and sediment flux of the locations monitored in Willapa Bay (Table 2.1), and therefore the channels and nearby flats serve to direct flow and sediment to the flat interior. During calm periods, residual along-channel water flux in C channel and flat is generally an order of magnitude larger than across-channel flow, which is positive (toward the SE). Across-channel July results depart from this pattern, potentially because of localized variability in morphology that alters the definition of the channel coordinate system. Storms enhance along-channel upstream water flux by 89–165% in C channel and 51–370% on the adjacent flat. In Bear channel the relative influence of storms was generally less than in C channel. Storms increased residual along-channel flood water transport in Bear channel by only about 26% over calm. During stormy periods, residual across-channel flows in the channel and flat were generally larger and negative, redirecting southeastward fluxes under calm conditions toward the NW. Across-channel flows at Bear flat increased by 167%. These results reflect the influence of wind-generated flow and reduced ebb-pulse intensity. Increased upstream water flux and greater SSC enhanced residual upstream sediment transport by a factor of 2.7 to 3.8 in the channel during stormy periods.

Flood-oriented transport of sediment in intertidal areas is regularly observed (e.g., Postma, 1967; Pejrup, 1988; Christie et al., 1999; Le Hir et al., 2000) and is enhanced by settling lag and scour lag effects (Postma, 1967). Wind waves generally enhance ebb transport of sediment as they keep sediment in suspension that otherwise would have settled out at high water (Dronkers and van de Kreeke, 1986), and our results contrast with previous studies in which wind events enhanced ebb sediment transport (Christie et al., 1999; Dyer et al., 2000b). Landward sediment flux in C channel is largely due to flow direction asymmetry, where material is pumped on floods through the channel network from the east to the flat interior and is drained on ebbs by Shoalwater Bay-scale tidal circulation to the NW.

Our observations are consistent with modeling (Hsu et al., 2012) and radiochemical (Boldt et al., 2012) studies of Willapa Bay but stand in contrast to the results of Mariotti

Table 2.1: Residual water and sediment fluxes for the three deployments. Data are rotated to the channel-wise coordinate system as shown in Fig. 2.1c.

	Residual water flux ($m^2\ d^{-1}$)				Residual sediment flux ($g\ m^{-1}\ d^{-1}$)			
	Channel		Flat		Channel		Flat	
	Along	Across	Along	Across	Along	Across	Along	Across
March 2009								
all data	-4.82×10^3	-4.21	-1.34×10^3	2.39	-3.97×10^5	-1.27×10^3	-6.78×10^4	2.75×10^4
calm	-4.36×10^3	9.48	-1.26×10^3	1.37×10^2	-2.98×10^5	1.92×10^4	-6.99×10^4	5.51×10^4
storm	-8.24×10^3	-1.08×10^3	-1.90×10^3	-8.18×10^2	-1.14×10^6	-1.57×10^5	-5.06×10^4	-1.79×10^5
July 2009								
all data (calm)	-1.81×10^3	-7.12×10^2	-1.31×10^3	-6.94×10^2	–	–	–	–
December 2009								
C channel								
all data	-5.14×10^3	6.25×10^2	-1.26×10^3	-6.18	-2.47×10^6	2.38×10^5	-3.43×10^5	1.59×10^5
calm	-3.35×10^3	1.29×10^3	-6.42×10^2	6.18	-1.59×10^6	3.56×10^5	-1.72×10^5	1.33×10^5
storm	-8.89×10^3	-7.78×10^2	-3.02×10^3	-4.14×10^2	-4.29×10^6	-1.00×10^4	-8.28×10^5	2.33×10^5
Bear channel								
all data	-3.49×10^4	-3.87×10^2	-7.03×10^3	-1.48×10^3	–	–	–	–
calm	-3.24×10^4	-2.20×10^2	-7.00×10^3	-1.00×10^3	–	–	–	–
storm	-4.10×10^4	-7.55×10^2	-7.39×10^3	-2.67×10^3	–	–	–	–

and Fagherazzi (2012), who found channels in Willapa Bay to be ebb dominated with respect to water and sediment fluxes. This discrepancy can be accounted for in part by noting the different morphology surrounding the studied channels. The study area of Mariotti and Fagherazzi (2012) was located in an area of constrained large-scale circulation, within 500 m of the eastern boundary of Shoalwater Bay. That location contrasts with C channel, whose headwaters are Shoalwater Bay's expansive inner flats. Further, ^{210}Pb data show the flats of Willapa Bay accumulate sediment at a rate consistent with local sea-level rise (Boldt et al., 2012), and landward, flood-dominant residual sediment flux is a mechanism to accommodate this gain of sediment.

Somewhat more speculatively, the flood dominance of flow in Bear channel may also be influenced by the balance between the wind stress and the pressure gradient in channels of varying depth. Long basins aligned with the direction of the wind forcing, as is roughly the case for Bear channel during SE wind events, exhibit along-wind flow in the shallows, where wind stress overwhelms the pressure gradient. A net reverse flow occurs in deeper areas where the opposite is the case (Csanady, 1973), resulting in a flood-oriented residual water flux.

2.6 Conclusions

We measured fluxes of water and sediment during three focused deployments over the course of ten months in Willapa Bay, Washington. Our observations in both primary and secondary channels in this mesotidal mudflat system lead to the following conclusions:

- Interaction between the morphology of the channel/flat complex and water-level variations produces well-defined velocity pulses during both flooding and ebbing tides. SSC trends are also largely set by the same morphologic control. Pulse-related transport processes represent about 27% of the water budget and 35% of the suspended-sediment budget of the observed secondary channel while making up only 8% of the deployment time. Maintenance of continuity in the channel/flat complex produces the velocity pulse, and its magnitude is set by tidal range or, equivalently, $\partial h/\partial t$.

- Wind increases minimum SSC via wind-generated waves and currents and is a signif-

icant short-term control on SSC. Wind alters the flow regime in channels and flats and augments flood dominance of channels through enhanced over-flat ebb flow and smaller ebb pulses. During windy periods, ebb-pulse intensity decreased by 28% while flood-pulse intensity increased by 18%.

- A direct rain-on-flat event eroded 3 mm of flat sediment and formed a 5-mm sediment deposit over the ensuing tidal cycles. Direct rain impact on flats could be one mechanism by which winter-time channel sediment deposits (Boldt et al., 2012) are formed.

- Along-channel water and sediment transport were flood dominant at all the measurement locations. Residual upstream water transport during storms was 1.9–2.7 times greater, and sediment flux was 2.7–3.8 times greater, during storms than calm periods.

Chapter 3

SEDIMENT TRANSPORT IN AMAZONIAN TIDAL FLOODPLAINS

3.1 Introduction

Approximately one third of the suspended sediment discharged by major rivers may be trapped between the head of tides and the river mouth (Amazon: Meade 1994; Nittrouer et al. 1995; Mertes et al. 1996; Dunne et al. 1998; Ganges-Brahmaputra: Goodbred and Kuehl 1998). In many large rivers, a considerable portion of this tidal region is also freshwater, and is referred to as the tidal river. Tidal rivers can extend for hundreds of kilometers and pass through many of the world's major cities, but their impacts on fine-sediment transfer remain understudied compared to adjacent fluvial and estuarine environments. In addition, sedimentary studies in those adjacent environments often overlook processes occurring within the tidal river, rendering it a missing link in the transport of sediment from terrestrial source to marine sink. These factors motivate the study of sediment transport, entrapment, and release in the tidal river.

Processes in tidal rivers likely demonstrate both fluvial and marine characteristics, or a unique coupling of both suites of processes. Like non-tidal lowland rivers, tidal rivers can have large floodplains which are periodically inundated by changing water levels. There may be sizable gradients in flow velocity, temperature, and suspended-sediment concentration (SSC) across the mainstem–floodplain transition, the magnitudes of which can exceed heterogenity along the entire mainstem (Tockner et al., 2000). The interface between the mainstem and the floodplain has been termed the "perirheic zone" (Mertes, 1997), and is an important and dynamic environment of large river systems. In fluvial systems, a dynamic equilibrium of exchange between the river and floodplain is controlled by the "flood pulse" (Junk et al., 1989), and river discharge determines the connectivity and transfer of material within and between the two environments. During periods of low discharge, connectivity is low between the mainstem and floodplain. During periods of rising stage, water and

material may advect through crevasses, openings which form in a natural river levee, and material may also be transferred from the mainstem to the floodplain by overbank flooding. As in purely fluvial systems, overbank flow is important in the tidal river during high seasonal discharge. In additional to the seasonal water level, variations in tidal water height determine whether and when overbank flow can occur.

Semi-diurnal or diurnal variations in water-surface elevation are the most obvious marine characteristic of tidal rivers, and are superimposed on the rise and fall of the seasonal discharge. Along with stuttering or reversing flow in the mainstem, tidal action forms channels which incise the natural river levee and tidal floodplain, especially in regions with large tidal range. These tidal channels are an important method in addition to overbank flow by which water and sediment are transferred through the tidal perirheic zone.

Within tidal channels, water level, flow velocity, temperature, and SSC all vary during the tidal cycle. Water level rises and falls with the tide and results in tidal currents that transport water and material into and out of the tidal floodplain. One velocity characteristic found in intertidal channels is the "tidal pulse," a velocity transient caused by the interaction between water level and channel morphology which was first observed in tidal creeks in the 1960s (Myrick and Leopold, 1963; Pestrong, 1965). While most observations of the tidal pulse have been made in salt-marsh channels (Boon, 1975; Bayliss-Smith et al., 1979; Healey et al., 1981; French and Stoddart, 1992; Allen, 1994), it has also been documented in mangrove creeks (Wolanski et al., 1992) and tidal flats (Mariotti and Fagherazzi, 2011; Hill et al., 2013; Nowacki and Ogston, 2013), and the importance of the tidal pulse to the overall water and sediment transport of channels varies by environment. There is little literature, however, concerning the tidal pulse in freshwater tidal channels connecting to vegetated floodplains such as those on the lower Amazon.

Temperature in tidal channels in a variety of environments has received less attention, primarily because the effects of salinity generally far outweigh those of temperature in determining water density. In fluvial systems, however, the importance of temperature heterogeneity is well established, particularly with regard to its ecological implications. Temperature changes across the river-floodplain transition can be greater than those along the length of the mainstem (Tockner et al., 2000), and the geomorphology of a river sys-

tem can influence the temperature differences between environments (e.g., mainstem and floodplain) (Arscott et al., 2001).

In this paper, we present data from tidal channels that incise the floodplain of the tidal Amazon River. The data, which are the first published measurements of their kind on the Amazon, include water level, flow velocity, water temperature, and SSC during a range of seasonal discharge levels. Our objectives are to describe the sediment dynamics of these channels and how they vary along the tidal river and over various temporal scales (e.g., daily, seasonal). We investigate the thermal dynamics of the channels and their relation to sediment transport, explore the feedbacks among time scales and geomorphology, and develop an initial estimate of sediment exchange with the Amazonian tidal floodplain.

3.1.1 The lower Amazon River

The Amazon River is by far the largest river in the world in annual water (6300 km^3 y^{-1}) and sediment (1200 Mt y^{-1}) discharge (Milliman and Farnsworth, 2011). Discharge at Óbidos, the lowermost gauging station (Fig. 4.1), varies seasonally with high flow from April through June and low flow from October through November (Fig. 3.2a). Seasonal discharge varies by a factor of only two to four (Meade et al., 1979) because of the geographic extent of the Amazon basin and its wet-tropical setting. Spring tides approach 5 m at the mouth (Ponta do Céu) and decrease to zero near Óbidos, the canonical head of the tidal river, over 800 km upstream of the mouth(Fig. 4.1). The Amazon's immense freshwater discharge pushes salinity and associated estuarine processes onto the shelf (Gibbs, 1970), making it the longest tidal river on Earth. SSC at Óbidos also varies seasonally and is highest during rising water (Fig. 3.2b). As water approaches its highest seasonal level, SSC decreases. SSC remains low during falling water and through low seasonal discharge. The floodplain downstream of Óbidos has been posited to be a location of sediment trapping (Meade et al., 1979), and perhaps one-third of the of sediment discharged at Óbidos (a mass approaching the total sediment load of the Mississippi River) is deposited before reaching the ocean (Mertes and Dunne, 1988; Meade, 1994).

Figure 3.1: The tidal Amazon River from Óbidos to the mouth. Water-level gauges and instrument deployments described in the text are indicated. Distances from the river mouth are determined using Ponta de Céu as river km 0.

3.2 Methods

In this paper we present data collected during four research cruises on the tidal Amazon River from 2011 to 2014. Cruise dates targeted rising, high, falling, and low discharge of the Amazon and covered a 7.5 m seasonal water-level variation at Óbidos (Fig. 3.2a).

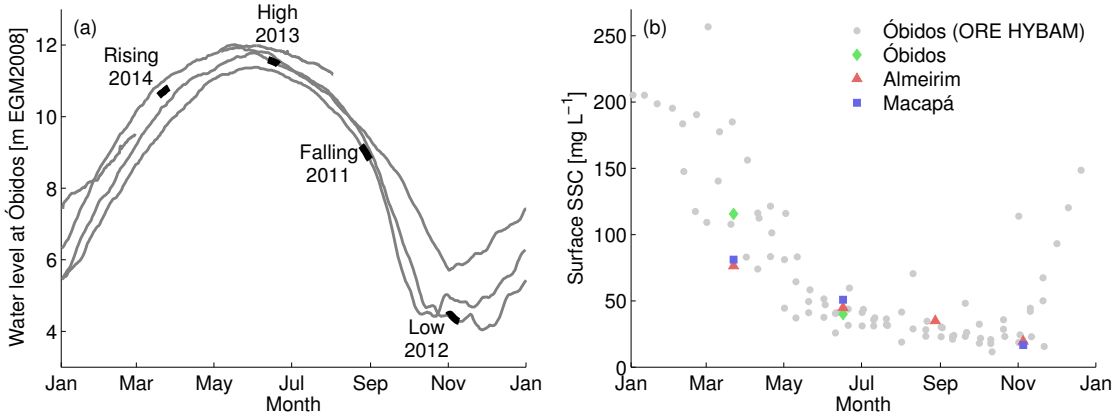

Figure 3.2: (a): Óbidos water level 2011–2014. Blackened sections indicate water level during cruises. Water level is estimated during the 2014 cruise, when the Óbidos gauge was inoperable. Data courtesy Agência Nacional de Águas. (b): SSC at Óbidos (dots and diamonds), Almeirim (triangles), and Macapá (squares). Óbidos (dots) are surface-water samples from 2006, 2007, and 2010 collected by the ORE HYBAM project; other data points were collected during the cruises described in this paper.

3.2.1 Tidal channels

A total of 11 instrument deployments were made in four floodplain-incising tidal channels along the Amazon tidal-river continuum. Three of the channels lie along the Amazon mainstem and are located: 440 km upstream of the mouth near the town of Almeirim; 300 km from the mouth near the confluence of the Cajari River, a small tributary of the Amazon; and 150 km from the mouth near the city of Macapá (Fig. 4.1). These three channels are hereinafter referred to as the "Almeirim," "Cajari," and "Macapá" channels, respectively. The fourth channel is about 200 km from the mouth and incises the floodplain of the Rio Jacaré Grande ("Jacaré"). It is located in a region known as the Estreitos de

Breves, a vast channel network that connects the Amazon to the Pará estuary. Although the Jacaré channel is not directly connected to the mainstem Amazon, the Estreitos de Breves are strongly influenced by the Amazon outflow (Vital and Stattegger, 2000a) and a portion (∼10%) of Amazon water and sediment likely flows through the Estreitos into the Pará River system (Fig. 4.1).

The channels were chosen to emphasize the changing influence of tidal and seasonal water-level changes, which vary along the tidal river (Kosuth et al., 2009). At the farthest upstream deployment location of Almeirim, the tidal range (0.2–1 m) was about an order of magnitude smaller than the seasonal range. Closer to the mouth at Macapá, the tidal range (2–3 m) was about three times larger than the seasonal range. The locations between these end-members have more parity between seasonal and tidal water-level fluctuations.

Bottom-mounted acoustic Doppler current profilers (ADCP; Nortek 2 MHz Aquadopp) with integrated optical backscatter sensors (OBS; Campbell Scientific OBS-3+) measured water level, flow velocity, water temperature, and SSC. During all deployments, the OBSs and temperature sensors measured at approximately 10 centimeters above bottom (cmab). Additional OBSs and temperature sensors were deployed at 50 cmab during some of the deployments.

Instruments were deployed for varying lengths of time during each cruise as dictated by logistical constraints. Typical deployment durations at all locations ranged from 12 to 24 hours. During the 2014 Macapá deployment, water level and SSC were additionally recorded for 12 days to investigate spring-neap variability.

Data from all instrumentation were inspected and spurious data points were removed. Velocity data from the ADCPs were rotated to a channel-wise coordinate system where positive along-channel velocity denotes ebbing flow (seaward) and negative values indicate flooding flow (landward). Water samples collected *in situ* were filtered to calibrate the OBS.

3.2.2 Mainstem temperature and SSC

In addition to the tidal-channel data, we present surface-temperature and SSC data collected by a vessel on the Amazon mainstem at stations near each tidal-channel mouth. Mainstem

water samples collected from the vessel during the tidal-channel deployments were filtered to compute SSC. Temperature data were from the upper 1 m of mainstem CTD casts completed during the tidal-channel deployments. When CTD data were not available, we present vessel-mounted ADCP thermistor data from when the vessel was within ∼200 m of the tidal-channel mouth.

3.2.3 Supporting data

Daily water-level data were obtained at Óbidos (courtesy of Agência Nacional de Águas) and Santana (courtesy of Instituto Brasileiro de Geografia e Estatística) (Fig. 4.1). Water levels measured at Óbidos were adjusted to the EGM2008 datum following Callède et al. (2013). Although the water-level datum at the Santana station is arbitrary (Instituto Brasileiro de Geografia e Estatística, 2012), we adjusted the water levels measured in the Macapá channel to the long-term Santana datum to compare water levels between deployments. *In-situ* and satellite SSC at Óbidos were obtained from the ORE HYBAM project (`http://www.ore-hybam.org/`).

3.3 Results

3.3.1 Almeirim

The Almeirim tidal channel is opposite the town of the same name, on the right bank of the Amazon mainstem (Figs. 4.1 & 3.3). The tidal channel is about 30 m in width and is surrounded on both sides by submerged and emergent aquatic vegetation that extends laterally for 60–100 m before reaching the mainstem levee. Instruments were deployed in the middle of the tidal channel, about 275 m from the edge of the mainstem channel. Depths in the tidal channel ranged from 1 to 4 m depending on the seasonal water level, and tidal variation was 0.3–1 m depending on deployment. Flow, temperature, and SSC dynamics varied with seasonal water level, and conditions were similar among the rising, high, and falling water cruises but dramatically different during the low-flow cruise. As a result, we group observations into those made during rising, high, and falling water and those during low water.

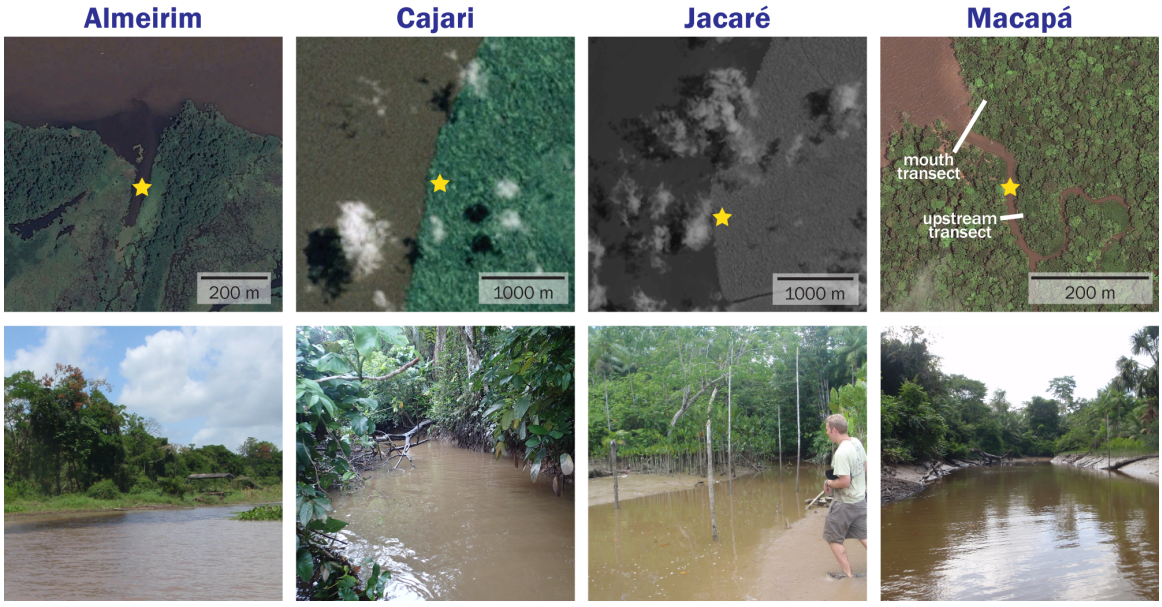

Figure 3.3: Top: satellite images of the four tidal channels discussed in this paper. Note different scales due to available imagery. Stars show deployment locations. Bottom: field photos looking into tidal channels from their mouths, where they connect with the mainstem Amazon River.

Rising, high, and falling seasonal water level

Mean tidal-channel depths during rising, high, and falling seasonal water level ranged from 1.5 to 3.5 m with tidal fluctuations of 0.2–0.3 m (Fig. 3.4a–c). Flood velocity quickly increased to a maximum of 0.15–0.3 m s^{-1} after low slack water. A rapid increase in temperature (1–2 °C) and SSC ($\sim$50 mg L^{-1}) generally accompanied the onset of the flood tide. After passage of the temperature front, temperature in the tidal-channel was equal to or greater than that of the mainstem, and SSC was about equal to that in the mainstem. Temperature and SSC remained high for the duration of the flood tide, even as flow slowed toward high slack water, a pattern indicative of temperature and sediment advection, not local resuspension. As flow reversed to ebb tide, velocity ranged from 0.1 to 0.2 m s^{-1}. During the ebb tide, temperature in the tidal channel was generally cooler than in the mainstem. Ebb-tide SSC steadily decreased and reached a minimum at low slack water.

In addition to the tidal forcing, wind sometimes modified the flow regime by producing local setup that reversed the flow direction briefly toward the end of the falling-water deployment (Fig. 3.4a).

Low seasonal water level

Dynamics during the low-water cruise reflected the larger tidal range and and higher elevation of the tidal floodplain relative to the mainstem water level. Water depth in the channel ranged from 0.15 m to 1.3 m, and the tidal wave was severely asymmetric (Fig. 3.4d). The strongly flood-dominated flow velocity exceeded 0.70 m s^{-1} on flood but only reached 0.25 m s^{-1} on the elongated ebb; both the velocity and the ebb duration were greater during this deployment compared to the other deployments at this location. While on flood the tidal-channel temperature reflected that of the mainstem, temperature increased on ebb as water about 3 °C warmer than the mainstem drained from the tidal floodplain. SSC was greater in the tidal channel than in the mainstem throughout the measurement period, and reached values of nearly $1,000$ mg L^{-1} in the tidal channel on the ebb, the highest observed at any location during all four cruises, and far higher than values in the mainstem ($\sim$ 30 mg L^{-1}). SSC also increased throughout the ebb, even as velocity slowed toward low slack

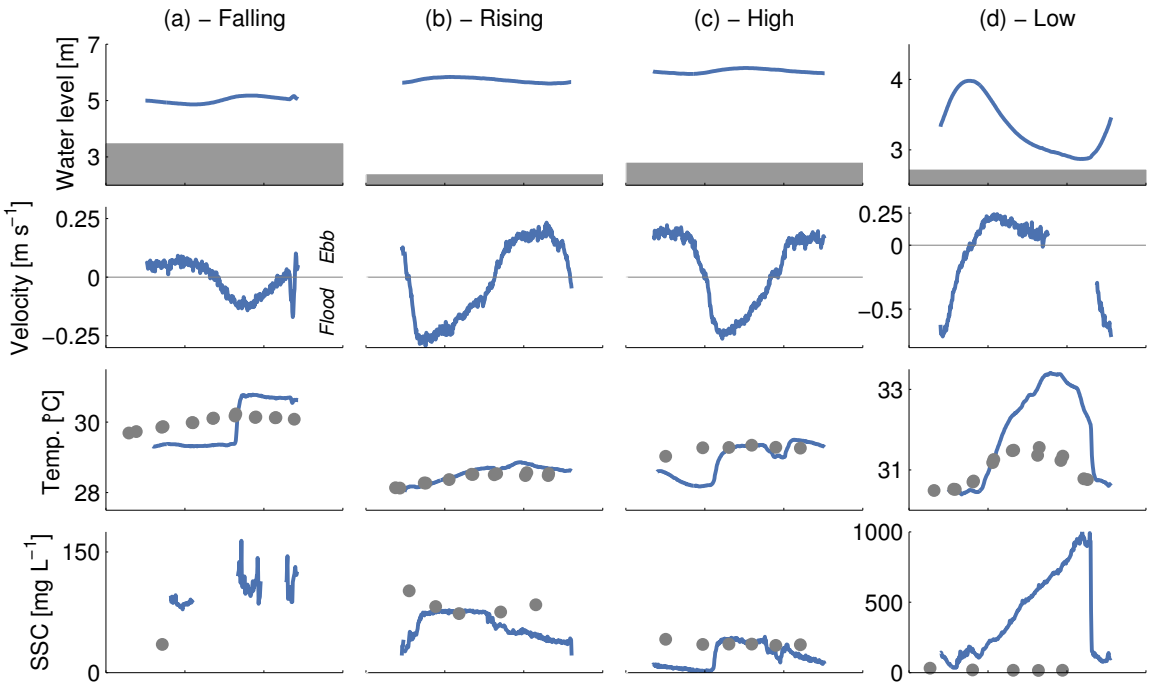

Figure 3.4: Timeseries of water level relative to EGM2008, flow velocity, temperature, and SSC for the four deployments at the Almeirim channel. Grey shaded regions in water-level plots denote the channel bed and dots show mainstem temperature and SSC. Note different y-axis ranges in (d).

water. When the tide turned from ebb to flood, temperature and SSC dropped rapidly as cooler, less sediment-laden water flowed back into the tidal channel from the mainstem.

3.3.2 Cajari and Jacaré

The Cajari tidal channel is located on the right bank of the Amazon mainstem, about 5 km upstream of the Cajari River mouth; the Jacaré tidal channel is located on the left bank of the Rio Jacaré near the village of Curumu (Figs. 4.1 & 3.3). The channels are 6–9 m wide and depths range from 0.5 to 2.5 m with tidal ranges of 1.3–1.7 m. Thick jungle vegetation surrounds the channels at both locations, and the elevation of the tidal floodplain is about 2.9 m above the channel bed at Cajari. Instruments were deployed in the tidal channels about 100 m from the mainstem banks. We describe the Cajari and Jacaré channels together in this section because of their similar distances from the mouth, tidal ranges, and behavior.

Cajari

Conditions at Cajari were similar to those during rising, high, and falling seasonal water level at Almeirim, though the larger tidal range (1.3 m) changed some characteristics. Flow speeds were faster, though still less than 0.4 m s^{-1}, and were stronger on flood tide(Fig. 3.5a). As at Almeirim, temperature and SSC both rapidly increased during the early flood tide and gradually decreased during ebb tide, and maximum temperature was approximately equal to that in the mainstem. In contrast to the Almeirim observations, SSC at Cajari was often higher than in the mainstem and had a short-lived peak at the beginning of the flood, perhaps because of resuspension from stronger tidal currents induced by the larger tidal range.

Jacaré

At Jacaré, maximum flow velocity was only about 0.25 m s^{-1} despite a tidal range of 1.7 m, though the tidal wave was less asymmetric than at Cajari (Fig. 3.5b, c). As at Almeirim and Cajari, temperature and SSC both increased at the beginning of the ebb. Temperature decreased throughout the ebb, as at the other locations, and maximum temperature was

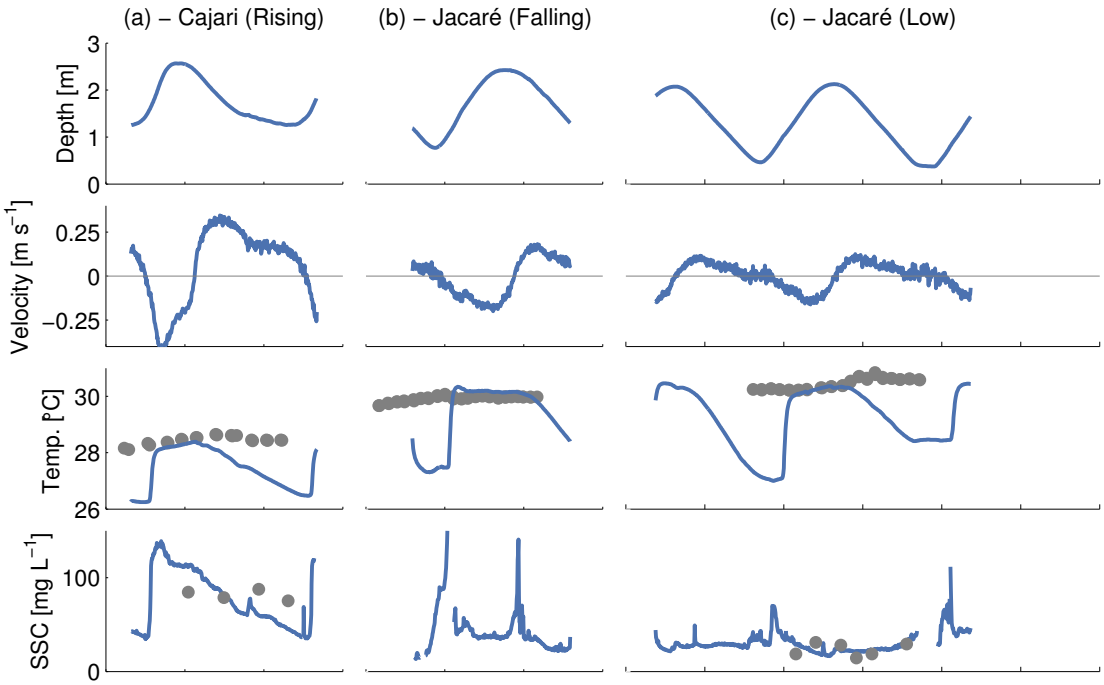

Figure 3.5: Timeseries of water depth, flow velocity, temperature, and SSC at the Jacaré and Cajari channels. Dots show mainstem temperature and SSC.

equal to mainstem temperature. The peak in SSC at the beginning of the flood was larger than at Cajari, and elevated SSC remained for the duration of the flood during the falling-water deployment. As at Cajari, SSC in the tidal channel was generally greater than in the mainstem. The peaks in SSC during slack-water periods seen here were not observed at Almeirim or Cajari.

3.3.3 Macapá

The Macapá channel is located on the right bank of the Amazon mainstem, opposite the city of Macapá (Figs. 4.1 & 3.3). Average channel width is 26 m and depth ranges from 1.5 to nearly 5 m depending on seasonal and tidal water level. Instruments were deployed in the channel about 275 m from the mainstem bank. Because of the hydrodynamic differences between them, we group deployments into those when water level inundated the tidal floodplain (rising and falling seasonal water level) and those that did not (low and high seasonal water level).

Floodplain inundated during deployment

During the two deployments when water inundated the floodplain, low slack water level was between 1.5 and 2 m (Fig. 3.6a, b), corresponding to a tidal-channel depth of about 0.9 m. SSC was lowest at low slack water and ranged from 20 to 65 mg L^{-1} depending on season and tidal range. After about 45 minutes of flood, temperature rose rapidly by 1.5–3 °C and SSC increased to a maximum of 100–275 mg L^{-1} and attained the highest values of the tidal cycle. The temperature and SSC front was thus a characteristic of all the instrumented channels. Flow velocity during the SSC and temperature increase was generally less than 0.2 m s^{-1}. As the flood progressed and flow velocity increased, SSC often decreased slightly. When water level reached about 4.6 m, the approximate tidal-floodplain elevation, flow velocity rapidly increased (referred to here as the tidal pulse) and reached nearly 1 m s^{-1}; SSC rose moderately during the tidal pulse. Velocity associated with the tidal pulse was confined to a 0.1 m range of water-surface elevation, between 4.6 and 4.7 m. SSC decreased as flow velocity slowed toward high slack water, and continued

to drop during the early ebb. When water level reached 4.2 m on the ebb, another velocity pulse occurred, and SSC increased 10–30 mg L^{-1} during the fastest flow as sediment was resuspended locally. As water level continued to fall, flow velocity and SSC decreased until both attained a minimum at low slack water. Toward the end of the ebb, water temperature decreased, though not as rapidly as it increased on flood.

Similar to the other locations, maximum water temperature was about equal to that in the mainstem, and ebbing water was generally about 2 °C cooler than the mainstem water. In contrast to the observations at Almeirim, but similar to those at Cajari and Jacaré, SSC tended to be greater than that in the mainstem, except during low slack water.

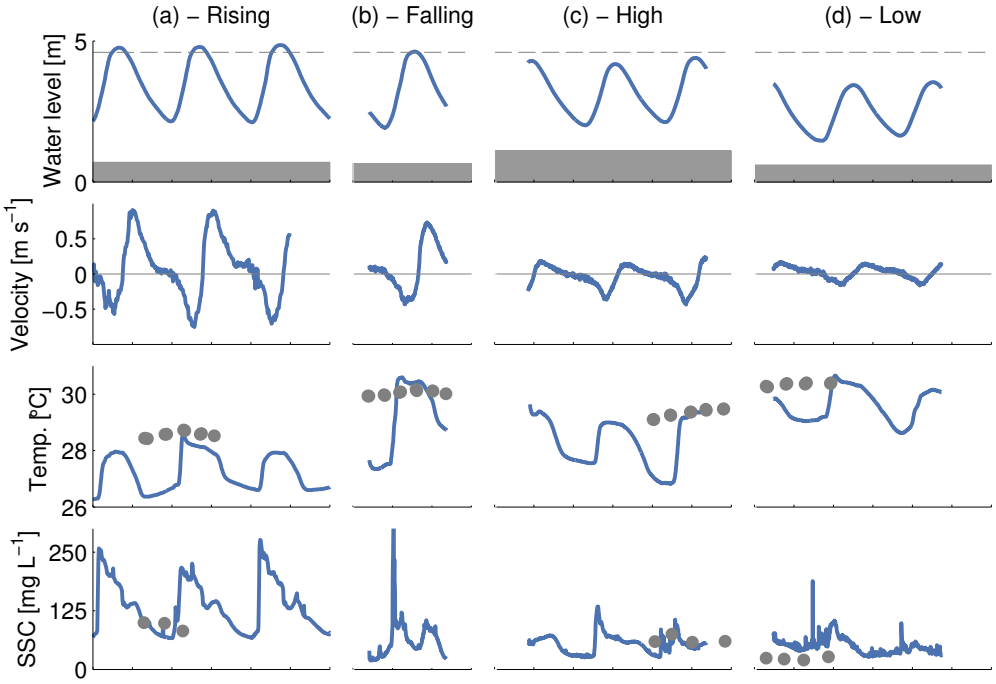

Figure 3.6: Timeseries of water level relative to Santana datum, flow velocity, temperature, and SSC for the four deployments at the Macapá channel. Dashed lines denote elevation of the tidal floodplain, grey shaded regions denote the channel bed, and dots show mainstem temperature and SSC. Water level during rising- and falling-water deployments exceeded the tidal-floodplain elevation, while those during high and low flow did not. Mainstem temperature and SSC data in (a) were collected on 26 March 2014 and have been shifted nine days to show representative values from the rising-flow period.

Floodplain not inundated during deployment

When maximum water level remained below the tidal floodplain, flow velocity was slower and SSC variability was reduced (Fig. 3.6c, d), and characteristics were more similar to those observed at tidal channels farther upstream. Maximum velocity was about 0.4 m s^{-1} on flood and 0.2 m s^{-1} on ebb, and there was no tidal pulse as observed when water level exceeded the tidal floodplain elevation. As during larger-range tides, temperature and SSC increased rapidly during the early flood and generally decreased toward high water. As velocity was slower, there was less evidence for resuspension on ebb. Temperature dynamics were similar to those during above-floodplain tides, and the early-flood SSC front accompanied the temperature front as at the other locations.

3.4 Discussion

The floodplain-incising channels of the tidal Amazon River behave in a predictable manner depending on river level, tidal range, and geographic location. Far upstream, seasonal water level is most important in determining channel dynamics, while at locations downstream, tidal range is also essential.

The tidal wave on the Amazon tidal river deforms (Kosuth et al., 2009) because of frictional effects and overtides. As a result, flood tides in the tidal channels are generally faster than ebbs, as is often the case in other shallow-water environments like tidal flats, salt marshes, and estuaries. The only observed exception to flood-tide dominance is at strongly tidal locations when the tidal floodplain is inundated. When this occurs, a tidal pulse is produced (section 3.4.1), which results in a faster ebb velocity.

Temperature generally is warmer on floods than ebbs, which results from warm mainstem water flowing into and cooling on the shaded floodplain, later discharging back into the mainstem 1–3 °C cooler. The sole exception to this behavior occurred during the rising-flow deployment at Almeirim, when the tidal-channel temperature was much warmer than the mainstem temperature on the ebb (Fig. 3.4b). Tidal-channel temperature behavior is discussed further in section 3.4.2.

Mean flood-tide SSC was 18–140% higher than ebb SSC in all deployments except

Almeirim during low seasonal discharge, when ebb SSC was 250% greater than flood. The variability of SSC with tidal range and other variables is discussed in section 3.4.3.

3.4.1 Tidal pulse

The tidal pulse occurs when water level crosses a geomorphic threshold where surface area changes more rapidly than cross-sectional area. Typically this condition is met when water level in the channel is at or near bankfull. This elevation corresponds to that of the tidal floodplain for the channels described here and the salt-marsh platform or tidal flat in other environments (French and Stoddart, 1992; Wolanski et al., 1992). On floods, water must rapidly fill the relatively flat surface area, producing a velocity transient; friction slows the spread of the flooding water onto the tidal floodplain until water level is several centimeters above the tidal floodplain. During ebbs, flow concentration into the channel produces the pulse, and it is again delayed by friction.

In the Amazon tidal river, as in other environments (e.g., Allen, 1994), the pulses are offset around the tidal-flat elevation (Fig. 3.7). Maximum velocity during flood and ebb tidal pulses occurs about 20 cm above and below the tidal floodplain, respectively. Vegetation is often cited as the source of the friction (French and Stoddart, 1992; Allen, 1994), although friction of the unvegetated bed is also sufficient to delay the pulse occurrence in tidal-flat environments (Nowacki and Ogston, 2013). In salt marshes, the effects of friction on the pulse have also been generalized into travel-time delays (Fagherazzi et al., 2008). The large amount of friction imparted by jungle vegetation at Macapá (Fig. 3.3) helps explain the relatively "wide" pulse that influences flow velocity over a broad range of water-surface elevations (Fig. 3.7).

Tidal-pulse importance to transport dynamics

Although the tidal pulse produces the highest flow velocity of the tidal cycle in Amazonian tidal channels, SSC during the tidal pulse is not great. Tidal-pulse SSC is only about 5% greater than average SSC and is just 86% of the peak SSC, which generally occurs concurrently with the temperature front (section 3.4.2). Because the pulse represents the

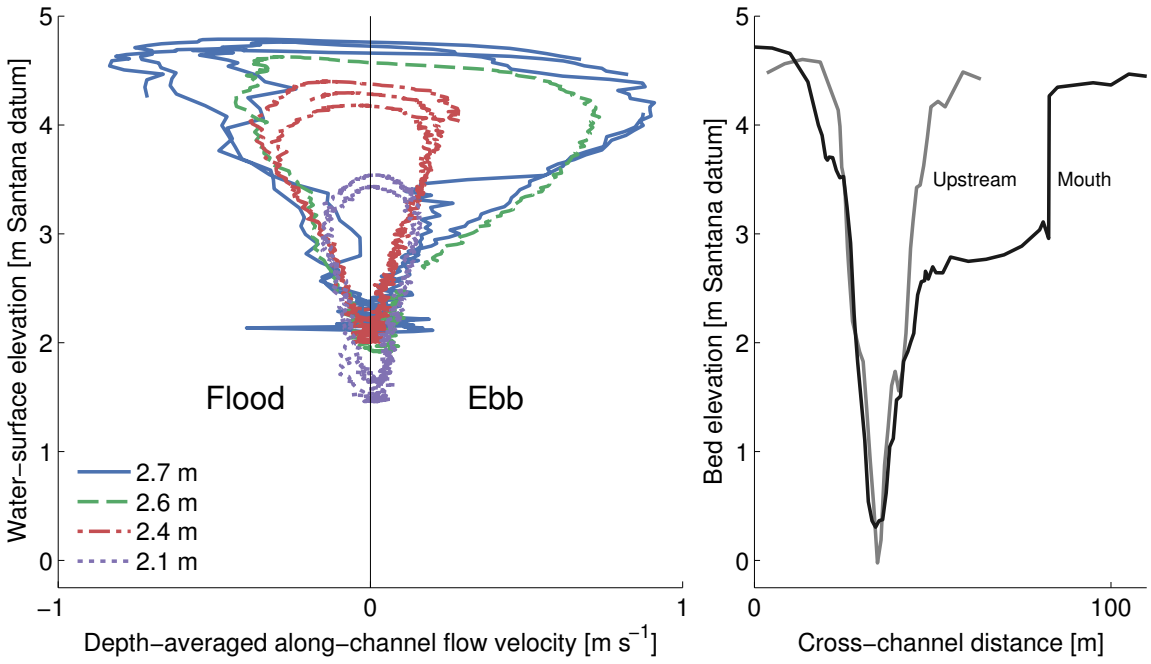

Figure 3.7: Left: depth-averaged flow velocity versus water-surface elevation for the four deployments at the Macapá channel. Legend shows tidal range. Right: Bed elevation transects (see Fig. 3.3) at the mouth of the Macapá channel and just upstream of the ADCP deployment location.

greatest water flux of the tidal cycle, the resultant sediment flux is still high despite its moderate SSC. Furthermore, sediment transport associated with the pulse is particularly important because it is this sediment (and that present at higher water levels) that flows over and ultimately may deposit on the tidal floodplain.

3.4.2 Temperature fronts

The lack of oceanic salinity in the Amazon tidal river makes temperature an important tracer that may also participate in flow dynamics. The early-flood-tide temperature front occurs along the length of the tidal river (Figs. 3.4, 3.5, 3.6) and is one example of temperature as a tracer in the Amazon. Day and night, warm mainstem water flows on flood tides into the tidal floodplain via tidal channels. A step-like temperature increase signals the arrival of mainstem water in the tidal channels, and the temperature remains elevated for the duration of the flood (e.g., Fig. 3.6). This warm water flows into the floodplain and cools under the jungle canopy and also mixes with a cooler, jungle-shaded, tidal-floodplain water mass. When the tide reverses, the water temperature near the channel mouth drops as the cooled water flows back to the mainstem.

Evidence that the temperature increase in the tidal channel is mainstem water is twofold. First, the mainstem temperature and that observed in the tidal channels after the front has passed early on flood tides is nearly equivalent (Figs. 3.5, 3.6), suggesting advected mainstem water. Second, the timing of the increase is consistent with the advective distance from the mainstem. The temperature increase occurs 40–80 minutes after the beginning of the flood tide. Integration of the flow velocity during this period for the Macapá deployments results in a distance of 60–300 m, which compares favorably to the distance between the ADCP deployment location and the mouth of the tidal channel, where it meets the mainstem. This flow-correlated temperature behavior contrasts with non-tidal riverine environments, where groundwater or hyporheic flow are often most important to temperature dynamics in floodplains and side channels (Mosley, 1989; Malard et al., 2001). Our results show that transfer of fluid between the mainstem and the tidal floodplain is an additional and substantial source of thermal variations in the Amazon tidal river.

The temperature front depends on two factors: floodplain shading and limited connectivity between the mainstem and floodplain, both of which may not be met at all locations along the tidal river. Two deployments at Almeirim exhibited behavior suggesting these factors were not met at this site. If vegetation provides little cover, the floodplain water temperature may be comparable to or even warmer than the (unshaded) mainstem. During the Almeirim low-flow deployment, solar heating of the < 1 m-deep waters of the floodplain warmed the water above the temperature of the mainstem, which resulted in elevated temperature throughout the ebb (Fig. 3.4d). The less-dense vegetation at Almeirim (Fig. 3.3) and exposed nature of the channel and floodplain enables water to warm more than at other locations with a thick jungle canopy. Increased connectivity between mainstem and floodplain has the opposite effect: it enhances mixing between the two environments and reduces their temperature differential. Because the floodplain was inundated with more than 2 m of water during the Almeirim rising-water deployment (Fig. 3.4b), connectivity between mainstem and floodplain was enhanced. The increased connectivity during this deployment resulted in a floodplain temperature that was similar to the mainstem throughout the tidal cycle (Fig. 3.4b).

Buoyancy-influenced flow

In addition to acting as a tracer of mainstem water masses to the floodplain, temperature influences flow dynamics in Amazonian tidal channels. In estuarine settings, salinity is the largest influence on density, being far more important than temperature. On the Amazon, where no salinity is present, temperature, along with SSC, sets the density.

The bulk Richardson number describes the balance between stratification, which fosters stability, and velocity shear, which fosters mixing.

$$Ri = \frac{g'h}{u^2}, \tag{3.1}$$

where $g' = (\Delta\rho/\rho)\, g$ is the reduced gravity, h is a layer thickness, and u is the flow velocity difference between the two flow layers. The Richardson number can used to estimate where and when a flow is dominated by buoyancy. In Amazonian tidal channels, temperature typically increases by 2–3 °C on flood tides (Figs. 3.4, 3.5, 3.6). Assuming the early-flood

flow is two layered, this vertical temperature difference produces a density anomaly of 0.87 kg m^{-3} for water at 30 °C. This is approximately equivalent to a salinity differential of 1.2 PSU.

The 2012 deployment at Jacaré illustrates the potential for buoyancy-influenced flows in Amazon tidal channels. During the earliest flood, the temperature at 50 cmab rose sharply about 1 h prior to the temperature increase at 10 cmab (Fig. 3.8a), indicating the presence of a thermocline at that time. As at other locations, arrival of the temperature front was simultaneous with an SSC increase at both 10 and 50 cmab (Fig. 3.8b), suggesting that warm water brings more sediment-rich water from the mainstem into the tidal channel (the SSC contribution to density is about 6% that of temperature and likely does not contribute greatly to the dynamics). Flow speeds during the early flood were very slow, less than 0.05 m s^{-1} (Fig. 3.8c), and there was a large density gradient (Fig. 3.8a) producing $Ri > 10$. The density anomaly and high Ri suggest that the temperature differential is important in establishing a buoyant plume of warm Amazon water intruding into the tidal channel at the beginning of the flood. A representative velocity profile from the early ebb (Fig. 3.8c, inset) shows shear throughout the water column, suggesting flood-tide water intruded first in the upper water column, which is a pattern consistent with a buoyant surface plume. The values also indicate that the flood tide begins as a buoyant plume of mainstem water before flow driven by the barotropic pressure gradient is established. The gravity current brings sediment from the banks of the Amazon mainstem with it, and the sediment settles out and is potentially trapped at the toe of the thermocline and advected into the tidal channel.

The predicted flow velocity of a lock-exchange gravity current is (Shin et al., 2004)

$$u = 0.5\sqrt{g'h}. \tag{3.2}$$

Here, we apply Eq. 3.2 to the assess the plume velocity of warm Amazon mainstem water flowing over cool floodplain water. Using the period of greatest temperature gradient to determine g' produces a flow velocity of 0.01–0.03 m s^{-1} for a range of reasonable flow layer thicknesses. These values compare favorably with the observed flow velocity during the earliest ebb (Fig. 3.8c), and the velocity shear in the water column at that time gives

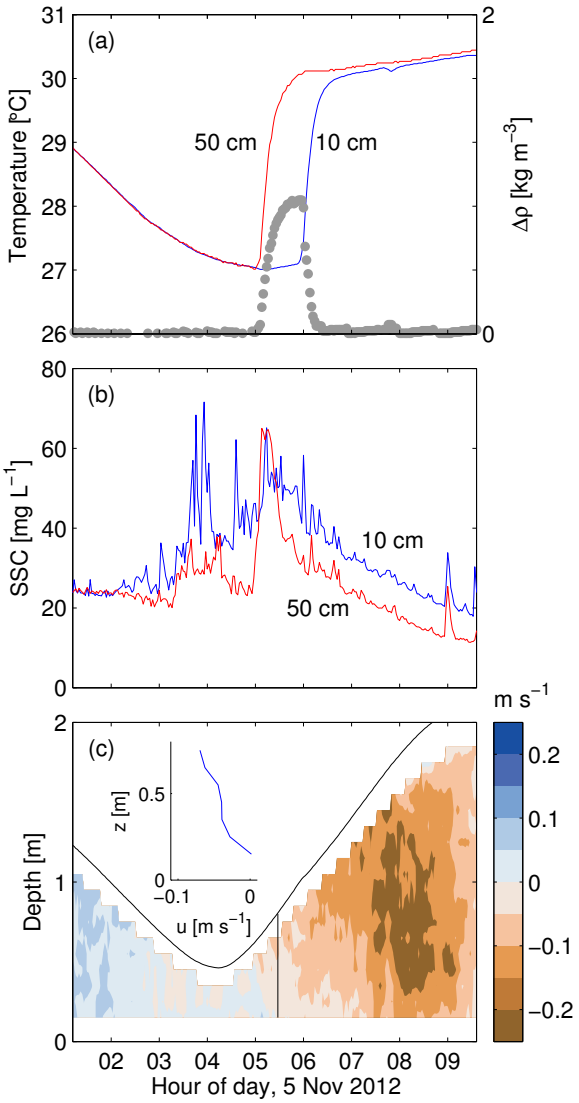

Figure 3.8: Data from the 2012 deployment at Jacaré showing (a) temperature at 10 cmab (blue) and 50 cmab (red) and $\Delta\rho$ (dots); (b) SSC at 10 cmab (blue) and 50 cmab (red); (c) along-channel flow velocity in m s^{-1}. Inset in (c) is the along-channel velocity profile at time indicated by vertical black line in velocity contour plot and shows vertical velocity shear throughout the water column.

further evidence for the existence of a temperature-driven gravity flow.

The increase in SSC began at about the same time as arrival of the temperature front (Fig. 3.9b, c), despite varying seasonal and tidal conditions. As described in the previous section, the simultaneity of the SSC and temperature fronts suggests advection, potentially via a gravity current, of higher-concentration mainstem water into the channel. At Almeirim, maximum channel SSC was similar to the SSC in the mainstem (Fig. 3.4b, c), indicating that the higher concentration water was purely advected into the tidal channel. Farther downstream, SSC in the tidal channel was greater than that of the mainstem (e.g., Fig. 3.6), though the extremely slow flow and high Ri values also suggest that local resuspension is not important in elevating the turbidity associated with the front.

3.4.3 Influence of tidal range on SSC

In addition to sediment advection, resuspension is also important in strongly tidal locations. At Macapá, both mean SSC (Fig. 3.10a) and the SSC increase associated with the thermal front (Fig. 3.10b) varied with tidal range, which suggests resuspension of sediment either within the tidal channel or at a distant location. The resuspension may occur in three potential locations: (1) within the mainstem channel; (2) in the tidal channel; and (3) on the banks of the mainstem.

We first consider the source of the additional sediment that contributes to the correlation of mean SSC with tidal range (Fig. 3.10a). Within the mainstem of the river, increased bed stresses from stronger flows associated with large tidal ranges likely resuspend more sediment than in less tidal environments, but this does not fully explain the tidal-channel observations. An additional resuspension source is necessary because tidal-channel SSC is greater than mainstem SSC in strongly tidal locations (Figs. 3.5 & 3.6). This local resuspension likely takes place in both the tidal channel and along the mainstem channel banks because of the complex relationship between flow velocity and SSC.

We second consider the correlation between the temperature-front SSC increase and tidal range (Fig. 3.10b). It is unlikely that the additional resuspension takes place within the tidal channel, because Ri is high and the increase occurs when flow velocity is less than

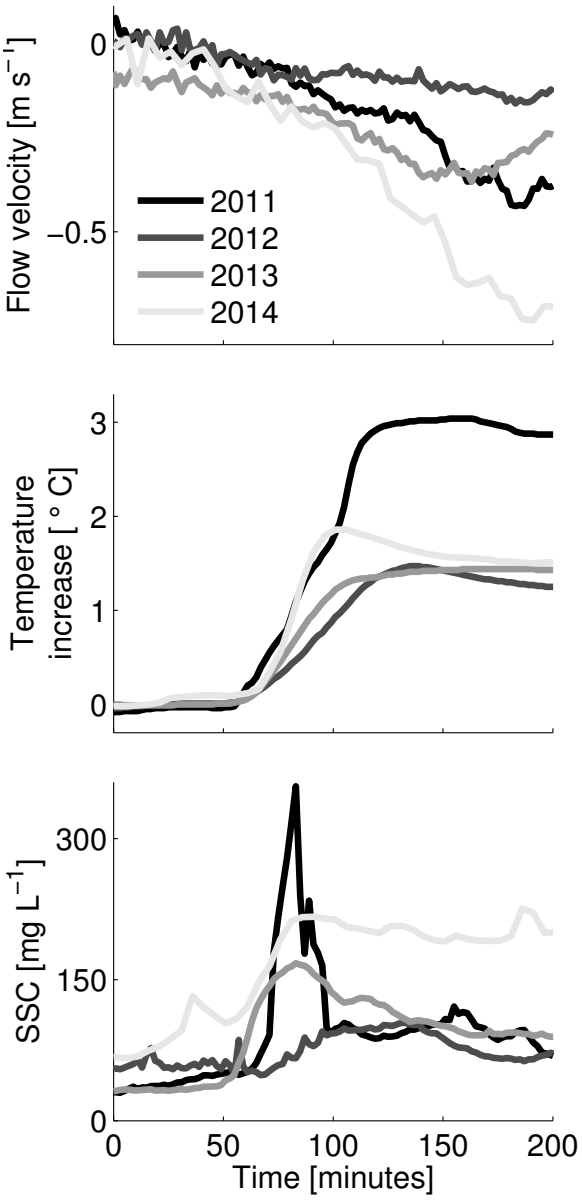

Figure 3.9: Timeseries of flow velocity (top), temperature increase (middle), and SSC (bottom) at the beginning of the flood in the Macapá channel. The temperature rapidly rose by 1.5–3 °C and was accompanied by an SSC increase.

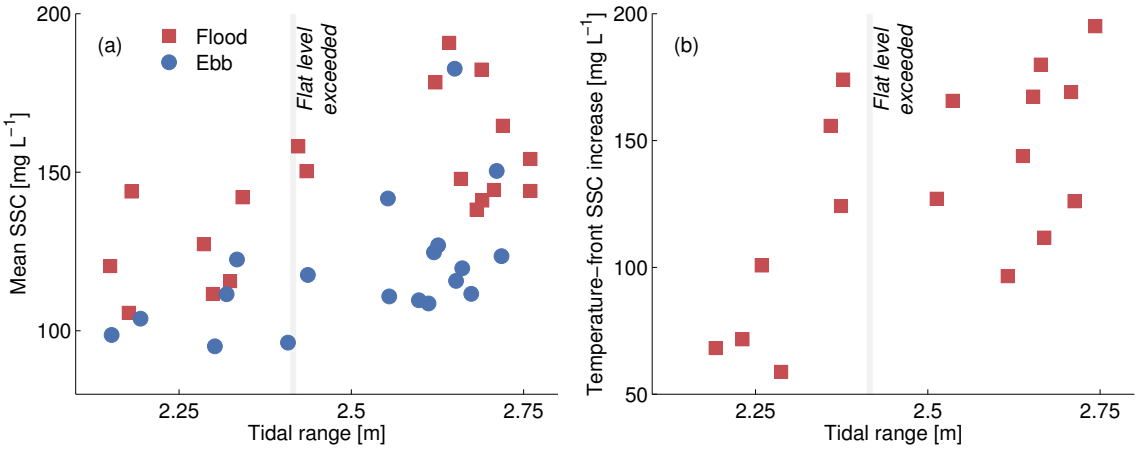

Figure 3.10: (a): tidal range versus mean SSC for each flood and ebb tide during the 2014 Macapá deployment. (b): tidal range versus the increase in SSC associated with the temperature front during the 2014 Macapá deployment.

0.15 m s^{-1} (Figs. 3.8 & 3.9), below the expected threshold for resuspension. A combination of resuspension on the mainstem banks and sediment trapping within the gravity current during the early ebb likely produces the increased sediment associated with the front.

Bed-sediment grain size of the Macapá channel has a dominant mode of 5.5Φ, which corresponds to medium silt. The time for sediment of this size to settle from suspension in a water column of 1 m depth is about 30 minutes. This settling timescale is rapid enough for sediment to deposit on the tidal floodplain during high slack water. Sediment settling out of the water column onto the floodplain is likely a primary factor in reducing the SSC of the water that flows back to the mainstem on ebb tides.

Comparison with other environments

Mean ebb SSC was less than flood SSC for tides both exceeding and not exceeding the tidal-floodplain elevation, with the exception of Almeirim at low water. This is consistent with behavior in other environments, including salt marshes (French and Stoddart, 1992) and tidal flats (Ridderinkhof et al., 2000; Friedrichs, 2011; Nowacki and Ogston, 2013). Combined with the flood-dominated flow velocity at most locations, the higher flood SSC

helps produce higher flood sediment flux, which may sequester sediment on the Amazon tidal floodplain.

In Amazonian tidal channels, there is no clear distinction in average SSC between below-flat and above-flat tides (Fig. 3.10). SSC when the water level is above the flat is generally not the highest of the tidal cycle, which is associated with with the temperature front. In salt-marsh channels, average SSC is higher during tides that exceed the level of the marsh than those that do not (French and Stoddart, 1992). This behavior is different from that of tidal flats, where the highest concentrations have been found during the velocity pulse and when depths are very shallow (Mariotti and Fagherazzi, 2011; Nowacki and Ogston, 2013). Local resuspension of sediment by wind waves can also be a major source of increased SSC in tidal flats (Ridderinkhof et al., 2000; Brand et al., 2010; Nowacki and Ogston, 2013). This is less common in salt marshes with vegetative sheltering, and presumably even less so in the forested tidal floodplains of the Amazon. While wind can reverse the flow direction and alter water level in Amazon tidal channels (Fig. 3.4a), these events tend to be short lived without sufficient time to develop sediment-resuspending waves.

3.4.4 Seasons, tides, and geography

The interaction of the seasonal and tidal water level and the tidal-floodplain morphology is a key element of the behavior of tidal-channel flow and sediment transport. Seasonal water level influences conditions at all locations along the Amazon tidal river, in part by setting the mean depth of tidal channels upon which tides vary. The magnitude of the seasonal water-level change varies depending on location along the tidal river, with large variation upstream and low variation downstream (Kosuth et al., 2009), because of the backwater effect. Propagation of the tide upstream is also affected by seasonal water level, and thus the tidal range, but the relative change in tidal range is greatest at upstream locations that also experience large seasonal water-level shifts.

For example, at Almeirim during low seasonal discharge, tides are relatively large (Fig. 3.4d), which could drive significant exchange of water and sediment with the floodplain. Connectivity with the floodplain is low, however, because of the low seasonal water level,

and the potential for significant exchange is diminished. This reflects the balance where seasonal water level must be high enough for sufficient connection to the tidal floodplain but low enough to generate meaningful tidal velocities to import or export sediment to and from the floodplain.

Seasonal distribution of water levels and the tidal pulse

Seasonal Óbidos water level is approximately evenly divided between rising- and falling-water conditions. Óbidos water level is within the upper and lower half of the seasonal water-level range—4–6 m and 10–12 m—for 61% of the year (Fig. 3.11a). The remaining half of the range, intermediate water levels (6–10 m) that represent rising and falling discharge, is present just 39% of the time. This riverine water-level influence persists to Macapá, where the low-tide water level is strongly correlated with Óbidos stage ($R^2 = 0.78$), though the seasonal river-stage range at Macapá is only about 1 m, versus 8 m at Óbidos. Tides are superimposed on this varying river baselevel, maintaining approximately the same range but shifting up and down by the seasonal river flow. As a result, the high-elevation tidal floodplain at Macapá is essentially incapable of being inundated until water level at Óbidos is greater than 8 m (Fig. 3.11c). Tidal-floodplain inundation time increases with Óbidos river stage and, by extension, season. When Óbidos water level is between 8 and 9 m, the tidal floodplain at Macapá is inundated about 2.6% of the time, while when water level at Óbidos is between 11 and 12 m, the floodplain is inundated 6% of the time and occurs during about 40% of the tidal cycles (Fig. 3.11c).

For a given Óbidos stage, the floodplain is inundated more often during rising seasonal water than falling seasonal water. This bias is potentially related to water storage on the floodplain as seasonal water level wanes, and the seasonal variability indicates that the tidal floodplain is most often inundated with water of a particular set of characteristics. The characteristics of water most often inundating the the tidal floodplain are biased toward high discharge, reflecting the total trend of Fig. 3.11c, but it is also biased toward those high water levels that are present during waning seasonal discharge. Thus deposition occurring on the tidal floodplain will preferentially bear features of high but falling seasonal water

level. SSC at Óbidos varies based on whether the seasonal discharge is rising or falling: SSC is higher during rising water than during falling water (Fig. 3.11b). Given the preferential inundation of the floodplain during high but falling seasonal water level, it is sediment from this low-SSC water that likely is best recorded in deposits on the tidal floodplain at Macapá. This SSC feedback limits rapid growth of the tidal floodplain regardless of accommodation space availability, although greater accommodation space would also change the floodplain inundation distribution.

In addition to its role in nourishing the tidal floodplain, seasonal water level influences the tidal pulse, and the pulse can only occur when water is able to access the tidal floodplain during rising, high, and falling water periods. The pulse occurs with regularity in low-elevation tidal flats (Nowacki and Ogston, 2013) and on spring tides or during storm events in higher-elevation salt marshes (Bayliss-Smith et al., 1979). On the Amazon tidal river, occurrence of the tidal pulse is controlled by both tides and seasonal water level. During intermediate river stage levels, the tidal floodplain is inundated only on spring tides; during high flow, it can access the tidal floodplain more frequently and with longer duration (Fig. 3.11c).

3.4.5 Exchange of water and sediment via tidal channels

In this section we draw some conclusions regarding exchange of water between the mainstem and tidal floodplain via tidal channels. Previous estimates of mainstem–floodplain flux on the non-tidal Amazon River have generally considered exchange via all processes, including overbank flow (e.g., Richey et al., 1989; Mertes, 1994; Alsdorf et al., 2010). Our estimate considers only exchange via floodplain-incising channels because the channels are widespread in the tidal river and they are active at nearly all river stages, in contrast to overbank flow. We divide the river into three sections centered around the Almeirim, Cajari, and Macapá tidal channels. Using average water and sediment flux values over a flood tide for each section and making conservative estimates regarding channel density and size, we extrapolate the total flux into the floodplain for each reach for a full year. The yearly water flux into (and out of) the tidal floodplain from Almeirim to the mouth is at a minimum 72

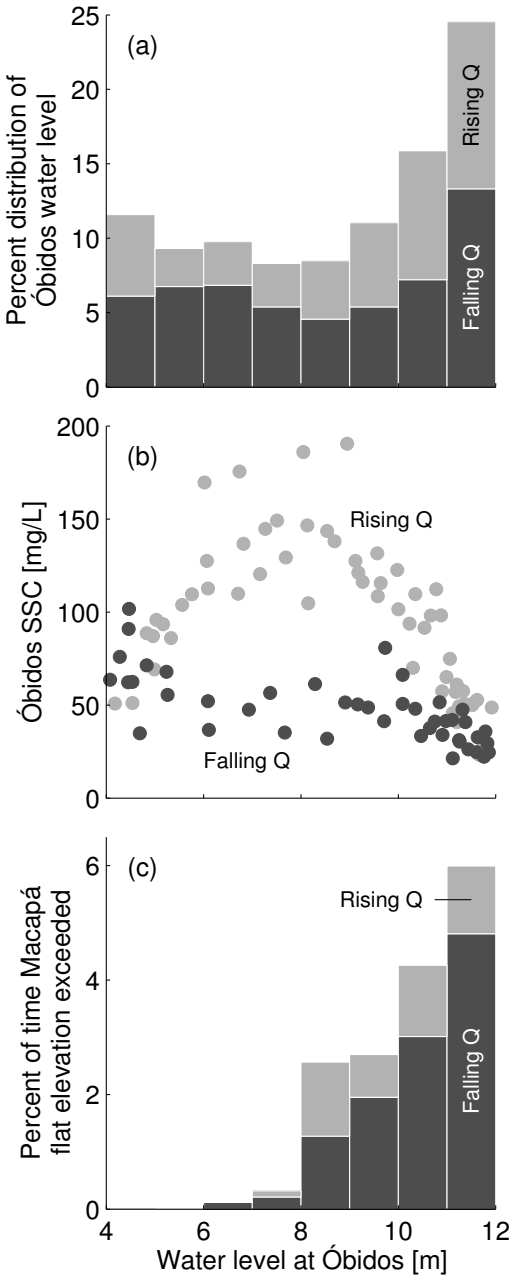

Figure 3.11: (a): Histogram of Óbidos water-level distribution. (b): Satellite-derived surface SSC at Óbidos (data courtesy ORE HYBAM). (c): Percentage of time water level exceeds the flat surface at Macapá binned by Óbidos water level. Data are grouped by rising and falling seasonal discharge as measured at Óbidos. All data are from 2011–2013.

$km^3\ y^{-1}$, which corresponds to about one percent of the yearly water discharge at Óbidos. Upstream of Óbidos, Richey et al. (1989) found extensive exchange of water between the mainstem and floodplain, with up to 30% of the mainstem flow being delivered from water stored on the floodplain. Our estimate on the tidal river is comparable to a recent study that estimated the water stored and drained from the floodplain represents only 5% of the Amazon discharge (Alsdorf et al., 2010). For sediment, at least 7 Mt y^{-1} is fluxed into and out of the tidal floodplain via channels, this value being only about 0.5% of the total Óbidos suspended load of 1200 Mt y^{-1}.

The daily unit-width sediment flux averages about 2 t d^{-1} m^{-1} in the instrumented tidal channels. Mertes (1994) computed sediment transported to the floodplain in the central Amazon basin about 700 km upstream of Óbidos, and found transport rates of 3–18 t d^{-1} m^{-1} during the seasonal flood. Our value is only slightly smaller than the values computed by Mertes (1994) and furthermore represents only flow in channels and does not account for any overbank flux in the tidal floodplain during high river discharge.

3.5 Conclusions

We have presented some of the first observations of hydrodynamics and sediment dynamics in floodplain-incising channels along the tidal Amazon River. Several themes characterize the channels across a range of tidal and seasonal water-level conditions.

- Tidal channels import water from the mainstem to the tidal floodplain with high SSC and export water from the floodplain to the river with low SSC at almost all locations and river stage. Flood-tide SSC was 18–140% higher than ebbs in 10 of the 11 deployments. This decanting process is similar to processes occurring over the seasonal flood wave (e.g., Bourgoin et al., 2007) but it takes place on an hourly timescale instead of a monthly timescale.

- The tidal pulse that occurs as flow reaches the elevation of the tidal floodplain induces the strongest velocities seen in the tidal channels and is a version of the same processes seen in tidal flats and salt marshes. In contrast to those environments, SSC during the tidal pulse was not considerably greater than at other periods in the tidal cycle.

- High-SSC water imported on floods is a result of advection from the main stem throughout the tide and also via a buoyant plume during early flood. As flow velocity increases, local resuspension may be important, especially at more tidal locations, as indicated by the increase in mean SSC with tidal range.

- In Macapá, overbank flow is an important characteristic of the flow regime, and only occurs during mid-to-high stages of the river. The water that nourishes the tidal floodplain is therefore biased toward lower seasonal SSC.

- Unit-width rates of tidal sediment transport through channels that deliver sediment from the mainstem to tidal floodplain areas are comparable to previous estimates of overbank sediment transported during the seasonal flood wave in the central Amazon River.

Chapter 4

SEDIMENT TRANSPORT OF THE LOWER MEKONG RIVER

4.1 Introduction

Rivers are the largest suppliers of sediment to the global ocean and deliver 13 Gt y^{-1} today (Syvitski and Kettner, 2011). This value is the global summation of sediment discharge measured at the lowermost river gauging stations, which are almost always upstream of tides. The ungauged regions, which include tidal rivers and their floodplains, deltas, estuaries, and nearshore zones, likely trap great amounts of sediment (Milliman and Farnsworth, 2011). In large tropical rivers, these areas may sequester about one-third of the sediment discharge (Amazon: Nittrouer et al. 1995; Mertes et al. 1996; Dunne et al. 1998; Ganges-Brahmaputra: Goodbred and Kuehl 1998; Changjiang: Milliman et al. 1985). The extensive area that these ungauged environments occupy, the considerable sediment transported in them that is not accounted for on the continental shelf, and their importance to the "true" global riverine sediment discharge to the ocean motivate investigation into their sedimentary processes.

There are many methods for predicting the character of tidal rivers and estuaries. Nearly all of these approaches base their predictions on the competition between river flow, which provides stratification, and tidal flow, which provides mixing (Dyer, 1997). Variability in river flow can come in the form of flood events, seasonal discharge changes, and long-term climatic shifts; tidal variability is primarily driven by the daily and spring–neap cycles. This paper focuses primarily on the changes induced by different seasonal discharge levels. Estuarine regime shifts driven by seasonal river discharge variability have long been observed (e.g., Hansen and Rattray, 1966) in estuaries and deltas of all sizes. The Columbia (Hughes and Rattray, 1980), San Francisco Bay (Walters et al., 1985), Tamar (Bale et al., 1985) and Merrimack (Ralston et al., 2010) estuaries transition from highly stratified to moderately stratified depending on seasonal river discharge.

The same variables that affect the estuarine regime also influence the suspended-sediment

dynamics of the tidal river and estuary. For example, seasonal shifts in sediment-transport patterns have been observed in the Chesapeake Bay (Schubel, 1968), Fraser (Milliman, 1980), Columbia (Gelfenbaum, 1983), Amazon (Allison et al., 1995), and Hudson (Woodruff et al., 2001) estuaries, and these shifts can also modify the character of the seabed. The nature of this variability determines potential sediment storage and release along the tidal river and, in turn, the magnitude and timing of sediment discharge to the coastal ocean.

One technique to explore the impacts of varying fluvial and tidal influence is flux decomposition. Decomposition of the tidally averaged (or residual) flux of salt or sediment into several terms has been applied in many tidal environments to elucidate relevant physical processes. Flux decomposition is used to describe whether the characteristics observed in an estuary result from river advection, exchange flow, tidal pumping, or some other process. While decomposition is most often applied to salt transport (e.g., Fischer, 1972, 1976; Dyer, 1974; Uncles and Jordan, 1979; Hughes and Rattray, 1980; Dronkers and van de Kreeke, 1986), the process is also used with sediment flux (Dyer, 1978; Uncles et al., 1985b,a; Su and Wang, 1986). Despite the technique's commonality, the specific approach used often differs between papers, and the number of terms retained can range from two to eight or more.

We made observations on a distributary of the lower Mekong River during high- and low-discharge periods to characterize its hydrodynamics and sediment dynamics. In addition to confirming previously observed seasonal changes of the tidal river and estuarine region of the lower Mekong (Wolanski et al., 1996, 1998), we sought to understand better the tidal-scale dynamics and spatial variability of this system and how river flow modifies these characteristics. Our objectives are to quantify the changes in the hydrodynamics and sediment transport on multiple temporal and spatial scales, decompose the residual sediment flux to determine the most important sediment-transport processes and their variability with discharge, and discuss the geomorphic implications of the observations.

4.1.1 Study region

The Mekong River ranks 7$^{\text{th}}$ worldwide in water discharge (550 km^3 y^{-1}) and 11$^{\text{th}}$ in sediment discharge (110 Mt y^{-1}) (Milliman and Farnsworth, 2011), these values being determined at locations upstream of tidal influence. The wave-influenced, tide-dominated Mekong Delta (Wright, 1985) comprises much of southern Vietnam (Fig. 4.1). Tides are mixed-semidurnal and mesotidal, with a spring tidal range of about 3.5 m near the mouth (Fig. 4.2), 2 m at Can Tho, 90 km upstream, and 1 m near the Cambodian border, 190 km from the mouth (Mekong River Commission, 2014). The river forms two main distributaries within the delta: the Bassac or Song Hau, and the Mekong or Song Tien (Fig. 4.1). These two distributaries ultimately split into eight major channels, and this study focuses on the Dinh An channel of the Song Hau distributary. The Song Hau accounts for about 41% of the total Mekong water discharge; the Dinh An carries about 70% of the Song Hau discharge and 27% of the total Mekong flow (Nguyen et al., 2008), making it the largest of the eight channels. Typical single-thread Mekong discharge upstream of the delta at Kratie, Cambodia ranges seasonally from $2,000$ m^3 s^{-1} to $40,000$ m^3 s^{-1} (Mekong River Commission, 2014) (Fig. 4.2). On the Song Hau, discharge magnitude is reduced by branching upstream, and seasonal variation is diminished by the influence of Tonle Sap, a lake that acts as a natural flow capacitor and smooths seasonal variability at locations downstream. Typical discharge ranges seasonally from $5,000$ m^3 s^{-1} to $12,000$ m^3 s^{-1} at Can Tho, Vietnam (Mekong River Commission, 2014), 35 km upstream of the landward extent our study area (Fig. 4.1). During high flow, freshwater can extend to the mouth of the Song Hau, while during low, flow salt water has been observed to penetrate about 50 km landward of the mouth (Wolanski et al., 1996, 1998).

The seasonal monsoon dominates weather in the Mekong delta. Waves during the wet summer monsoon (May–October) are southwesterly, while during the drier winter monsoon (November–March) waves are larger and from the northeast (Hu et al., 2000). Shore-parallel shelf circulation near the channel mouths is strong and to the southwest during the winter, and is weaker and to the northeast during the summer (Gagliano and McIntire, 1968). Net transport of sediment is to the southwest (Gagliano and McIntire, 1968) and has formed

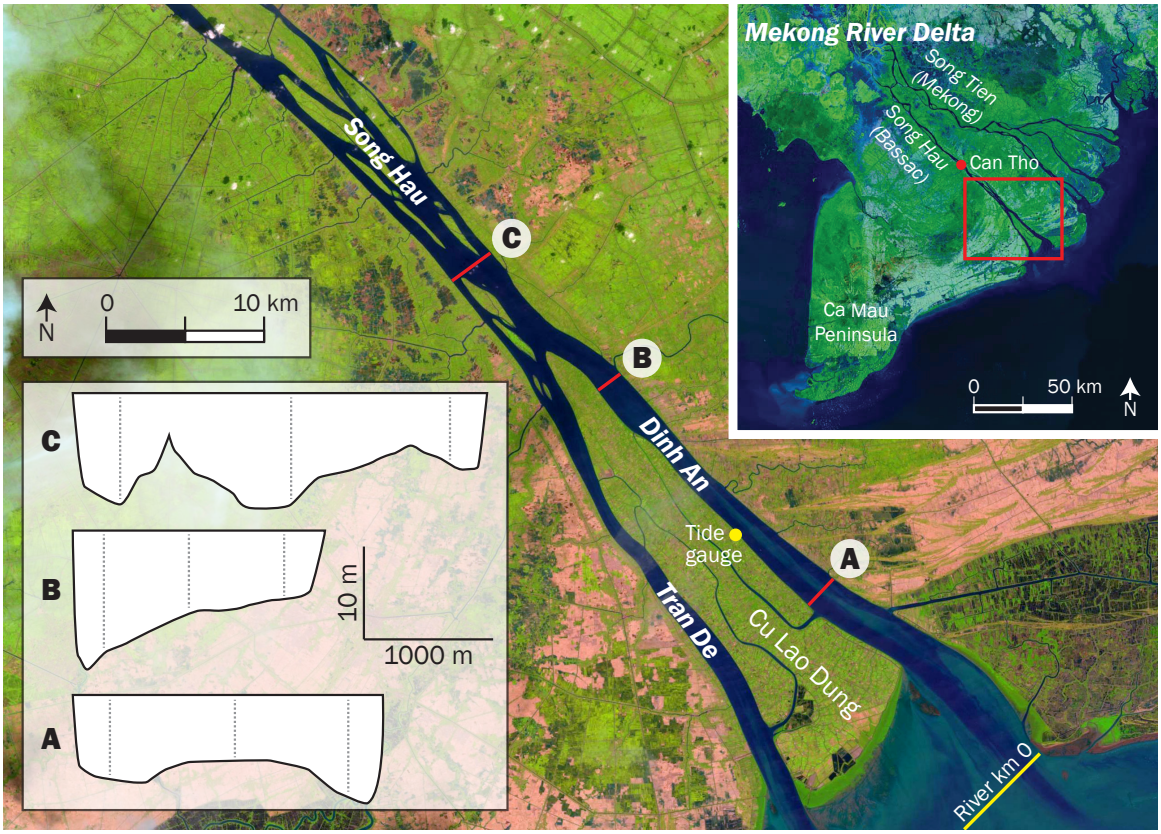

Figure 4.1: Study area basemap with Landsat 7 ETM imagery acquired 13 February 2002. Map at top right shows greater Mekong River Delta region. Red lines denote cross-sections occupied during the two cruises. Inset at lower left shows generalized bathymetry as viewed downstream, with nominal station locations indicated by dashed vertical lines. The mouth (river km 0) is defined as the cross-channel extension of the left-bank limit. This is seaward of Cu Lao Dung's subaerial extent but representative of the geomorphic transition from river to open ocean given the extensive flats fronting Cu Lao Dung.

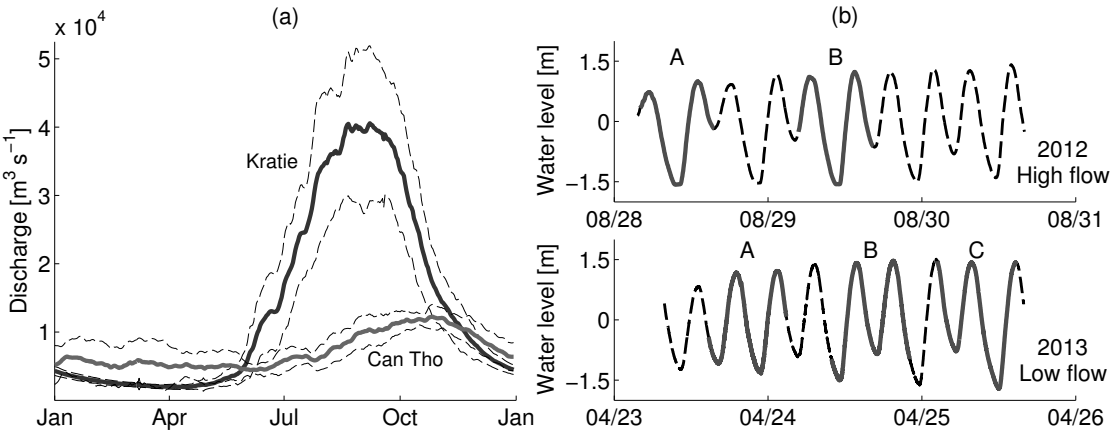

Figure 4.2: (a) Average historical discharge, ± one standard deviation, at Kratie, Cambodia, based on 45 years of record (1925–1969), and at Can Tho, Vietnam, based on seven years of record (2001–2007). Data provided by the Mekong River Commission. (b) Measured water level during the 2012 high-flow (top) and 2013 low-flow (bottom) cruises with measurement periods for the cross-sections indicated. The location of the tide gauge is indicated on Fig. 4.1.

the Ca Mau peninsula and a shelf clinoform (Ta et al., 2005; Xue et al., 2010). Despite sometimes energetic shelf conditions, waves within the distributary channels were minimal during our field campaign.

Little previous work has been published on the hydrodynamics and sediment dynamics of the tidal Mekong River. During a high-flow period in 1993, Wolanski et al. (1996) encountered salt-wedge estuarine conditions where ebb flows were stronger than floods, the river bed was mostly sandy, no along-channel SSC gradient was observed, and no turbidity maximum was present. Deposition and erosion dominated SSC variability and the system exported sediment to the ocean. During low flow in 1996, Wolanski et al. (1998) found a partially mixed Mekong with stronger peak flood flows than ebb flows . Suspended sediment, potentially deposited offshore during previous high-flow periods, was transported landward from coastal waters.

4.2 Methods

4.2.1 Data collection

Boat-based surveys of flow velocity, salinity, suspended-sediment concentration, and riverbed sediment were made during high and low seasonal discharge in August and September 2012 and April 2013, respectively. A 600 kHz RD Instruments acoustic Doppler current profiler (ADCP) measured flow velocity. An RBR, Ltd. XRX-620 CTD with integrated optical backscatter sensor (Campbell Scientific OBS-3+), both sampling at 6 Hz, measured profiles of salinity, temperature, depth, and suspended-sediment concentration (SSC). Bed sediment was collected with a grab sampler.

Our field efforts captured the seasonal and spatial variability of the Song Hau and its distributary channels. Observations were made at three cross-sections (Fig. 4.1), two of which—sections A and B, in the Dinh An channel—were re-occupied during both campaigns. Section C, upstream of the bifurcation around the island of Cu Lao Dung, was occupied only during low flow. Bathymetry is complex and varies between sections (Fig. 4.1). Section A consists of two deep channels separated by a mid-channel shoal. Section B has a deep thalweg close to the left bank and the bathymetry gradually shoals toward the right bank. Section C is made up of three channels separated by shoals that are extensions of islands immediately upstream and downstream of the cross-section. The left and center channels are directly connected to Dinh An, while the right channel is more directly connected to Tran De.

At each section, the ADCP operated continuously for about 24.8 hours. The vessel repeatedly traversed each cross-section and completed a one-way pass in 15–30 minutes, depending on channel width, vessel traffic, and logistical considerations. Stops were made at three pre-determined station locations (Fig. 4.1) on alternate crossings to conduct CTD casts and collect water samples. Bed-sediment sediment samples were collected at each section throughout the tidal cycle.

4.2.2 Data processing

The data were quality checked and spurious data points were removed. No-data areas from instrument blanking near the water surface and river bed were extrapolated by prescribing a no-slip condition at the bottom and applying a shape-preserving cubic spline to the empty regions. CTD data extended closer to the surface and bed than the ADCP data, but any gaps were filled by linear extrapolation. Representative ADCP data were assigned to each CTD cast by averaging 200 m of ADCP data centered around each CTD station. Throughout this paper, velocities and fluxes are presented in a channel-wise coordinate system using the fluvial convention of looking downstream: positive along-channel values indicate downstream flow, and positive across-channel values indicate flow toward the right bank.

Bed-sediment samples were wet sieved into fine (< 63 μm; silt and clay) and coarse (> 63 μm; sand) fractions. Grain size of the disaggregated fine fraction was determined with a Micromeritics SediGraph III particle-size analyzer.

4.2.3 Sigma coordinates and decomposition

To help interpret seasonal and spatial variability, we averaged the velocity and sediment fluxes over the 24.8 hour tidal cycles and also decomposed the subtidal sediment fluxes. In this process we replaced normal depth values with a fixed number of sigma levels that vary between 0 at the water surface and 1 at the bed. Sigma coordinates are particularly useful in shallow settings with large tidal ranges (Giddings et al., 2013) like the Mekong. Cross-sections were divided into a fixed quantity of grid cells of area dA by applying sigma coordinates across the width of each section. The magnitude of dA varies as the cross-sectional area changes with the tide, but the number of elements remains constant.

The tidally averaged but spatially varying flux field is

$$\langle u\,(y,\sigma,t)\;c\,(y,\sigma,t)\rangle\,, \tag{4.1}$$

where u is velocity, c is concentration (e.g., of salt or sediment), and angle brackets denote a tidally averaged quantity. Both u and c vary across-channel (y), vertically (σ), and in time (t). When considering the residual velocity alone, c is set to 1 everywhere.

The sub-tidal or residual flux through a cross-section is

$$F = \left\langle \int uc\, dA \right\rangle, \tag{4.2}$$

which is the section-integrated form of Eq. 4.1. When considering salinity, F will be zero for an estuary in steady state, though steady state is rarely achieved (Uncles et al., 1985b). F is generally nonzero for sediment, suggesting import or export, because sediment can have local sources and sinks via resuspension and settling, and generally does not escape upriver to its terrestrial source as salt can do with its ocean source. For $c = 1$, F is water discharge.

We decomposed the flux following the method described by Lerczak et al. (2006). This routine opts for simplicity by grouping into only three terms: a sectionally and tidally averaged term, a sectionally varying and tidally averaged term, and a remainder term, which is sectionally and tidally varying:

$$\begin{aligned} F = \left\langle \int uc\, dA \right\rangle &= u_0 c_0 A_0 + \int u_1 c_1\, dA_0 + \left\langle \int u_2 c_2\, dA \right\rangle \\ &= F_R + F_E(\sigma) + F_T(y, \sigma). \end{aligned} \tag{4.3}$$

In the equation above, $u_0 = \left\langle \int u\, dA \right\rangle / A_0$, $c_0 = \left\langle \int c\, dA \right\rangle / A_0$, $A_0 = \left\langle \int dA \right\rangle$, $u_1 = \langle udA \rangle / dA_0 - u_0$, $c_1 = \langle cdA \rangle / dA_0 - c_0$, $u_2 = u - u_0 - u_1$, and $c_2 = c - c_0 - c_1$. Full details of the derivation can be found in Lerczak et al. (2006) and MacCready and Banas (2011). This mathematical procedure makes no assumptions about estuary or tidal-river properties. Accordingly, the terms must be interpreted with care. The first term, F_R, is attributed to advection of material from upstream that is flushed seaward by the river, potentially to a location outside the mouth, and includes Stokes drift. The second term, F_E, is the flux associated with particle movement via estuarine exchange-flow flux. Tidally averaged velocity and salinity fields can be inspected to see whether this term in fact results from gravitational circulation. The remainder is F_T, often called the "tidal term," which arises from temporal correlations of velocity and the constituent. F_T contains all leftover processes, including tidal pumping and, in the case of sediment, local erosion and deposition.

4.3 Results

The 25-hour transects conducted at the three cross-sections show that the Dinh An channel was an ebb-dominant tidal river with an ephemeral salt wedge during high flow and a flood-dominant, partially mixed estuary during low flow. Table 4.1 gives an overview of the conditions during the two cruises. Spring and near-spring tides were present during both cruises, with a maximum tidal range that exceeded 3 m (Fig. 4.2). During the high-flow cruise, diurnal tidal inequality was greatest during measurement at section A, while greater and lesser tides were more comparable at B. Tidal range increased during the low-flow campaign, with the largest tides present during measurement at section C.

Table 4.1: Velocity dominance, estuarine regime, tidal range in m, salinity range in PSU, top-to-bottom stratification range (ΔS) in PSU, 95% range of depth-averaged SSC in mg L^{-1}, and bed grain-size characteristics during high and low flow at sections A, B, and C.

	High flow		**Low flow**		
	A	B	A	B	C
Velocity	Ebb dominant	Ebb dominant	Flood dominant	Flood dominant	Flood dominant
Estuarine regime	Salt wedge/ tidal river	Tidal river	Partially mixed	Partially mixed	Partially mixed
Tidal range	1.2–2.5	1.8–2.7	2.2–2.4	2.2–2.9	2.2–3.1
Salinity	0–18	0	7–24	2–11	0–6
ΔS	0.0–18.0	0.0	0.3–13.1	0.1–6.2	0.0–2.8
SSC	61–242	71–171	27–305	33–459	30–577
Grain size	Variable	Variable	Fine	Fine	Variable

4.3.1 High flow

Section A

The ephemeral salt wedge at section A was an important modifier of the section's velocity, salinity, and SSC patterns. The salt wedge was present during late floods and into early ebbs, and salinity in the section was zero otherwise (Fig. 4.3a). Salinity within the salt wedge reached 18 PSU on the lesser flood, when it was more than 6 m thick, and 7 PSU on the greater flood, when it was weaker and thinner, its intrusion limited by the previous strong ebb. The salt wedge was thickest and longest lived in the deep right channel. When the salt wedge was present, there was strong vertical velocity shear on floods, with seaward flow in the freshwater above the wedge and landward flow within the wedge. SSC within the salt wedge was low, less than 30 mg L^{-1}, except for during the strongest upstream salt-wedge flow, when SSC was elevated.

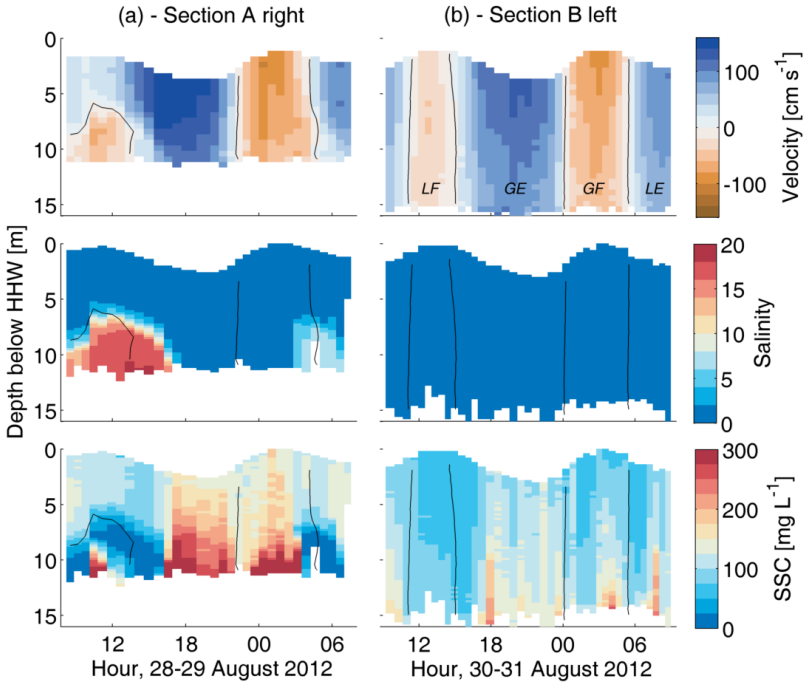

Figure 4.3: Along-channel flow velocity, salinity, and SSC during high flow in the thalwegs of (a) section A, and (b) section B. Data from the other stations at each cross-section are not shown here but are used later in the paper. Contour lines indicate velocity zero crossing.

Outside of the salt wedge—above it when it was present and throughout the water column when it was not—flows were strong, and exceeded 1 m s^{-1}. Ebbs were elongated and faster relative to floods, and the fastest currents were in the right channel. Background SSC was about 100–200 mg L^{-1}, but reached 400 mg L^{-1} near the bed during the strongest flows. SSC was correlated with velocity, and concentrations were higher on ebbs.

Section B

In contrast to section A, no salinity was present during measurement at section B (Fig. 4.3b). Floods were strongest in the thalweg (left station), and ebbs, which were stronger than floods, were greatest in the middle of the channel. As at section A outside the salt wedge, flow direction was uniform throughout the water column, and there was minimal velocity shear. Depth-averaged SSC ranged from 130–200 mg L^{-1} and was higher on ebb, similar to the observations at section A. Average SSC at section B was about 30% less than the freshwater regions of section A, though it remained positively correlated with velocity, particularly at the center and right stations, where concentrations were greatest.

4.3.2 Low flow

Section A

Floods at section A during low flow began first in the lower water column, particularly in the left and right channels. During maximum flood, velocity was upstream everywhere and strongest in the channels (Fig. 4.4a). Salinity ranged from 8 to 18 PSU and was partially mixed during the floods. Salinity was greatest in the right channel, which is where the salt wedge was strongest during high flow. SSC was vertically stratified and was lesser at the center and right stations than the left station, where values approached 700 mg L^{-1} near the bed.

Floods transitioned to ebbs simultaneously throughout the water column, and flow was uniformly downstream everywhere, though slowest near the bed in the right channel. Salinity ranged from 8 to 20 PSU, and, as during floods, the greatest values were near the right-channel bed. Stratification was greater on ebbs than floods and ranged from 5 to 10

PSU. As during floods, SSC was lowest in the right channel and the highest in the left channel, and exceeded 700 mg L^{-1} near the bed during the strongest flows.

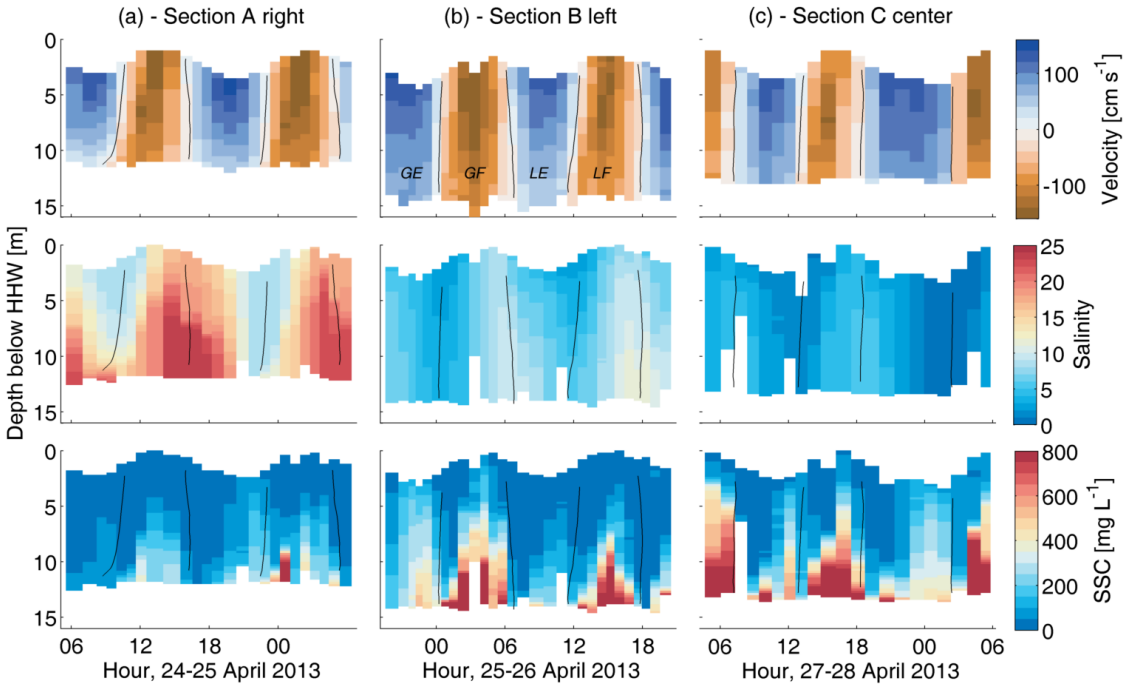

Figure 4.4: Along-channel flow velocity, salinity, and SSC during low flow in the thalwegs of (a) section A, (b) section B, and (c) section C. Data from the other stations at each cross-section are not shown here but are used later in the paper. Contour lines indicate velocity zero crossing.

Section B

At section B, floods were most dynamic in the thalweg. Flow velocity was strongest, salinity greatest (4–8 PSU), and SSC largest (> 1000 mg L^{-1}) in the thalweg on maximum flood (Fig. 4.4b). This behavior is consistent with the deeper regions of A, where these quantities were also greatest on floods. A strong correlation between nearbed velocity and SSC was present, especially in the thalweg, and SSC at B was in general greater than at section A.

On ebbs, flow and SSC were greater over the shoal and lesser in the thalweg. Flow velocity was nearly 1 m s^{-1} and SSC exceeded 1000 mg L^{-1} near the bed at the right

station but remained less than 300 mg L^{-1} in the thalweg. As during floods, salinity was greatest in the thalweg, and ranged from 4 to 9 PSU.

Section C

At section C, dynamics in the left and center channels were similar but distinct from those in the right channel. On floods, flow was stronger in the left and center channels (1–1.2 m s^{-1}) (Fig. 4.4c) and weaker in the right channel (0.7–0.8 m s^{-1}). Salinity was greatest at the left station (3–5 PSU) and least at the right station, averaging about 1.5 PSU. SSC was greatest in the left and center stations, correlated with nearbed flow velocity, and vertically stratified. Average SSC was also greater than observed at sections A and B. In the left and center channels, the 1000 mg L^{-1} isolute was about 2 m above the bed and maximum concentrations were about $2,500$ mg L^{-1}; SSC in the right channel reached only about 400 mg L^{-1}.

On ebbs, maximum velocity was focused in the thalwegs of the three channels. Salinity ranged from 1 to 2 PSU at all three stations, though it was generally less at the right station than the left and center stations. SSC was generally less than 200 mg L^{-1}, but was correlated with velocity, especially in the right channel, where ebb SSC was greatest.

4.3.3 Bed sediment

The bed-sediment distributions were distinct between the two cruises. During high flow, grain-size distributions at A and B were coarse, averaging 25–75% sand (Fig. 4.5), and had considerable variability. Mud balls, pebble-like clasts of consolidated mud that are erosive in nature (Bell, 1940), were prevalent at the left and center stations of B. Shallow areas—the center station at section A and right station at section B—were finer, with sand fractions less than 12% by weight.

During low flow, bed sediment at A and B was finer, with a sand fraction of about 15% at each station. Within-section variability was minimal, in contrast to the spatial heterogeneity during high flow. At section C, grain size at the left and center stations, which are more directly connected to the Dinh An channel than the right station, was coarse and somewhat

variable, and was similar to the deep stations of section A and B during high flow. The right station, which is more directly connected to the Tran De channel, was considerably finer, even more so than at A and B during low flow, with only about 5% sand.

4.4 Discussion

The lower Mekong River transitions from freshwater tidal river to estuary, which varies between salt-wedge and partially mixed conditions depending on seasonal river flow. Here we interpret this seasonal regime change, compute patterns of residual velocity and sediment flux, review factors that control these patterns, generate a new yearly sediment discharge, and provide insights on the geomorphic response of the system.

4.4.1 Seasonal regime change

Freshwater discharge

During high flow, instantaneous water discharge reached a maximum of more than $20,000$ m^3 s^{-1} on ebb and about $18,000$ m^3 s^{-1} on flood (Fig. 4.6). After integrating the instantaneous discharge over the 24.8 hour tidal cycle, the resultant freshwater river discharge was approximately $7,300$ m^3 s^{-1}. Assuming that the Dinh An channel represents about 70% of Song Hau discharge (Nguyen et al., 2008), total Song Hau discharge was about $10,000$ m^3 s^{-1} during the high-flow cruise. While modern discharge records are limited, this scaled discharge compares favorably to the 2001–2007 average Song Hau high-flow discharge measured at Can Tho (Fig. 4.2).

During low flow, maximum discharge at sections A and B was about $25,000$ m^3 s^{-1} on flood and about $20,000$ m^3 s^{-1} on ebb. Mean discharge was only about 500 m^3 s^{-1} at A and B during the low-flow cruise, a factor of 50 smaller than the maximum instantaneous discharge values. At section C, both flood and ebb discharge magnitudes were greater than at A and B, exceeding $30,000$ m^3 s^{-1} and $22,000$ m^3 s^{-1}, respectively. At C, the freshwater discharge was about $1,700$ m^3 s^{-1}, a result of section C's location upstream of Cu Lao Dung, spanning the width of the Song Hau before it branches into the Dinh An and Tran De channels (Fig. 4.1). This estimate suggests that discharge during the low-flow cruise was

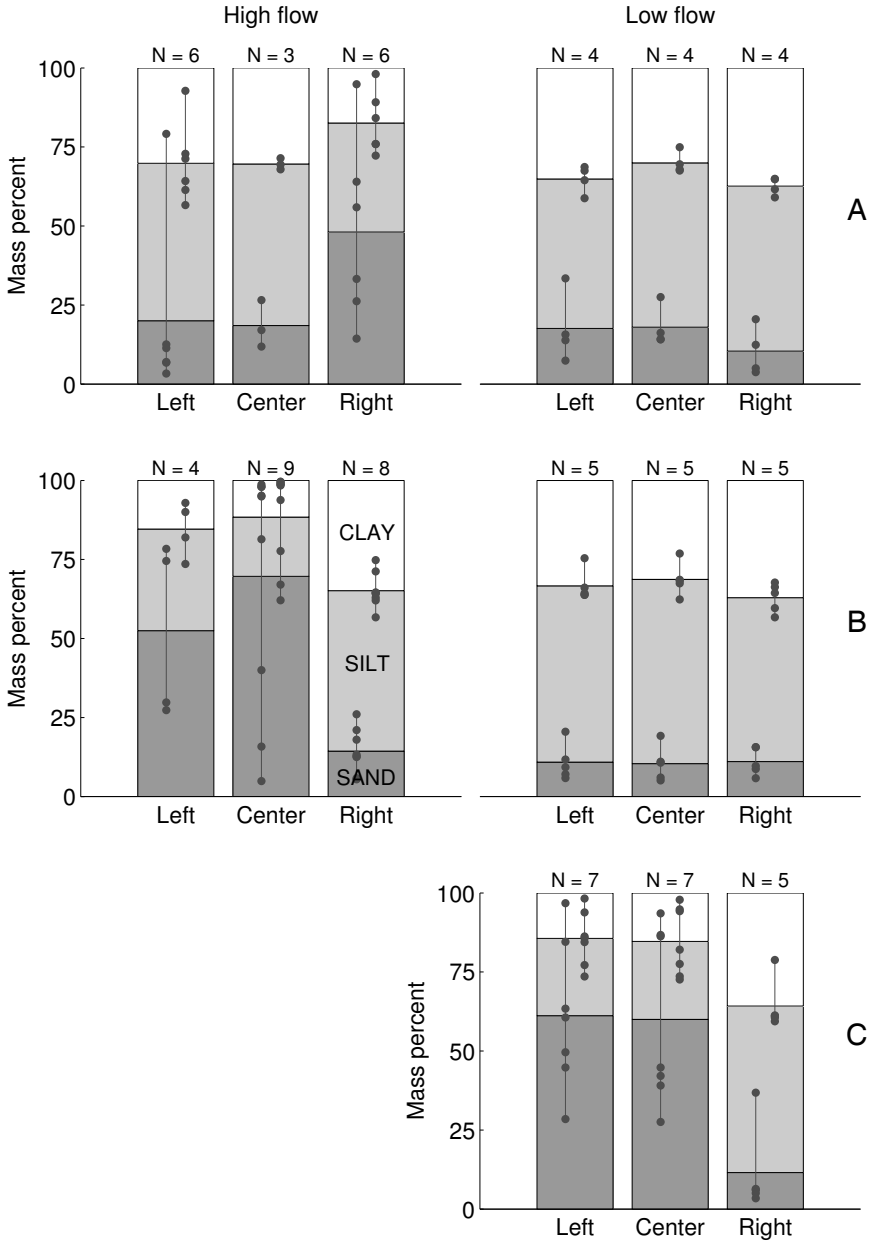

Figure 4.5: Mean sand, silt, and clay bed-sediment mass distributions at A, B, and C during high and low flow. Values for each sample are plotted as dots connected by vertical lines; numbers of samples analyzed are listed at the top of each distribution.

about one standard deviation below the historic low-flow discharge measured at Can Tho (Fig. 4.2).

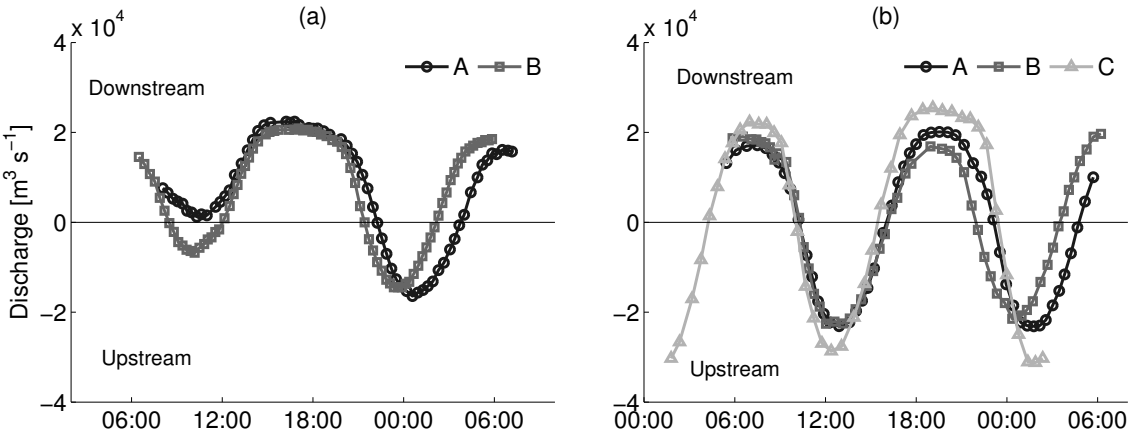

Figure 4.6: Instantaneous water discharge at sections A, B, and C during (a) high flow and (b) low flow. The data have been time shifted and overlaid to allow for easier comparison.

Velocity patterns

The dominant tidal-flow direction is a function of the freshwater that must be carried downstream by the river discharge, and the magnitude of ebb dominance increases as river flow grows relative to the flow induced by filling and draining the tidal prism (Savenije, 2005). Unless the river floods its banks, ebbs will be stronger and of increased duration during high river discharge to accommodate the additional freshwater input. During high flow of the Mekong, river discharge was so great that the areal majority of section A continued flowing seaward during the lesser ebb (Fig. 4.3a), and these extended ebbs helped flush sediment downstream. During low flow at A and B, when the river discharge was small compared to the tidal prism, flood-dominated shallow-water tidal behavior prevailed. The flow-velocity patterns at C are a hybrid of the high- and low-flow conditions at A and B; section C's greater freshwater discharge produces high-flow characteristics like extended ebb duration while still being flood dominated (Fig. 4.6). Flow in the right channel of C was less flood dominated than in the left and center channels, suggesting that flood tides were

preferentially routed via the Dinh An channel and ebbs via Tran De.

Salinity intrusion

Integration of the flow velocity reveals that the salt wedge intruded 11 km upstream of section A on the high-flow greater flood. This location, some 30 km upstream of the mouth (river km 0; Fig. 4.1) and 8 km downstream of B, is farther landward than the location of maximum salinity intrusion found by Wolanski et al. (1996). That study took place in November, when Song Hau discharge is on average about 10% higher than during our study period, suggesting that, despite extensive dam construction in the interim (Xue et al., 2011), the high-flow salinity intrusion length has not changed dramatically in the past 20 years. This stability may be related in part to Tonle Sap's moderating influence on flow downstream. During the greater ebb, salinity was pushed to within 3 km of the mouth, again based on integration of the velocity field at section A.

Maximum salinity intrusion during the low-flow cruise was 22 km upstream of section C, and 55 km upstream of the mouth, about half way to Can Tho. This value is similar to previous estimates of salinity intrusion during low-flow of 45–60 km (Wolanski et al., 1998; Nguyen and Tanaka, 2007). On ebbs, salinity was pushed about 1 km downstream of section C at the left and center stations and about 3 km downstream at the right station. The lower salinity intrusion in the right channel is explained by its decreased flood dominance and resultant lower salinity values.

Suspended-sediment resuspension and advection

During high flow, SSC in freshwater regions—section A outside the salt wedge and everywhere at section B—was correlated with velocity on both floods and ebbs (Fig. 4.7), with higher values on ebb, owing to the stronger ebb velocities. The salt wedge at A shielded the river bed from high bed stresses, and SSC in the salt wedge was substantially lower than in the freshwater regions, except during periods of strongest upstream flow within the salt wedge (Fig. 4.3a), when local resuspension occurred. Saline water from offshore entering the river channel was generally devoid of sediment, any suspended load it once carried having

settled out by the time it reached section A. This is congruent with the weaker southwesterly waves and lower winds at the coast during the summer monsoon (Hu et al., 2000), though the shallowness (< 5 m) of the subaqueous delta topset (Unverricht et al., 2013) suggests that even moderate waves could resuspend sediment there.

Minimum background SSC was also greater during high flow than low flow in the freshwater regions (Fig. 4.7). The elevated minimum SSC during high flow suggests that sediment settling rates were slow in freshwater regions, likely because flocculation was limited by the negligible salinity. Wolanski et al. (1996) posited that advection could be disregarded and variability in the sediment signal during high flow was fully attributable to local erosion and deposition. While our data similarly show the (minor) SSC variability is primarily due to local erosion and deposition, the majority of the fine-grained sediment transported during high flow is carried by the river from locations upstream.

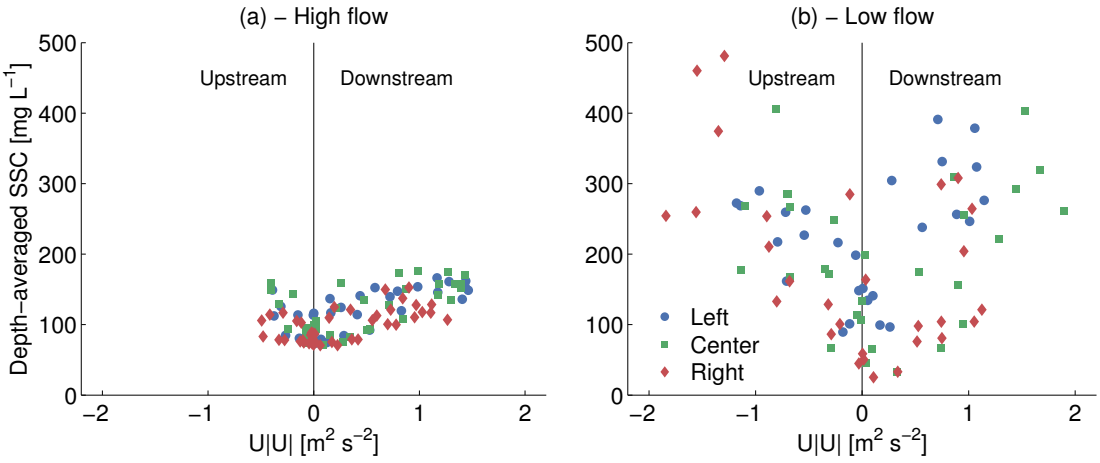

Figure 4.7: Squared depth-averaged flow velocity plotted against depth-averaged SSC at section B during (a) high flow and (b) low flow.

SSC during low flow was more dynamic: minima were lesser and maxima were greater than during high flow (Table 4.1). This was potentially because of flocculation enhanced by the presence of salinity throughout the tidal cycle at A and B. More fine-grained sediment was available on the river bed to be resuspended (Fig. 4.5), and the strong vertical variation in SSC (e.g., Fig. 4.4b) shows that this sediment was not fully mixed throughout

the water column. The SSC stratification, in conjunction with the relatively strong velocity shear, suggests preferred sediment pathways within the water column wherein sediment is brought landward lower in the water column and seaward in the upper water column. Depth-averaged concentrations tended to be higher on the flood (Fig. 4.7b) which, when combined with the flood-dominant flow velocity, fostered landward sediment pumping. The low background SSC, large resuspension signal, and flood dominance suggest that sediment delivery from upstream was minor compared to local processes.

Estuarine turbidity maximum The rapid increase in high-flow SSC near the toe of the salt wedge at section A around 17:00 on 28 August (Fig. 4.3a) is classic behavior for an estuarine turbidity maximum (ETM) (e.g., Meade, 1969; Geyer, 1993). The increase may, however, simply be due to local resuspension of sediment that had been shielded during the flood by the salt wedge (Wellershaus, 1981). Indeed, SSC throughout the water column remained elevated during the (unstratified) ebb, and the decrease in SSC around 04:00 on 29 August was abrupt and dramatic when the salt wedge was again present. This behavior runs contrary to the idea of ETMs as mobile regions of elevated SSC, wherein an ETM-derived turbidity increase would be ephemerally present at a particular location (Dyer, 1986). Another sediment-trapping mechanism of salt wedges is the decrease in upper-layer SSC as sediment sinks into the lower layer, thereby trapping it (Geyer, 1993). The first part of this behavior was observed at section A when the salt wedge was present (Fig. 4.3a), but SSC within the salt wedge rarely exceeded 30 mg L^{-1}, suggesting that minimal sediment sunk from the upper layer into the salt wedge.

During the partially mixed low-flow cruise, the general increase in SSC with distance upstream (Table 4.1) and co-location of the salinity node and enhanced SSC could point to an ETM region at or near section C. ETMs often form at or near the head of salinity intrusion (Dyer, 1995), and section C during low flow captured the freshwater-saltwater interface. This interpretation could be biased because the tidal range increased during our measurement campaign (Fig. 4.2). Despite the larger tidal range and presumably because of its distance from the mouth, velocities at C were not greater than at A or B, but more sediment may have been resuspended farther downstream and subsequently pumped upstream. The fine-

grained bed sediment at A and B suggests significant sediment trapping in those locations, another feautre of ETMs, and the coarser grain size at C indicates that it is upstream of the strongest ETM effects.

4.4.2 Residual flow and sediment flux

High flow

During high flow at sections A and B, the residual velocity was downstream everywhere (Fig. 4.8), resulting from the significant freshwater input to the system. The minimum in residual velocity near the bottom of the deeper right channel at A was due to upstream flow in the ephemerally present salt wedge (Fig. 4.3a).

In a purely fluvial system, the maximum residual velocity would be in the thalweg. In this tidal-river reach, however, the lowest residual velocity at B was in the thalweg within 500 m of the left bank, and the maximum was in the middle of the cross-section. This minimum is likely related to salt-wedge effects from locations downstream propagating upstream to B (section 4.4.1), even though salinity at B never exceeded 0.1 PSU. The morphology of the cross-section at and seaward of B, combined with the presence of salinity in deep locations downstream, helps explain why flood flows at B are stronger in the deep regions and ebbs are stronger over the shallows. Given their similarity, flows in the deep thalweg on the left-hand side of B are likely most directly connected to those in the right-hand channel of A.

Residual sediment flux during high flow echoed the residual velocity at both A and B (Fig. 4.8). At section A, the seaward residual sediment flux (Eq. 4.1) (Fig. 4.9) is expected because of the downstream velocity field (Fig. 4.8) and low SSC variability (Fig. 4.7). The residual velocity drove the strongest residual fluxes in the mid-water column of the deep regions to the left and right of the mid-channel shoal, and toward the right side of the mid-channel shoal (Fig. 4.8). The smallest residual sediment flux, close to the bed in the right channel, was a result of the intermittently present salt wedge there, which was slow moving and generally devoid of sediment (Fig. 4.3a).

At B, sediment discharge was similarly downstream everywhere. The greatest down-

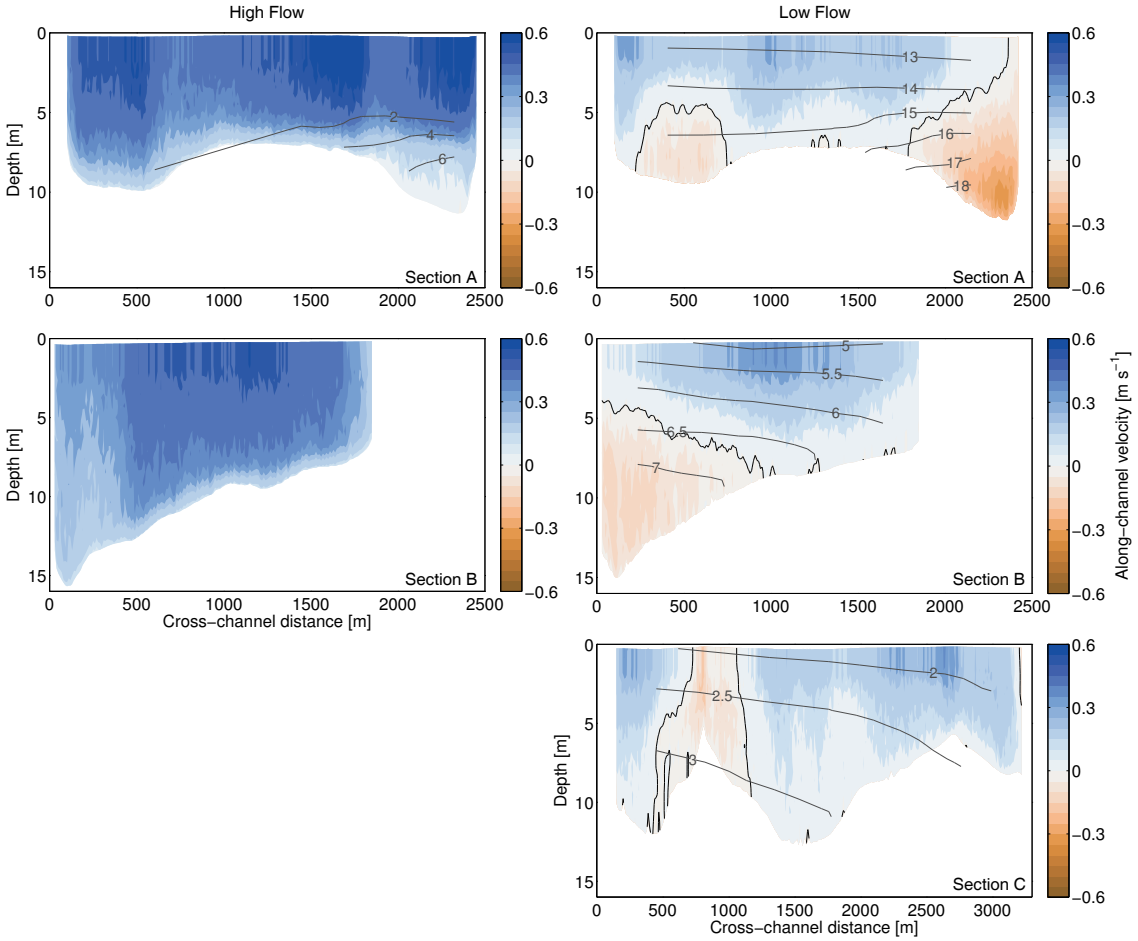

Figure 4.8: Residual along-channel flow velocity at sections A, B, and C during high flow (left) and low flow (right). Black contour lines indicate velocity zero crossing. Grey, labeled contour lines indicate extrapolated and tidally averaged salinity in PSU. Note change in x-axis scale of section C.

stream flux per unit area was over the shoal, and the flux in the thalweg was weaker. The reduced sediment flux in the thalweg is consistent with the lower SSC and reduced residual velocity (Fig. 4.8) there.

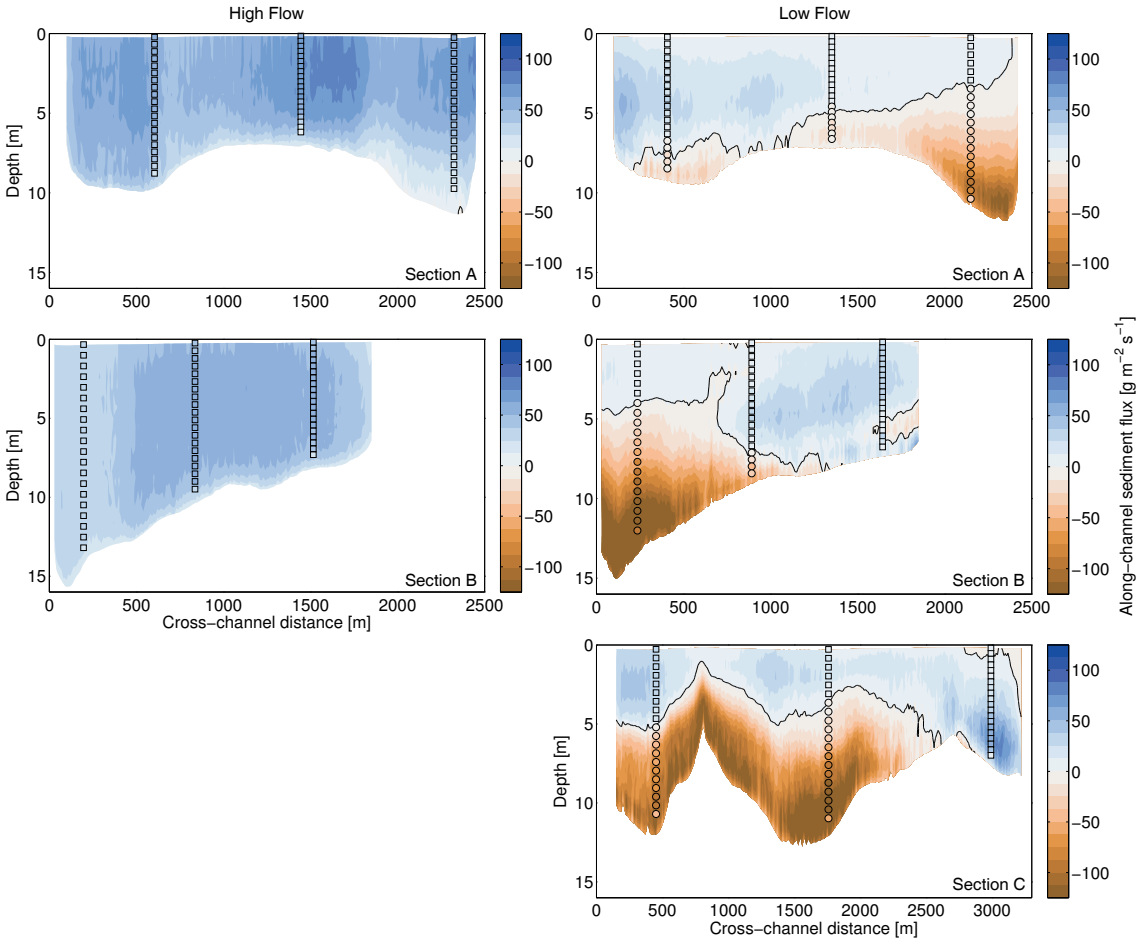

Figure 4.9: Residual along-channel sediment flux at sections A, B, and C during high flow (left) and low flow (right). SSC measured at the three stations was extrapolated across the channel and multiplied by the measured velocity to produce these maps. Results from the three stations at each section are presented using circles and squares, with squares denoting seaward flow. Contour lines indicate flux zero crossing. Note change in x-axis scale of section C.

Low flow

During low flow, the zones of residual upstream flow in the deep areas of A and B (Fig. 4.8) were due to gravitational circulation, compensated by downstream flow in shallower regions. Residual flow at C was downstream across the majority of the cross-section, a result of the greater fluvial discharge upstream of Cu Lao Dung. An exception was the region of landward residual flow just upstream of section C (Figs. 4.1 & 4.8) which results from a recirculation zone in the lee of the island.

The low-flow residual sediment-flux patterns were distinct from the residual velocity, in contrast to the high-flow observations, as can be expected from the SSC and velocity variability within the water column during low flow. At section A, there was considerably more spatial variability in sediment flux than during high flow (Fig. 4.9). Across the width of the channel, residual sediment flux was generally landward in the lower portion of the water column and seaward in the upper portion of the water column, in contrast to the residual velocity (Fig. 4.8). At both the left channel and the mid-channel shoal, the lower 10–25% of the water column imported sediment, while the upper 75–90% exported sediment. In the right channel, there was considerably greater landward sediment flux, and only the upper 25% of the water column exported sediment. The increased landward flux in the right channel is a result of the strong landward residual velocity here (Fig. 4.8), primarily attributable to the estuarine circulation. The reduced landward flux in the left channel is due to the lower SSC there and weaker gravitational circulation.

At section B, baroclinic effects were essential to the residual sediment flux, and the flux was similar to the residual velocity (Fig. 4.8). In the thalweg, the majority of the water column brought sediment landward, with only the upper 25% exporting sediment seaward. The shallower regions exported sediment throughout the water column.

Section C had a complex residual flux field, owing to its geographic location immediately upstream and downstream of two mid-channel islands (Fig. 4.1). In the left and center channels, the lower half of the water column was given over to strong upstream sediment flux, similar to the deep sections of A and B. The upper portion of the water column exported sediment toward the ocean. The vertical shear in the residual flux is likely due to

tidal pumping and not the estuarine circulation, as the residual velocity at these locations is downstream (Fig. 4.8). In contrast, the right channel transported sediment downstream throughout the water column. This pattern, taken in context with the geographic location of section C, suggests that during low flow the Dinh An channel (on the left side of C) primarily imports sediment upstream along Cu Lao Dung. Sediment is brought landward via estuarine circulation in the deep regions, as seen at A, B, and the left and center channels of C. The Tran De channel, on the right side of C, serves primarily to export sediment from the Song Hau distributary. This suggests that mutually evasive flow and sediment flux patterns (Harris, 1988) develop around Cu Lao Dung during low flow. Such mutually evasive flow patterns have been observed in other large deltas of the world, including the Ganges-Brahmaputra (Barua, 1990) and Fly (Harris et al., 2004), and modify the release of sediment to the marine environment.

The complexity of the sediment-flux field during low flow is consistent with observations in other strongly tidal systems. In the tide-dominated Fly River delta, for instance, some channels were net importers while others were net exporters of bedload sediment, implying that suspended-sediment transport patterns were similarly complex (Harris et al., 2004). Cross-sectional variability in tidally averaged sediment flux has also been modeled in the Hudson estuary (Ralston et al., 2012). There, average fluxes in deep regions were up-estuary, while fluxes over shoals were down-estuary, and the net flux was considerably smaller than would have been measured in the channels or shoals alone. Taken together, these studies reinforce the importance of spatially characterizing the sediment and flow field of an entire cross-section, and demonstrate the caution that must be taken when extrapolating flux measured at a single location.

4.4.3 Factors controlling sediment discharge

Applying Eq. 4.3 enables us to decompose the residual sediment flux into terms that represent physically meaningful processes. This procedure allows us to better interpret the factors driving the transition from tidal river and salt-wedge conditions to partially mixed estuary.

We expect the integrated residual sediment flux (Eq. 4.2) during high flow to be seaward at both A and B given their residual velocity and sediment-flux patterns (Figs. 4.8 & 4.9). Indeed, total integrated flux here was downstream at a rate of about 1 t s^{-1} (Fig. 4.10). River advection as characterized by F_R (Eq. 4.3) dominated the residual flux by composing over 80% of the total. The bulk of the remainder was contained in the downstream-oriented tidal term, F_T, suggesting that local resuspension was present and helped transport sediment downstream, but that it was less important than advection from upriver. There was minor upstream exchange flux F_E at section A, likely resulting from the episodically present salt wedge; this flux was small because SSC was generally low in the salt wedge and mixing was limited by the sharp pycnocline. Decomposed quantities at B were similar, though F_E was negligible because salinity there was always less than 0.1.

During low flow, the Dinh An channel imported less than 0.1 t s^{-1} of sediment at A, about a tenth of the 1 t s^{-1} exported during high flow (Fig. 4.10). The exchange-flow term drove the net upstream flux, far outweighing the small river term, although the the downstream-oriented tidal term counteracted some of the exchange-flow term. This is somewhat unusual; in the case of salt flux the tidal term is generally oriented upstream (MacCready and Banas, 2011) because shallow-water tidal processes (e.g., flood velocity dominance) tend to pump material landward. Sediment is not a conservative tracer like salt, however, and other processes like resuspension and settling fluxes contribute to this term.

At section B, about 0.3 t s^{-1} of sediment was imported, a moderate increase from the residual flux calculated at section A. The small downstream river term was compensated by upstream flux from the exchange and tidal terms. The increase in sediment import at B could be a result of the larger tidal range during that survey day compared to the range during measurement at A (Fig. 4.2).

The net upstream sediment flux was about 0.7 t s^{-1} at section C. The downstream river component of flux of about 0.3 t s^{-1} was considerably larger than observed at A and B, and was due to the greater freshwater discharge at section C, on the Song Hau, compared to the Dinh An discharge at A and B (section 4.4.1). Exchange-flow flux was of the same order as that observed at B, and represented about 30 percent of the total upstream flux.

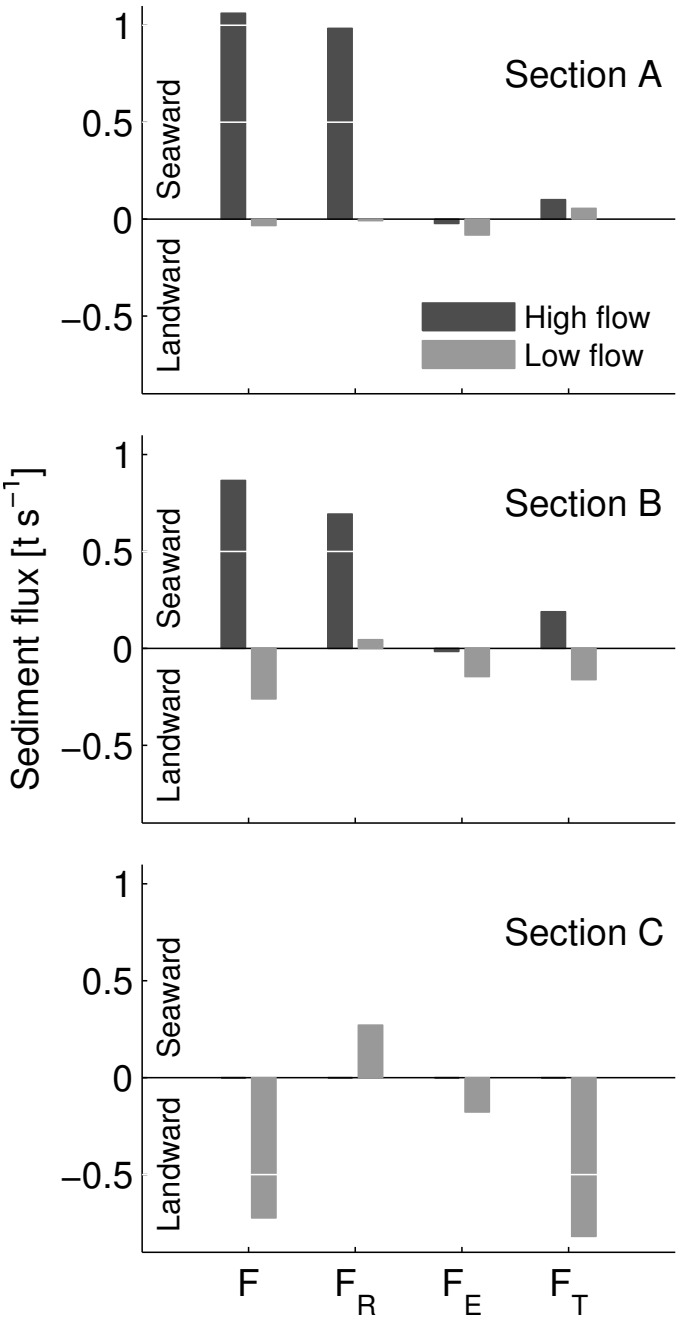

Figure 4.10: Decomposed residual sediment fluxes at sections A, B, and C during the two cruises. Section C was measured only during low flow. F: total flux; F_R: river flux; F_E: exchange-flow flux; F_T: tidal flux.

The driver of the increased upstream flux at C was the large tidal term, which more than balanced the river term and increased the total sediment import rate.

Synthesis of factors

During high flow, river advection was the most important component of the net downstream sediment flux. A large F_R is expected given the significant freshwater input, and the minimal influence of F_E is similarly intuitive because of the lack of salinity. Tidal fluxes, including local resuspension and settling, were large compared to the low-flow period but insignificant compared to the high-flow total, which is again consistent with the reduced local resuspension during high flow. During low flow, exchange flow and tidal fluxes were most important, especially in the Dinh An channel. The residual low-flow velocity and salinity (Fig. 4.8) are consistent with a strong F_E driven by gravitational circulation: upstream flow deep in the water column and downstream flow in the upper water column. The strong resuspension during low flow (Fig. 4.7) and minimal river discharge both enable a large F_T. On the mainstem Song Hau at section C, the river component was larger than at A and B because of the greater river flow in that section, but the exchange flow and tidal terms still drove the net sediment import.

The residual flow and sediment-flux vectors and inferred sediment-transport pathways during high and low flow are shown graphically in Fig. 4.11. Our results illustrate the complexities of transport dynamics in the transition between tidal river and estuary and have similarities with previous work on the Mekong and other large river systems. Conditions on the Mekong shelf are congruent with our findings of sediment export during high flow and import during low flow. River-derived SSC was observed 50–60 km offshore during the summer monsoon, while, during the winter monsoon, concentrations were low and the sediment was assumed to have settled within the river mouths (Anikiyev et al., 1986). On the Fraser River, Canada, Milliman (1980) observed that the majority of the sediment discharge occurred during the high-flow freshet. During low flow, there was little or no seaward transport of sediment, and near-bottom sediment transport was landward. Similarly, river discharge controls sediment transport to the ocean in the Changjiang River estuary, China

(Milliman et al., 1985).

Seasonal or longer-timescale variability in sediment discharge has been documented in other deltas with large freshwater reaches dominated by tidal processes. For instance, on the Fly River delta, Papua New Guinea, estuarine processes reach past the channels during non-El Niño conditions and ETM-related sediment can escape to regions outside the mouth area. During El Niño, which corresponds to decreased river discharge, the ETM is trapped landward of the mouth, even during spring tides, which restricts seaward delivery of sediment (Ogston et al., 2008).

Though we captured large-amplitude tides during our study (Fig. 4.2), they represent a limited subset of the spring–neap progression. Spring–neap tidal variability should not be overlooked (e.g., Allen et al., 1980), particularly during low flow, when the relative influence of tides is large compared to river discharge.

Extrapolated sediment discharge

The residual sediment flux of about 1 t s^{-1} during high flow represents a theoretical yearly sediment discharge of 32 Mt y^{-1} from the Dinh An channel, if high-flow conditions were present year-round. During low flow, average Dinh An sediment import was 0.3 t s^{-1}, corresponding to about 9 Mt y^{-1} if low-flow conditions prevailed at all times. Assuming high and low flow conditions each represent half of the year (Fig. 4.2), yearly Dinh An suspended-sediment discharge is about 11 Mt y^{-1}. Applying the flow partitioning values of Nguyen et al. (2008) to this value results in 15 Mt y^{-1} exported from the Song Hau distributary, and about 40 Mt y^{-1} from the Mekong River as a whole. In order to interpret this new estimate, we look to previous values from other studies, though they are based on scarce data often collected far from the mouth. Early estimates of 170–190 Mt y^{-1} were made in the 1960s at stations 1000 km or more upstream of the mouth 1963 (Economic Commission for Asia and the Far East, 1966; Holeman, 1968). A discharge of 178 Mt y^{-1} was estimated 850 km from the mouth, with a notation that perhaps only 100–150 Mt y^{-1} are delivered to the ocean (Härden and Sundborg, 1992), implying deposition of 26–44% in downstream floodplain and delta. One recent and generally accepted estimate is 110 Mt y^{-1}

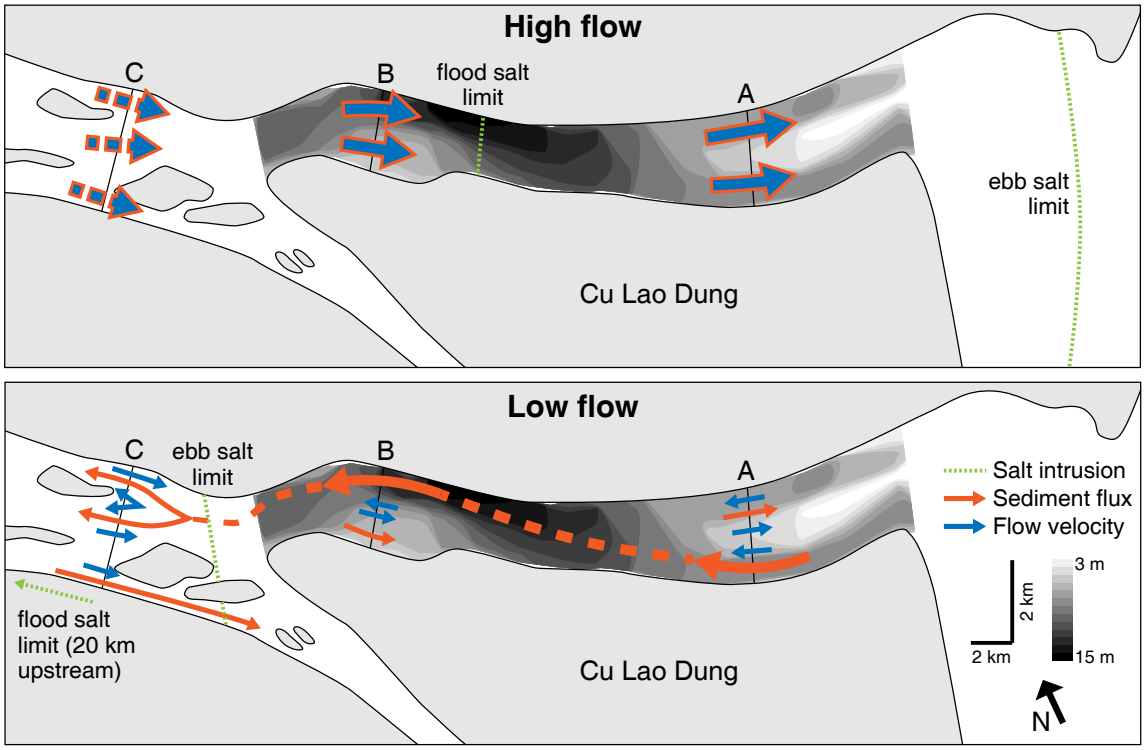

Figure 4.11: Schematic of residual sediment-transport (blue arrows) and flow-velocity (orange arrows) pathways during high and low flow. Thickness of arrows qualitatively indicates flux magnitude. Dashed lines indicate inferred pathways. Salt intrusion extent is calculated by integration of the velocity field and represents the seaward-most locations of water with salinity less than 0.5 PSU. To better show pathways, the scale of this schematic has been distorted. Generalized bathymetric contours are shown for the Dinh An channel.

today and 150 Mt y^{-1} before damming and other impoundment (Milliman and Farnsworth, 2011), but this estimate again is based on a synthesis of gauged values far from the mouth and does not account for deposition in the tidal reach.

Our sediment discharge value is 64–76% smaller than estimates made upstream, and 60% smaller than one previous estimate at the mouth. This suggests either significant deposition on the floodplain and delta or a dramatically changing Mekong sediment-discharge rate. It could also indicate a distribution of sediment discharge among the distributary channels that is different from water discharge, or one that varies with seasonal river flow.

What conditions would be necessary to obtain sediment discharge at the mouth similar to the modern estimate of 110 Mt y^{-1}? A scenario wherein the Dinh An channel operates as a high-flow system throughout the year is required: in this situation, Dinh An sediment discharge would be about 32 Mt y^{-1}, and, using the same scaling as above, total Mekong sediment discharge would be 117 Mt y^{-1}. This value is comparable to modern estimates and yet is still considerably smaller than higher and oft-cited values of 170 Mt y^{-1} or more.

Although our computed sediment discharge is seasonally limited, it was obtained closer to the mouth than any other sediment discharge estimate of the Mekong, and those of most other large, tidally influenced rivers worldwide. Our value, about 65% less than the estimate upstream of tides and about 60% less than one estimate at the mouth (Härden and Sundborg, 1992), suggests that significant amounts of sediment may be stored within the tidal-river reach, which is consistent with the notion of tidal rivers as sediment traps. At a minimum, these new insights illustrate the dynamic variability of the tidal Mekong and its changing sedimentary role with seasonal discharge levels.

4.4.4 Geomorphic response

The bed-sediment characteristics reflect the pattern of suspended-sediment export during high flow and import during low flow. The coarser grain-size distributions in deep regions of the distributary channels during high flow are consistent with a system that mobilizes and transports fine particles to locations downstream, as observed in the residual flux, especially F_R (Fig. 4.10). Shallower locations during high flow, especially at section B, were finer (Fig.

4.5) and had higher SSC than the deep thalweg, suggesting spatially heterogeneous local sediment resuspension. The finer bed sediment during low flow is representative of a system that imports (via landward-directed F_R and F_T) and seasonally stores fine-grained sediment that is remobilized during subsequent high-flow periods.

The migration of the coarse region from within the Dinh An channel during high flow to above Cu Lao Dung during low flow suggests a shift in the location of fine-sediment trapping processes. During high flow, bed stresses are high enough that mud cannot deposit in the deep regions, where the presence of mud balls suggests flow scouring of the river bed. The mud cap imported during low flow evidently extends only as far as the upper limit of Cu Lao Dung. The coarser material at the left and center stations of section C during low flow suggests that this area is above the region of the greatest sediment trapping, which includes sections A and B in the Dinh An channel. The finer material at the right station of C, which is a direct upstream extension of the Tran De channel, is intriguing. While the right station, and by inference Tran De, is more ebb dominated, anecdotal evidence suggests Tran De is becoming a less important conduit for flow and sediment flux, and may be a preferential location of sediment deposition. This might explain why more fine bed sediment is present at the right station of section C, despite its lower salinity and reduced flood dominance.

Shoal and channel-island formation and maintenance

While bedload dynamics are essential to fluvial (Osterkamp, 1998) and tidal (Dalrymple et al., 2003; Harris et al., 2004) landform generation and maintenance, our observations suggest suspended-sediment pathways also support the development and maintenance of the rapidly prograding islands in the Mekong. Section C is surrounded up- and downstream by two channel islands, which divide the distributary into three channel sections (Fig. 4.1). Residual flow is downstream across most of the section, except for a region of upstream flow near the upstream island (Fig. 4.8). The residual upstream flow and sediment flux (Fig. 4.9) may help produce the island's average progradation rate of 45 m y^{-1}, which is estimated from Landsat imagery acquired between 1990 and 2010. While our data at section C are from only the low-flow period, they do provide a glimpse into what is potentially an island-

building flow regime, where sediment import via estuarine circulation and tidal pumping nourishes the downstream ends of channel islands. During high flow, flushing from the system by the river may erode some of this sediment, though annual progradation persists.

Farther downstream, at section A, the mid-channel bar resembles the linear subaqueous ridges that often form in river mouths of tide-dominated systems (Wright, 1977). These ridges are thought to be generated by lateral convergence of sediment from ebb- and flood-dominated channels. Indeed, during low flow, the right channel is more flood dominated with respect to velocity (Figs. 4.4a & 4.8) than the left channel, and sediment is generally imported in the right channel and exported via the left channel (Figs. 4.9a & 4.11). This pattern of sediment transport around the shoal may be related to the shoal's maintenance and, ultimately, its emergence as another channel island (Hori et al., 2002).

4.5 Conclusions

We have presented water-column and bed-sediment time-series observations made along 30 km of the tidal Mekong River. These measurements include water level, flow velocity, salinity, SSC, and bed-sediment grain size, and expand the present understanding of the dynamics of large tropical deltas under varying seasonal discharge. Our conclusions are as follows:

- The flow and sediment dynamics of the tidal Mekong River undergo a comprehensive regime change between high and low seasonal discharge. This is highlighted by a transition from a tidal freshwater system with an ephemeral salt wedge to a partially mixed estuarine system.

- During high flow, Dinh An residual sediment discharge was seaward at a rate of about 1 t s^{-1}, and during low flow it was spatially variable and landward at a rate of 0.3 t s^{-1}. These rates scale to a yearly sediment discharge to the South China Sea of 11 Mt y^{-1} for the Dinh An channel and 40 Mt y^{-1} for the entire Mekong River. This value is about 65% less than most previous estimates of Mekong sediment discharge.

- Decomposition of the sediment flux reveals that the river component was most impor-

tant during high flow, while baroclinic and tidal processes, especially local resuspension, were more important during low flow.

- Residual sediment flux was seaward throughout the water column during high flow. During low flow, residual sediment flux was landward in deep regions and seaward in the upper water column. These pathways provide evidence for larger-scale mutually evasive flow (sediment import via Dinh An and export via Tran De) around Cu Lao Dung during low flow.

- Seasonal flow dynamics are reflected in seabed grain-size characteristics, wherein grain size is variable to coarse during high flow and finer during low flow. The residual flow and sediment-flux patterns also support the maintenance and progradation of mid-channel islands.

Chapter 5

SUMMARY

This dissertation illuminates the importance of various sedimentary processes occurring in the two distinct but related environments, tidal flats and tidal rivers. Observations of hydrodynamics and sediment transport in the muddy tidal flats of Willapa Bay, Washington, USA; the tidal Amazon River, Brazil; and the lower Mekong River, Vietnam are used to investigate sediment fluxes and trapping mechanisms in each environment. These results are discussed in the greater context of a range of tidal and riverine environments across the globe.

The processes that transport water and sediment in tidal-flat channels are explored in Chapter 2, which quantifies fluxes of water and sediment during three focused deployments over 10 months in Willapa Bay. Interaction between water-level variations and the morphology of the channel/flat complex produces well-defined velocity pulses during both flooding and ebbing tides. SSC trends are also largely set by the same morphologic control. Pulse-related transport processes represent about 27% of the water budget and 35% of the suspended-sediment flux budget of the observed secondary channel while making up only 8% of the deployment time. Wind increases minimum SSC via wind-generated waves and currents and is a significant short-term control on SSC. Wind alters the flow regime in channels and flats, and augments flood dominance of channels through increased over-flat ebb flow and smaller ebb pulses. During windy periods, ebb-pulse intensity decreased and flood-pulse intensity increased. Along-channel water and sediment transport were flood dominant at all the measurement locations. Residual upstream water transport was 1.9–2.7 times greater, and sediment flux was 2.7–3.8 times greater, during storms than during calm periods. These observations provide insight to sediment-transport processes active on tidal flats worldwide and reveal important similarities with processes in tidal floodplain channels associated with larger rivers, as discussed in Chapter 3.

Although tidal flats may not be directly river influenced, the dynamics of tidal channels that incise the floodplains of large tidal rivers are intimately connected to the river mainstem. Chapter 3 presents some of the first observations of hydrodynamics and sediment dynamics in floodplain-incising channels along the tidal Amazon River, Brazil. Tidal channels import water from the mainstem to the tidal floodplain with high SSC and export water from the floodplain to the river with low SSC at almost all locations and river stages. High-SSC water imported on flood tides is a result of advection from the main stem throughout the tide and also via a buoyant plume during early flood. As a result, flood-tide SSC was 18–139% higher than during ebbs in 10 of the 11 deployments. This daily, tidally-influenced change in SSC, which suggests sediment trapping on the tidal floodplain, occurs in addition to seasonal floodplain sediment sequestration (e.g., Bourgoin et al., 2007), which occurs on monthly timescales. The tidal pulse induces the strongest velocities seen in the tidal channels and is a version of the same processes seen in tidal flats and salt marshes. Yet in contrast to these other environments, SSC during the tidal pulse was not considerably greater than elsewhere in the tidal cycle. Local resuspension is also important in strongly tidal locations, as indicated by the increase in mean SSC with tidal range. Unit-width rates of tidal sediment transport in tidal channels along the tidal river are comparable to previous overbank estimates of sediment flux during the seasonal flood wave in the central Amazon. These observations show channels are important conduits of sediment-laden water to floodplains where sediment can be trapped on seasonal or longer timescales.

Sediment that is not imported or trapped on the tidal floodplain may be exported from the tidal river or temporarily stored within the mainstem river channel. Chapter 4 presents water-column and bed-sediment time-series observations made along 30 km of the tidal Mekong River. These measurements include water level, flow velocity, salinity, SSC, and bed-sediment grain size, and expand the present understanding of the dynamics of large tropical deltas under varying seasonal discharge. The flow and sediment dynamics of the tidal Mekong River undergo a comprehensive regime change between high and low seasonal discharge. This regime change is the transition from a tidal freshwater system with an ephemeral salt wedge to a partially mixed estuarine system. During high flow, Dinh An residual sediment discharge was seaward at a rate of about 1 t s^{-1}. During low flow it was

spatially variable and landward at a rate of 0.3 t s^{-1}. These rates scale to a yearly sediment discharge to the South China Sea of 11 Mt y^{-1} for the Dinh An channel and 40 Mt y^{-1} for the entire Mekong River. This value is about 65% less than most previous estimates of Mekong sediment discharge. Decomposition of the sediment flux reveals that the river component was most important during high flow, while baroclinic and tidal processes, especially local resuspension, were more important during low flow. Residual sediment flux was seaward throughout the water column during high flow. During low flow, residual sediment flux was landward in deep regions and seaward in the upper water column. These pathways provide evidence for larger-scale mutually evasive flow (sediment import via Dinh An and export via Tran De) around Cu Lao Dung during low flow. Seasonal flow dynamics are reflected in seabed grain-size characteristics, wherein grain size is coarse but variable during high flow and finer during low flow. The residual flow and sediment-flux patterns also support the maintenance and progradation of mid-channel islands. These results help elucidate processes controlling geomorphic change within tidal rivers.

The research presented here is evidence of the spatial and temporal complexity of tidally influenced systems in a variety of environments with a range of fluvial influence. The field observations and their interpretation in each chapter are important contributions to knowledge of sedimentary processes in two gateways on the path from land to sea. Work on the tidal flats furthers an already rich corpus of literature and highlights the importance of small channels in tidal-flat systems. Results from the mainstem and tidal channels of two large tidal rivers represent a considerable advance in our understanding of this missing link in the source-to-sink continuum.

BIBLIOGRAPHY

Alexander, C. R., Nittrouer, C. A., Demaster, D. J., Park, Y.-A., and Park, S.-C. (1991). Macrotidal mudflats of the southwestern korean coast: a model for interpretation of intertidal deposits. *Journal of Sedimentary Research*, 61(5).

Allen, G., Salomon, J., Bassoullet, P., du Penhoat, Y., and de Grandpre, C. (1980). Effects of tides on mixing and suspended sediment transport in macrotidal estuaries. *Sedimentary Geology*, 26:69–90.

Allen, J. (1994). A continuity-based sedimentological model for temperate-zone tidal salt marshes. *Journal of the Geological Society*, 151(1):41–49.

Allison, M., Nittrouer, C., and Kineke, G. (1995). Seasonal sediment storage on mudflats adjacent to the Amazon River. *Marine Geology*, 125(3-4):303–328.

Alsdorf, D., Han, S.-C., Bates, P., and Melack, J. (2010). Seasonal water storage on the Amazon floodplain measured from satellites. *Remote Sensing of Environment*, 114(11):2448–2456.

Amos, C. (1995). Siliciclastic tidal flats. In Perillo, G., editor, *Geomorphology and Sedimentology of Estuaries*, pages 273–306. Elsevier.

Anderson, F. E., Black, L., Watling, L. E., Mook, W., and Mayer, L. M. (1981). A temporal and spatial study of mudflat erosion and deposition. *Journal of Sedimentary Petrology*, 51(3):729–736.

Andrews, R. S. (1965). Modern sediments of Willapa Bay, Washington: A coastal plain estuary. Technical Report 118, University of Washington Department of Oceanography.

Anikiyev, V., Zaytsev, O., Hieu, T. T., Savil'yeva, I., Starodubtsev, Y., and Shumilin, Y. (1986). Variation in the Space-Time Distribution of Suspended Matter in the Coastal Zone of the Mekong River. *Oceanology*, 26(6):725–729.

Arscott, D. B., Tockner, K., and Ward, J. (2001). Thermal heterogeneity along a braided floodplain river (Tagliamento River, northeastern Italy). *Canadian Journal of Fisheries and Aquatic Sciences*, 58(12):2359–2373.

Bale, A., Morris, A., and Howland, R. (1985). Seasonal sediment movement in the Tamar Estuary. *Oceanologica Acta*, 8(1):1–6.

Banas, N. S. and Hickey, B. M. (2005). Mapping exchange and residence time in a model of Willapa Bay, Washington, a branching, macrotidal estuary. *Journal of Geophysical Research*, 110:C11011.

Banas, N. S., Hickey, B. M., MacCready, P., and Newton, J. A. (2004). Dynamics of Willapa Bay, Washington: A Highly Unsteady, Partially Mixed Estuary. *Journal of Physical Oceanography*, 34:2413–2427.

Barua, D. K. (1990). Suspended sediment movement in the estuary of the Ganges-Brahmaputra-Meghna river system. *Marine Geology*, 91:243–253.

Bayliss-Smith, T., Healey, R., Lailey, R., Spencer, T., and Stoddart, D. (1979). Tidal flows in salt marsh creeks. *Estuarine and Coastal Marine Science*, 9(3):235–255.

Bell, H. S. (1940). Armored mud balls: their origin, properties, and role in sedimentation. *The Journal of Geology*, 48(1):1–31.

Berner, R. A. and Raiswell, R. (1983). Burial of organic carbon and pyrite sulfur in sediments over phanerozoic time: a new theory. *Geochimica et Cosmochimica Acta*, 47(5):855–862.

Boldt, K. V., Nittrouer, C. A., and Ogston, A. S. (2012). Seasonal transfer and net accumulation of fine sediment on a muddy tidal flat: Willapa Bay, Washington. *Continental Shelf Research*, (this issue).

Boon, J. (1975). Tidal discharge asymmetry in a salt marsh drainage system. *Limnology and Oceanography*, 20(1):71–80.

Bourgoin, L., Bonnet, M., Martinez, J., Kosuth, P., Cochonneau, G., Moreiraturcq, P., Guyot, J., Vauchel, P., Filizola, N., and Seyler, P. (2007). Temporal dynamics of water

and sediment exchanges between the Curuaí floodplain and the Amazon River, Brazil. *Journal of Hydrology*, 335(1-2):140–156.

Brand, A., Lacy, J. R., Hsu, K., Hoover, D., Gladding, S., and Stacey, M. T. (2010). Wind-enhanced resuspension in the shallow waters of South San Francisco Bay: Mechanisms and potential implications for cohesive sediment transport. *Journal of Geophysical Research*, 115(C11):C11024.

Buijsman, M. C., Sherwood, C. R., Gibbs, A. E., Gelfenbaum, G., Kaminsky, G. M., Ruggiero, P., and Franklin, J. (2002). Regional Sediment Budget of the Columbia River Littoral Cell, USA. Open-File Report 2002-281, U.S. Geological Survey.

Callède, J., Medeiros Moreira, D., and Calmant, S. (2013). Détermination de l'altitude du Zéro des stations hydrométriques en Amazonie brésilienne. Application aux lignes d'eau des Rios Negro, Solimões et Amazone. *Revue des Sciences de lEau*, 26(2):153.

Christie, M. C., Dyer, K. R., and Turner, P. (1999). Sediment flux and bed level measurements from a macro tidal mudflat. *Estuarine, Coastal and Shelf Science*, 49(5):667–688.

Csanady, G. (1973). Wind-induced barotropic motions in long lakes. *Journal of Physical Oceanography*, 3:429–438.

Dagg, M., Benner, R., Lohrenz, S., and Lawrence, D. (2004). Transformation of dissolved and particulate materials on continental shelves influenced by large rivers: plume processes. *Continental Shelf Research*, 24(7):833–858.

Dalrymple, R. W., Baker, E. K., Harris, P. T., and Hughes, M. G. (2003). Sedimentology and stratigraphy of a tide-dominated foreland-basin delta (Fly River, Papua New Guinea). In *Tropical deltas of southeast Asia—Sedimentology, stratigraphy, and petroleum geology*, pages 147–174. SEPM (Society for Sedimentary Geology).

Dronkers, J. and van de Kreeke, J. (1986). Experimental determination of salt intrusion mechanisms in the Volkerak estuary. *Netherlands Journal of Sea Research*, 20(1):1–19.

Dunne, T., Mertes, L., and Meade, R. (1998). Exchanges of sediment between the flood plain and channel of the Amazon River in Brazil. *Geological Society of America Bulletin*, 110(4):450–467.

Dyer, K. (1974). The salt balance in stratified estuaries. *Estuarine and Coastal Marine Science*, 2(3):273–281.

Dyer, K., Christie, M., and Wright, E. (2000a). The classification of intertidal mudflats. *Continental Shelf Research*, 20(10):1039–1060.

Dyer, K. R. (1978). The balance of suspended sediment in the Gironde and Thames estuaries. In Kjerfve, B., editor, *Estuarine Transport Processes*, pages 135–146. University of South Carolina Press.

Dyer, K. R. (1986). *Coastal and Estuarine Sediment Dynamics*. John Wiley & Sons, Chichester.

Dyer, K. R. (1995). Sediment transport processes in estuaries. In Perillo, G., editor, *Geomorphology and Sedimentology of Estuaries*, pages 423–449. Elsevier Science B.V., Amsterdam.

Dyer, K. R. (1997). *Estuaries: A physical introduction*. John Wiley & Sons, Chichester, 2nd edition.

Dyer, K. R., Christie, M. C., Feates, N., Fennessy, M. J., Pejrup, M., and Van der Lee, W. (2000b). An investigation into processes influencing the morphodynamics of an intertidal mudflat, the Dollard Estuary, the Netherlands: I. Hydrodynamics and suspended sediment. *Estuarine, Coastal and Shelf Science*, 50(5):607–625.

Economic Commission for Asia and the Far East (1966). *A compendium of major international rivers in the ECAFE region*. United Nations.

Fagherazzi, S., Hannion, M., and D'Odorico, P. (2008). Geomorphic structure of tidal hydrodynamics in salt marsh creeks. *Water Resources Research*, 44(2):1–12.

Fischer, H. B. (1972). Mass transport mechanisms in partially stratified estuaries. *Journal of Fluid Mechanics*, 53:671–687.

Fischer, H. B. (1976). Mixing and Dispersion in Estuaries. *Annual Review of Fluid Mechanics*, 8:107–133.

Fortunato, A. B. and Oliveira, A. (2005). Influence of Intertidal Flats on Tidal Asymmetry. *Journal of Coastal Research*, pages 1062–1067.

French, J. and Stoddart, D. (1992). Hydrodynamics of salt marsh creek systems: implications for marsh morphological development and material exchange. *Earth Surface Processes and Landforms*, 17(3):235–252.

Friedrichs, C. (2011). Tidal flat morphodynamics: A synthesis. In *Treatise on Estuarine and Coastal Science*, volume 3, pages 137–170. Elsevier Inc.

Friedrichs, C., Lynch, D., and Aubrey, D. (1992). Velocity asymmetries in frictionally-dominated tidal embayments: longitudinal and lateral variability. In *Dynamics and Exchanges in Estuaries and the Coastal Zone*, volume 40, pages 277–312.

Friedrichs, C. and Perry, J. (2001). Tidal salt marsh morphodynamics: a synthesis. *Journal of Coastal Research*, SI(27):7–37.

Friedrichs, C. T. and Aubrey, D. G. (1996). Uniform bottom shear stress and equilibrium hyposometry of intertidal flats. In *Coastal and Estuarine Studies: Mixing in Estuaries and Coastal Seas*.

Gagliano, S. M. and McIntire, W. (1968). Reports on the Mekong River Delta. Technical report, Coastal Studies Institute, Louisiana State University.

Gelfenbaum, G. (1983). Suspended-sediment response to semidiurnal and fortnightly tidal variations in a mesotidal estuary: Columbia River, U.S.A. *Marine Geology*, 52(1-2):39–57.

Geyer, W. R. (1993). The importance of suppression of turbulence by stratification on the estuarine turbidity maximum. *Estuaries*, 16(1):113–125.

Gibbs, R. J. (1970). Circulation in the Amazon River Estuary and Adjacent Atlantic Ocean. *Journal of Marine Research*, 28(2):113–123.

Giddings, S. N., Monismith, S. G., Fong, D. A., and Stacey, M. T. (2013). Using depth-normalized coordinates to examine mass transport residual circulation in estuaries with large tidal amplitude relative to the mean depth. *Journal of Physical Oceanography*.

Goodbred, S. L. and Kuehl, S. A. (1998). Floodplain processes in the Bengal Basin and the storage of Ganges–Brahmaputra river sediment: an accretion study using 137Cs and 210Pb geochronology. *Sedimentary Geology*, 121:239–258.

Green, T. and Houk, D. (1980). The resuspension of underwater sediment by rain. *Sedimentology*, 27(5):607–610.

Hansen, D. V. and Rattray, Jr., M. (1966). New dimensions in estuary classification. *Limnology and Oceanography*, 11(3):319–326.

Härden, P. and Sundborg, A. (1992). The lower Mekong basin suspended sediment transport and sedimentation problems. Technical report, Mekong Secretariat, Uppsala.

Harris, P. T. (1988). Large-scale bedforms as indicators of mutually evasive sand transport and the sequential infilling of wide-mouthed estuaries. *Sedimentary Geology*, 57(1988):273–298.

Harris, P. T., Hughes, M. G., Baker, E. K., Dalrymple, R. W., and Keene, J. B. (2004). Sediment transport in distributary channels and its export to the pro-deltaic environment in a tidally dominated delta: Fly River, Papua New Guinea. *Continental Shelf Research*, 24(19):2431–2454.

Healey, R. G., Pye, K., Stoddart, D. R., and Bayliss-Smith, T. P. (1981). Velocity variations in salt marsh creeks, Norfolk, England. *Estuarine, Coastal and Shelf Science*, 13(5):535–545.

Hedges, J. I. and Keil, R. G. (1995). Sedimentary organic matter preservation: an assessment and speculative synthesis. *Marine Chemistry*, 49(2):81–115.

Hill, P., Newgard, J., Law, B., and Milligan, T. (2013). Flocculation on a muddy intertidal flat in Willapa Bay, Washington, Part II: Observations of suspended particle size in a secondary channel and adjacent flat. *Continental Shelf Research*, 60:S145–S156.

Holeman, J. N. (1968). The Sediment Yield of Major Rivers of the World. *Water Resources Research*, 4(4):737–747.

Hori, K., Saito, Y., Zhao, Q., and Wang, P. (2002). Architecture and evolution of the tide-dominated Changjiang (Yangtze) River delta, China. *Sedimentary Geology*, 146(3-4):249–264.

Hsu, T.-J., Chen, S.-N., and Ogston, A. S. (2012). A numerical investigation of fine sediment transport across intertidal flats. *Continental Shelf Research*, (this issue).

Hu, J., Kawamura, H., Hong, H., and Qi, Y. (2000). A review on the currents in the South China Sea: seasonal circulation, South China Sea warm current and Kuroshio intrusion. *Journal of Oceanography*, 56:607–624.

Hughes, F. and Rattray, Jr., M. (1980). Salt flux and mixing in the Columbia River Estuary. *Estuarine and Coastal Marine Science*, 10:479–493.

Instituto Brasileiro de Geografia e Estatística (2012). Relatório Descritivo da Estação Maregráfica de Santana. Technical report, Instituto Brasileiro de Geografia e Estatística.

Junk, W. J., Bayley, P. B., and Sparks, R. E. (1989). The flood pulse concept in river-floodplain systems. In Dodge, D., editor, *Proceedings of the International Large River Symposium*, pages 110–127.

Kjerfve, B. (1986). Circulation and Salt Flux in a Well Mixed Estuary. In van de Kreeke, J., editor, *Physics of Shallow Estuaries and Bays*, pages 22–29. Springer Verlag.

Kosuth, P., Callède, J., Laraque, A., Filizola, N., Guyot, J., Seyler, P., Fritsch, J., and Guimaraes, V. (2009). Sea-tide effects on flows in the lower reaches of the Amazon River. *Hydrological Processes*, 23(22):3141–3150.

Le Hir, P., Roberts, W., Cazaillet, O., Christie, M., Bassoullet, P., and Bacher, C. (2000). Characterization of intertidal flat hydrodynamics. *Continental Shelf Research*, 20(12–13):1433–1459.

Lee, H. J., Jo, H. R., Chu, Y. S., and Bahk, K. S. (2004). Sediment transport on macrotidal flats in Garolim Bay, west coast of Korea: significance of wind waves and asymmetry of tidal currents. *Continental shelf research*, 24(7-8):821–832.

Lerczak, J. A., Geyer, W. R., and Chant, R. J. (2006). Mechanisms driving the time-dependent salt flux in a partially stratified estuary. *Journal of Physical Oceanography*, 36:2296–2311.

MacCready, P. and Banas, N. (2011). Residual Circulation, Mixing, and Dispersion. In Wolanski, E. and McLusky, D., editors, *Treatise on Estuarine and Coastal Science*, pages 75–89. Academic Press.

Madsen, O. S. (1994). Spectral wave-current bottom boundary layer flows. In Edge, B. L., editor, *Coastal Engineering 1994: Proceedings of the twenty-fourth international conference*, pages 384–398. American Society of Civil Engineers.

Malard, F., Mangin, A., Uehlinger, U., and Ward, J. (2001). Thermal heterogeneity in the hyporheic zone of a glacial floodplain. *Canadian Journal of Fisheries and Aquatic Sciences*, 58(7):1319–1335.

Mariotti, G. and Fagherazzi, S. (2011). Asymmetric fluxes of water and sediments in a mesotidal mudflat channel. *Continental Shelf Research*, 31(1):23–36.

Mariotti, G. and Fagherazzi, S. (2012). Asymmetric fluxes of water and sediments in a mesotidal mudflat channel. *Continental Shelf Research*, (this issue).

Meade, R., Nordin, C., Curtis, W., Costa Rodrigues, F., do Vale, C., and Edmond, J. (1979). Sediment loads in the Amazon River. *Nature*, 278:161–163.

Meade, R. H. (1969). Landward transport of bottom sediments in estuaries of the Atlantic coastal plain. *Journal of Sedimentary Petrology*, 39(1):222–234.

Meade, R. H. (1994). Suspended sediments of the modern Amazon and Orinoco rivers. *Quaternary International*, 21(93):29–39.

Mekong River Commission (2014). Data Portal.

Mertes, L. and Dunne, T. (1988). Morphology and construction of the Solimões-Amazon River floodplain. In *Proceedings of the Chapman Conference on the Fate of Particulate and Dissolved Components within the Amazon Dispersal System: River and Ocean*, pages 82–86, Washington, D.C. American Geophysical Union.

Mertes, L. A. (1997). Documentation and significance of the perirheic zone on inundated floodplains. *Water Resources Research*, 33(7):1749–1762.

Mertes, L. A. K. (1994). Rates of flood-plain sedimentation on the central Amazon River. *Geology*, 22:171–174.

Mertes, L. A. K., Dunne, T., and Martinelli, L. A. (1996). Channel-floodplain geomorphology along the Solimões-Amazon River, Brazil. *Geological Society of America Bulletin*, 108(9):1089–1107.

Milliman, J. D. (1980). Sedimentation in the Fraser River and its estuary, southwestern British Columbia (Canada). *Estuarine and Coastal Marine Science*, 10:609–633.

Milliman, J. D. and Farnsworth, K. L. (2011). *River Discharge to the Coastal Ocean: A Global Synthesis*. Cambridge University Press, Cambridge.

Milliman, J. D., Huang-Ting, S., Zuo-Sheng, Y., and Meade, R. H. (1985). Transport and deposition of river sediment in the Changjiang estuary and adjacent continental shelf. *Continental Shelf Research*, 4(1/2):37–45.

Mosley, M. P. (1989). Variability of water temperatures in the braided Ashley and Rakaia rivers. *New Zealand Journal of Marine and Freshwater Research*, 17:331–342.

Mwamba, M. J. and Torres, R. (2002). Rainfall effects on marsh sediment redistribution, North Inlet, South Carolina, USA. *Marine Geology*, 189(3-4):267–287.

Myrick, R. M. and Leopold, L. B. (1963). Hydraulic geometry of a small tidal estuary. Technical report, U.S. Geological Survey.

Nguyen, A. D., Savenije, H. H., Pham, D. N., and Tang, D. T. (2008). Using salt intrusion measurements to determine the freshwater discharge distribution over the branches of a multi-channel estuary: The Mekong Delta case. *Estuarine, Coastal and Shelf Science*, 77(3):433–445.

Nguyen, T. and Tanaka, H. (2007). Study on the Effect of Morphology Change on Salinity Distribution in the Dinh An Estuary, Lower Mekong River of Vietnam. *Journal of Coastal Research*, SI 50:268–272.

Nittrouer, C. A., Kuehl, S. A., Sternberg, R. W., Figueiredo, A. G., and Faria, L. E. C. (1995). An introduction to the geological significance of sediment transport and accumulation on the Amazon continental shelf. *Marine Geology*, 125:177–192.

Nowacki, D. J. and Ogston, A. S. (2013). Water and sediment transport of channel-flat systems in a mesotidal mudflat: Willapa Bay, Washington. *Continental Shelf Research*, 60:1–14.

O'Brien, D. J., Whitehouse, R. J. S., and Cramp, A. (2000). The cyclic development of a macrotidal mudflat on varying timescales. *Continental Shelf Research*, 20(12-13):1593–1619.

Ogston, A. S., Sternberg, R. W., Nittrouer, C. A., Martin, D. P., Goñi, M. A., and Crockett, J. S. (2008). Sediment delivery from the Fly River tidally dominated delta to the nearshore marine environment and the impact of El Niño. *Journal of Geophysical Research*, 113(F1):F01S11.

Osterkamp, W. (1998). Processes of fluvial island formation, with examples from Plum Creek, Colorado and Snake River, Idaho. *Wetlands*, 18(4):530–545.

Pejrup, M. (1988). Suspended sediment transport across a tidal flat. *Marine Geology*, 82(3-4):187–198.

Pestrong, R. (1965). The development of drainage patterns on tidal marshes. *Stanford University Publications*, 10(2).

Pilditch, C. A., Widdows, J., Kuhn, N. J., Pope, N. D., and Brinsley, M. D. (2008). Effects of low tide rainfall on the erodibility of intertidal cohesive sediments. *Continental Shelf Research*, 28(14):1854–1865.

Postma, H. (1961). Transport and accumulation of suspended matter in the Dutch Wadden Sea. *Netherlands Journal of Sea Research*, 1(1/2):148–190.

Postma, H. (1967). Sediment Transport and Sedimentation in the Estuarine Environment. In Lauff, G. H., editor, *Estuaries*, pages 158–179. American Association for the Advancement of Science.

Ralston, D. K., Geyer, W. R., Lerczak, J. a., and Scully, M. (2010). Turbulent mixing in a strongly forced salt wedge estuary. *Journal of Geophysical Research: Oceans*, 115(C6):1–21.

Ralston, D. K., Geyer, W. R., and Warner, J. C. (2012). Bathymetric controls on sediment transport in the Hudson River estuary: Lateral asymmetry and frontal trapping. *Journal of Geophysical Research*, 117(C10):C10013.

Ralston, D. K. and Stacey, M. T. (2007). Tidal and meteorological forcing of sediment transport in tributary mudflat channels. *Continental Shelf Research*, 27(10-11):1510–1527.

Richey, J., Mertes, L., Dunne, T., Victoria, R., Forsberg, B., Tancredi, A., and Oliveira, E. (1989). Sources and routing of the Amazon River flood wave. *Global Biogeochemical Cycles*, 3(3):191–204.

Ridderinkhof, H., van der Ham, R., and van der Lee, W. (2000). Temporal variations in concentration and transport of suspended sediments in a channelflat system in the Ems-Dollard estuary. *Continental Shelf Research*, 20(12-13):1479–1493.

Sanford, L. P. (1994). Wave-forced resuspension of upper Chesapeake Bay muds. *Estuaries and Coasts*, 17(1):148–165.

Savenije, H. H. (2005). *Salinity and Tides in Alluvial Estuaries*. Elsevier.

Schubel, J. (1968). Turbidity maximum of the northern Chesapeake Bay. *Science*, 161(3845):1013–1015.

Shi, Z. and Chen, J. (1996). Morphodynamics and sediment dynamics on intertidal mudflats in china (1961–1994). *Continental Shelf Research*, 16(15):1909–1926.

Shin, J., Dalziel, S., and Linden, P. (2004). Gravity currents produced by lock exchange. *Journal of Fluid Mechanics*, 521:1–34.

Su, J. and Wang, K. (1986). The Suspended Sediment Balance in Changjiang Estuary. *Estuarine, Coastal and Shelf Science*, 23:81–98.

Syvitski, J. P. M. and Kettner, A. (2011). Sediment flux and the Anthropocene. *Philosophical Transactions of the Royal Society A*, 369(1938):957–975.

Ta, T. K. O., Nguyen, V. L., Tateishi, M., Kobayashi, I., and Saito, Y. (2005). Holocene delta evolution and deposition models of the Mekong River Delta, southern Vietnam. In Giosan, L. and Bhattacharya, J. P., editors, *River Deltas—Concepts, Models, and Examples*, pages 453–466. SEPM (Society for Sedimentary Geology).

Tockner, K., Malard, F., and Ward, J. (2000). An extension of the flood pulse concept. *Hydrological Processes*, 14:2861–2883.

Tolhurst, T. J., Friend, P. L., Watts, C., Wakefield, R., Black, K. S., and Paterson, D. M. (2006). The effects of rain on the erosion threshold of intertidal cohesive sediments. *Aquatic Ecology*, 40(4):533–541.

Uncles, R., Elliott, R., and Weston, S. (1985a). Dispersion of salt and suspended sediment in a partly mixed estuary. *Estuaries*, 8(3):256–269.

Uncles, R., Elliott, R., and Weston, S. (1985b). Observed fluxes of water, salt and suspended sediment in a partly mixed estuary. *Estuarine, Coastal and Shelf Science*, 20(2):147–167.

Uncles, R. and Jordan, M. (1979). Residual fluxes of water and salt at two stations in the Severn Estuary. *Estuarine and Coastal Marine Science*, 9(3):287–302.

Unverricht, D., Szczuciński, W., Stattegger, K., Jagodziński, R., Le, X. T., and Kwong, L. L. W. (2013). Modern sedimentation and morphology of the subaqueous Mekong Delta, Southern Vietnam. *Global and Planetary Change*, 110:223–235.

van Straaten, L. and Kuenen, P. H. (1958). Tidal action as a cause of clay accumulation. *Journal of Sedimentary Petrology*, 28(4):406–413.

Vital, H. and Stattegger, K. (2000a). Major and trace elements of stream sediments from the lowermost Amazon River. *Chemical Geology*, 168(1-2):151–168.

Vital, H. and Stattegger, K. (2000b). Sediment dynamics in the lowermost Amazon. *Journal of Coastal Research*, 16(2):316–328.

Vital, H., Stattegger, K., Posewang, J., and Theilen, F. (1998). Lowermost Amazon River: morphology and shallow seismic characteristics. *Marine Geology*, 152(4):277–294.

Walters, R., Cheng, R., and Conomos, T. (1985). Time scales of circulation and mixing processes of San Francisco Bay waters. *Hydrobiologia*, 129:13–36.

Webster, K. L., Ogston, A. S., and Nittrouer, C. a. (2013). Delivery, reworking and export of fine-grained sediment across the sandy Skagit River tidal flats. *Continental Shelf Research*, 60:S58–S70.

Wellershaus, S. (1981). Turbidity maximum and mud shoaling in the Weser estuary. *Archiv für Hydrobiologie*, 92(2):161–198.

Wells, J. T., Adams Jr, C. E., Park, Y. A., and Frankenberg, E. W. (1990). Morphology, sedimentology and tidal channel processes on a high-tide-range mudflat, west coast of South Korea. *Marine Geology*, 95(2):111–130.

Wiberg, P. L., Law, B. A., Wheatcroft, R. A., Milligan, T. G., and Hill, P. S. (2012). Seasonal Variations in Erodibility and Sediment Transport Potential in a Mesotidal Channel-Flat Complex, Willapa Bay, WA. *Continental Shelf Research*, (this issue).

Wolanski, E., Mazda, Y., and Ridd, P. (1992). Mangrove Hydrodynamics. In Robertson, A. and Alongi, D., editors, *Coastal and Estuarine Studies: Tropical Mangrove Ecosystems*, volume 41, pages 43–62. American Geophysical Union, Washington, D.C.

Wolanski, E., Ngoc Huan, N., Trong Dao, L., Huu Nhan, N., and Ngoc Thuy, N. (1996). Fine-sediment dynamics in the Mekong River estuary, Vietnam. *Estuarine, Coastal and Shelf Science*, 43(5):565–582.

Wolanski, E., Nhan, N., and Spagnol, S. (1998). Sediment dynamics during low flow conditions in the Mekong River Estuary, Vietnam. *Journal of Coastal Research*, 14(2):472–482.

Woodruff, J. D., Geyer, W. R., Sommerfield, C. K., and Driscoll, N. W. (2001). Seasonal variation of sediment deposition in the Hudson River estuary. *Marine Geology*, 179:105–119.

Wright, L. (1977). Sediment transport and deposition at river mouths: a synthesis. *Bulletin of the Geological Society of America*, 88(6):857.

Wright, L. (1985). River Deltas. In *Coastal Sedimentary Environments*. Springer-Verlag, New York.

Xue, Z., Liu, J. P., DeMaster, D., Van Nguyen, L., and Ta, T. K. O. (2010). Late Holocene Evolution of the Mekong Subaqueous Delta, Southern Vietnam. *Marine Geology*, 269(1-2):46–60.

Xue, Z., Liu, J. P., and Ge, Q. (2011). Changes in hydrology and sediment delivery of the Mekong River in the last 50 years: connection to damming, monsoon, and ENSO. *Earth Surface Processes and Landforms*, 36(3):296–308.

Yang, B., Dalrymple, R., and Chun, S. (2005). Sedimentation on a wave-dominated, open-coast tidal flat, south-western Korea: summer tidal flat–winter shoreface. *Sedimentology*, 52(2):235–252.

Yang, S.-L., Ding, P.-X., and Chen, S.-L. (2001). Changes in progradation rate of the tidal flats at the mouth of the Changjiang (Yangtze) River, China. *Geomorphology*, 38:167–180.

Yang, S. L., Friedrichs, C. T., Shi, Z., Ding, P. X., Zhu, J., and Zhao, Q. Y. (2003). Morphological response of tidal marshes, flats and channels of the outer Yangtze River mouth to a major storm. *Estuaries*, 26(6):1416–1425.

Yelland, M. J., Moat, B. I., Taylor, P. K., Pascal, R. W., Hutchings, J., and Cornell, V. C. (1998). Wind stress measurements from the open ocean corrected for airflow distortion by the ship. *Journal of Physical Oceanography*, 28(7):1511–1526.